

## ABSTRACT

Title of dissertation: DISSIPATION IN A  
SUPERFLUID ATOM CIRCUIT

Jeffrey Garver Lee, Doctor of Philosophy, 2017

Dissertation directed by: Professor Wendell T. Hill, III  
Chemical Physics Program

Bose-Einstein condensates of weakly interacting dilute atomic gases provide a unique system with which to study phenomena associated with superfluidity. The simplicity of these systems allows us to study the fundamental physics of superfluidity without having to consider the strong interactions present in other superfluid systems such as superconductors and liquid helium. While condensate-based studies have been around for 20 years, our novel approach to confining ultracold atoms has opened a completely new range of parameter space to investigate. Armed with an ability for straightforward creation of arbitrary, time-dependent potential landscapes in which to study superfluid interactions, we were able to take a closer look at predictions of superfluid behavior that are decades old, but until now have never been tested directly. The purpose of this research was to draw direct analogies between superfluid BEC systems, which we term superfluid atom circuits, and existing superconducting circuits, thus allowing us to take advantage of much of the existing knowledge that has come from this well-studied field. Specifically, existing circuits and devices that have been created with superconductors give us insight into what

might be possible someday with atom-circuit devices and inspiration to create them.

In these experiments, we employed two different atom circuits; one classical (thermal ideal gas) and one quantum (ultracold superfluid). Our results show that each system is equivalent to an electronic circuit consisting of a capacitor being discharged through an inductor in series with some dissipative element. In the thermal system, dissipation can be described in terms of simple resistive flow with the resistance equivalent to ballistic, Sharvin resistance seen in electronic circuits. The superfluid measurements show that the dissipation is best described as a resistance-shunted Josephson junction, which is an analogue to similar devices in superconducting circuits. Additionally, the specific geometry of the atom circuit we used in our superfluid system allowed us to investigate directly a predicted mechanism responsible for the dissipation in superfluids caused by the generation of collective excitations, namely vortices. Direct observation of this mechanism has not previously been possible in superfluid helium and superconducting systems.

# DISSIPATION IN A SUPERFLUID ATOM CIRCUIT

by

Jeffrey Garver Lee

Dissertation submitted to the Faculty of the Graduate School of the  
University of Maryland, College Park in partial fulfillment  
of the requirements for the degree of  
Doctor of Philosophy  
2017

Advisory Committee:  
Professor Wendell T. Hill, III, Chair/Advisor  
Professor Gretchen K. Campbell  
Dr. Stephen P. Eckel  
Professor Christopher Jarzynski  
Professor Christopher J. Lobb  
Professor William D. Phillips

© Copyright by  
Jeffrey Garver Lee  
2017

# Table of Contents

List of Figures	iv
List of Abbreviations	vi
1 Introduction	1
1.1 History of Superfluidity	1
1.2 BEC Atom Circuits as Analogs of Superconducting Circuits	3
1.2.1 An Atom Capacitor	4
1.2.2 Experimental Setup	6
1.2.3 Results	6
2 Atom Circuit Analog	8
2.1 An Atom Circuit to Study Dissipation	8
2.2 Chemical Potential and Capacitance	9
2.2.1 Capacitance in a BEC System	11
2.3 Kinetic Inductance	15
2.4 Dissipation	16
2.4.1 A Superfluid Weak Link	16
2.4.2 Superfluid Dissipation - Feynman Resistance	18
2.4.3 Dissipation in a Thermal Gas	21
3 Apparatus	26
3.1 BEC Apparatus	26
3.1.1 Laser System	27
3.1.2 Main Experimental Optical Breadboard	31
3.1.3 Computer Control	32
3.1.4 Imaging	35
3.1.5 Cooling Sequence	36
3.1.6 Imaging	37
3.1.7 Trap Geometry	38
3.1.7.1 The Sheet	39
3.1.7.2 The Reservoirs	40

3.1.7.3	The Channel	41
3.2	Thermal Cold Atom Apparatus	43
3.2.1	Vacuum System	43
3.2.2	Laser System	46
3.2.3	Computer Control	51
3.2.4	Cooling Sequence	51
3.2.5	Imaging	52
3.2.6	Thermal System Temperature	53
3.2.6.1	Truncated Thermal Distribution	54
3.3	Creating a Dumbbell Potential	57
3.3.1	Generalized Phase-Contrast Imaging	57
3.3.2	Direct Intensity Masking	63
3.3.2.1	Construction of Intensity Masks	65
4	Experimental Details and Results	69
4.1	Thermal System	69
4.1.1	Details of Parameters varied in Experiment	70
4.1.2	Data	70
4.1.3	Comparison to Expected Values	71
4.2	BEC System	77
4.2.1	Details of Parameters varied in Experiment	78
4.2.2	Data	78
4.2.3	Component Values	80
4.2.4	Observation of Vortices	85
4.3	Conclusions	88
4.3.1	Future Directions	90
A	Details of Cooling Methods	92
A.1	Cooling and Trapping Methods	92
A.1.1	Electronic Structure of the Alkali Atoms	92
A.1.2	Zeeman Slowing	95
A.1.3	Magneto-Optical Trapping	96
A.1.4	Dark-Spot MOT	98
A.1.5	Evaporative Cooling and Conservative Traps	99
A.1.5.1	Evaporative Cooling	99
A.1.5.2	Magnetic Trapping	100
A.1.5.3	Evaporative Cooling in a Magnetic Trap	102
A.1.5.4	Dipole Trapping	103
A.1.5.5	Evaporatively Cooling in a Dipole Trap	106
A.2	Imaging	106
A.2.1	Fluorescence Imaging	106
A.2.2	Absorption Imaging	107
A.2.2.1	Partial Transfer Absorption Imaging	108
	Bibliography	110

## List of Figures

2.1	Dumbbell Trap Geometry . . . . .	9
2.2	Fit of Chemical Potential of a Single Reservoir . . . . .	12
2.3	BEC Chemical Potential of a Single Reservoir . . . . .	13
2.4	BEC Chemical Potential of Both Reservoirs . . . . .	14
2.5	BEC Chemical Potential Difference . . . . .	14
2.6	Superfluid Atom Circuit Model . . . . .	18
2.7	Feynman Vortex Production . . . . .	19
3.1	BEC System Schematic . . . . .	27
3.2	BEC System Main Laser Table Schematic . . . . .	29
3.3	BEC System Main Laser Setup Image . . . . .	30
3.4	BEC System Main Laser Frequencies . . . . .	30
3.5	BEC System Upper Optical Breadboard Schematic . . . . .	33
3.6	BEC System Upper Optical Breadboard Image . . . . .	34
3.7	BEC in a Dumbbell Potential . . . . .	39
3.8	Reservoir Potential Shape . . . . .	41
3.9	Thermal Rb Vacuum System . . . . .	44
3.10	Thermal Rb Vacuum Chamber and MOT Optical Setup Image . . . . .	45
3.11	Thermal Rb Main Laser System Schematic . . . . .	47
3.12	Thermal Rb Main Laser System Image . . . . .	48
3.13	Tapered Amplifier Seed Laser Setup . . . . .	50
3.14	Thermal Gas Expansion for Temperature Measurement . . . . .	55
3.15	Truncated Thermal Velocity Distribution . . . . .	56
3.16	Generalized Phase-Contrast Imaging System Schematic . . . . .	58
3.17	Generalized Phase-Contrast Imaging System Image . . . . .	59
3.18	Direct Intensity Mask Imaging Setup . . . . .	64
4.1	Thermal Capacitor Discharge Composite Image . . . . .	72
4.2	Plot of Capacitor Discharge Dynamics in the Thermal System . . . . .	73
4.3	Plot of Capacitor Discharge Dynamics in the Thermal System (cont.) . . . . .	74
4.4	Comparison of Measured Decay Times to Theory . . . . .	76
4.5	BEC Capacitor Discharge Composite Image . . . . .	79

4.6	Plot of Capacitor Discharge Dynamics in the BEC System with nominally $125 \times 10^3$ Atoms . . . . .	80
4.7	Plot of Capacitor Discharge Dynamics in the BEC System with nominally $230 \times 10^3$ Atoms . . . . .	81
4.8	Plot of Capacitor Discharge Dynamics in the BEC System with nominally $333 \times 10^3$ Atoms . . . . .	82
4.9	Plot of Capacitor Discharge Dynamics in the BEC System with nominally $470 \times 10^3$ Atoms . . . . .	83
4.10	Plot of Measured Conductance in the BEC System . . . . .	85
4.11	Comparison of Measured to Expected Inductance in the BEC System . . . . .	86
4.12	Comparison of Measured to Expected Critical Current in the BEC System . . . . .	87
4.13	Collective Excitations Imaged in Time-of-Flight . . . . .	87
A.1	Na Electronic Structure . . . . .	93
A.2	Rb Electronic Structure . . . . .	94

## List of Abbreviations

1D	1-dimensional
2D	2-dimensional
Rb	Rubidium
Na	Sodium
AM	Amplitude Mask
AOM	Acousto-Optic Modulator
AOD	Acousto-Optic Deflector
AR	Anti-Reflective
BEC	Bose-Einstein Condensate
GPC	Generalized Phase-Contrast
IR	Infrared
LCoS	Liquid Crystal on Silicon
LG	Laguerre-Gauss
MOT	Magneto-Optical Trap
NA	Numerical Aperture
ODP	Optical Dipole Potential
ODT	Optical Dipole Trap
PCF	Phase-Contrast Filter
RF	Radio Frequency
RMS	Root-Mean Squared
SA	Saturated Absorption
SLM	Spatial Light Modulator
SQUID	Superconducting Quantum Interference Device
TOF	Time-of-Flight
TOP	Time-orbiting potential
UHV	Ultra-High Vacuum
UV	Ultraviolet

## Chapter 1: Introduction

### 1.1 History of Superfluidity

Since its first observation in the form of superconductivity in 1911 [1], the phenomenon of superfluidity has continued to be of interest on the frontiers of physics. The surprising result that came out of these experiments, that the resistance in solid mercury suddenly drops to a value indistinguishable from zero below a critical temperature of 4.2 K, has many interesting implications such as the possibility of persistent currents which can flow almost indefinitely [2,3]. Not long after this, liquid helium was observed to exhibit strange behaviors below a critical temperature of 2.2 K [4,5]. Similar to the drop in resistance that was seen in superconductors, a sudden and dramatic drop of viscosity was seen in liquid helium. Again, this drop in viscosity leads to many new effects in liquid helium, such as the superfluid fountain [5], and superfluid “creep” [6,7]. Later still, superfluid effects were predicted and seen in dilute atomic gases cooled to below the threshold for Bose-Einstein Condensation [8–16]. Our goal is to use these Bose-Einstein Condensates (BECs) to further study the nature of superfluidity, and in particular draw analogies between these newer systems and the superconducting systems that have been around for longer and are more well studied. Because the parameter spaces for controls in ex-

periments are quite different between these systems, this analogy will not only allow a direct comparison of aspects of them that overlap, it would enable us to extend the observations of either field to areas that are not directly observable in the other. In order to facilitate this, we also develop two new methods for creating arbitrary optical dipole potentials for ultracold atom research.

It took many decades to begin to understand the new phenomena observed in superfluid systems, with the first qualitative explanations not coming until 1938 when London related it to Bose-Einstein condensation [17]. This was later extended to include both a condensed fraction with identically zero viscosity, and the remaining uncondensed fraction that contributes to dissipation and viscosity [18]. In 1941, Landau published his quantitative description of superfluidity using a similar two-component model with a ground superfluid state and a normal excited state [19]. In addition to quantitatively describing the transition to superfluid, including accurate predictions of the transition temperature, Landau's theory also predicted as of yet unseen phenomena such as second sound, which would later be observed [20]. In 1947, Bogoliubov started to make a stronger connection between Landau's quantitative, two component superfluid model and Bose-Einstein condensation [21]. He showed that the excitation spectra of collective excitations in a weakly interacting BEC have the same dispersion relation seen in the Landau formalism. While not directly applicable to liquid helium due to the strong interatomic interaction, it is often used in modern descriptions of weakly interacting BEC superfluids.

Extending this description further, Onsager [22] and Feynman [23] later included descriptions of rotation in the superfluid lacking from Landau's description.

These rotations, called vortices, carry an amount of energy, so a system which continually produces vortices will exhibit dissipation. Experiments have since confirmed the existence of vortices in superfluids, although the study described in this thesis is the first to directly observe dissipation in a system with the geometry described by Feynman [23].

## 1.2 BEC Atom Circuits as Analogs of Superconducting Circuits

In order to further our understanding of superfluids, our study draws an analogy between superconducting circuit models and the dynamics of atoms in a dilute atomic BEC. This analogy allows us to study things that are not possible in superconductors, as well as use existing knowledge of superconductors to further the uses of superfluid BEC systems.

The differences between superconductors and BECs allow us to create a system similar to what can be made in a superconductor, but having properties and adjustable parameters different from what is possible at the moment in superconducting systems. In superconductors, the confining potential for the electrons is always nearly hard-walled due to the structure of the wires used. Also, once the circuit is created and cooled down to below the transition temperature, the overall structure is fixed, although variations can be introduced such as gating potentials. In our system, the confining potentials are created using light and magnetic fields. This allows us to create time-varying potentials, although it constrains us to soft-walled potentials. Additionally, we are able to observe directly the atoms in BEC,

which is a huge advantage over either liquid helium or superconductors. Finally, in superconducting circuits, the superconducting electrons flow through the complex lattice structure of the superconducting wires themselves. Coupling to this lattice can have effects on the superfluid that are not present in atomic gas systems since these are confined in very different ways.

By drawing our analogy between these systems, we are also able to use the wealth of knowledge that already exists in the field of superconductivity to guide our research of superfluidity in an atomic BEC. There have been an incredible variety of superconducting circuits studied previously, ranging from simple test setups used in basic experiments, to complex radio frequency (RF) circuits, to practical commercial devices such as superconducting quantum interference devices (SQUIDs) [24]. The results of experiments with these circuits can help us to start to envision what practical devices we might someday be able to create with superfluid BEC systems.

### 1.2.1 An Atom Capacitor

In chapter 2, we will show that the system we created is analogous to an electronic capacitor being discharged through an inductor in series with a dissipative element. The geometry we create that produces this atom capacitor consists of two reservoirs separated by a channel. In our system, a difference in atom density between the two reservoirs will produce a chemical potential difference that drives atom flow through the channel to equalize the imbalance. This is equivalent to what happens in a parallel plate capacitor, where a charge imbalance between the

two plates causes an electro-chemical potential difference between the plates that drives electric current to flow through a circuit to equalize the imbalance. There are obvious differences between these systems, such as the fact that in our system the relative location of the two reservoirs has no effect on the potential difference. Due to the longer range interaction between electrons in the parallel plate capacitor, this is not true for the electronic case.

The flow in our atomic system is restricted by a few factors. First, we will derive an effective inductance in the system analogous to kinetic inductance in electronics. Again there are differences between the systems. In the electronic case, the energy stored in an inductor is stored in a magnetic field. In our system it is stored as the kinetic energy of atoms flowing in the channel. In addition to this inductance, there will be dissipation due to two main factors. In the thermal part of the system, there will be an equivalent to the Sharvin resistance seen in electronics [25]. This limiting is easy to understand intuitively. It is due to the number of collisions of the thermal atoms with an imaginary cross sectional area of the wall that the channel covers. A narrower channel results in a lower rate of collisions with this imaginary area, thus increasing the effective resistance. The other dissipation that is present in our system is due to collective excitations in the superfluid, such as vortices, phonons, and solitons. We will focus only on vortex excitations in this study since we are following the model presented by Feynman [23]. In this model, these vortices are created when the superfluid flow exits the channel into one of the reservoirs. If this flow is higher than some superfluid critical velocity, vortices will be produced. These excitations carry an amount of energy in the form of kinetic

energy, and eventually thermalize in the system, raising the temperature.

## 1.2.2 Experimental Setup

In chapter 3, we describe our experimental setup in detail. Two separate setups were used to test the theory derived in chapter 2; one classical (thermal ideal gas) system and one quantum (superfluid BEC) system. In each case, the atoms are confined using optical dipole potentials. For the thermal system, we extend the concept of Generalized Phase-Contrast Imaging used in microscopy to create arbitrary two dimensional (2D) optical dipole potentials (ODP)s. In the BEC system, we use the equipment from a microfabrication lab to create intensity masks for direct imaging of the required geometry to create the trap. By starting these systems with more atoms loaded into one reservoir then allowing flow for a variable amount of time, we are able to study the dynamics of flow in the system. We are also able to image the effects of the collective excitations present in the BEC by releasing the trap after some flow has occurred, and imaging in time-of-flight. A detailed description of the more commonly used techniques in our experiment are described in appendix A.

## 1.2.3 Results

In chapter 4, we lay out the details of the parameters varied throughout the experimental runs, and show the data collected. We also fit this data to our expected forms derived in chapter 2. We show that our system can in fact be modeled well

by our proposed circuit analogy. Additionally, we show direct observation of the collective excitations expected in our system that contribute to the dissipation seen in the circuit.

## Chapter 2: Atom Circuit Analog

### 2.1 An Atom Circuit to Study Dissipation

In order to study dissipation in an ultracold atomic system, we will create a trapping geometry for our atoms that produces dynamics in atom flow that are analogous to those in an electronic circuit. This geometry of this trap in the horizontal plane, shown in figure 2.1, consists of a dumbbell shape with two circular reservoirs connected by a channel. In the vertical direction the trap can be described by a tightly confining harmonic potential. As we will show below, this dumbbell geometry provides us with an analog to a capacitor with the reservoirs holding the potential difference needed to create flow in the circuit, and the channel between them providing an analog to two other circuit elements. The first of these is the common inductor, which arises in our system due to the kinetic energy of the atoms flowing between the reservoirs. The other is a more complex resistance shunted Josephson-Junction, caused by a weak superfluid link in combination with collective excitations due to flow above a critical velocity.

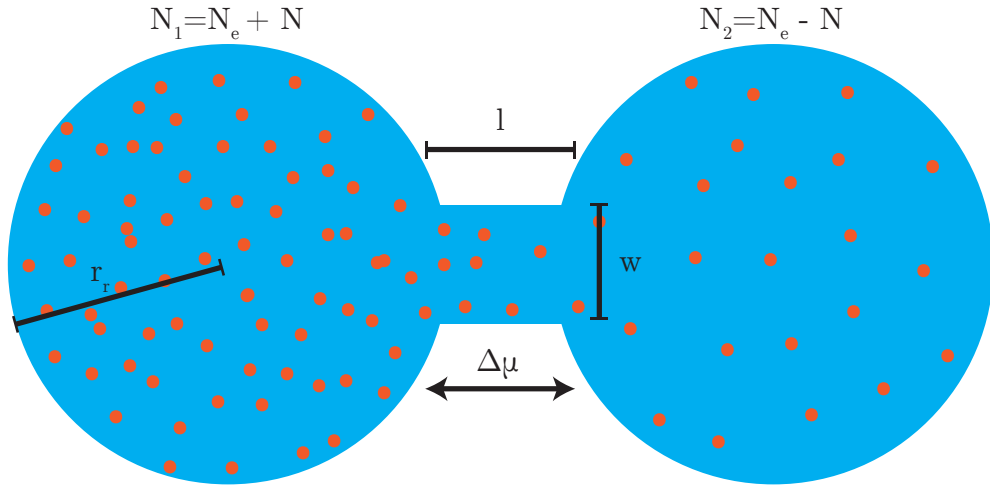


Figure 2.1: A schematic of the geometry of our dumbbell potential, showing the two reservoirs with relevant dimensions (channel width  $w$ , channel length  $l$ , and reservoir area  $A = \pi r_r^2$ , where  $r_r$  is the radius of the reservoirs). The number of atoms in one reservoir is given by  $N_1 = N_e + N$ , and the other  $N_2 = N_e - N$ , where  $N_e = N_{tot}/2$  is the equilibrium number of atoms in either reservoir, and  $N$  is what we call the number imbalance in the system, which is half the difference in atom number between the reservoirs.

## 2.2 Chemical Potential and Capacitance

The simplest element of our system that we will look at is the atom circuit analog to a capacitor. In any non-superconducting circuit, a source of electric potential difference is needed to drive current through the various components of the circuit. A capacitor produces such an electric potential difference between its two leads when electrons are moved from one side to the other. Since our system con-

sists of neutral particles, electric potential will not produce a force on the atoms. Instead, we will look at the chemical potential difference between the two reservoirs as an analog to the electric potential difference.

In the electronic capacitor, the amount of energy needed to move a charge from one plate of the capacitor to the other is equal to the charge times the electric potential difference between the plates [26]. Similarly, the energy needed to move a small group of atoms from one of our reservoirs to the other is equal to the number of atoms being moved times the difference in chemical potential between the reservoirs [27]. In the BEC case, the local mean field of the atoms in a reservoir is the same as the chemical potential of the atoms in that reservoir, except for some offset value due to the external potential. As long as there is no offset in external potential between the reservoirs, and we are only worried about the difference in chemical potential between the reservoirs, this distinction is unnecessary. Since this is the case in our system, unless otherwise noted the chemical potential will be defined in this thesis as the local mean field when discussing quantum systems. The classical thermodynamically calculated chemical potential is used for thermal systems.

In the electronic capacitor, if we start with equal charge on both plates, and then move an amount of charge  $Q$  from one plate to the other, we can write the electric potential difference  $\Delta V$  between the two plates as

$$\Delta V = \frac{Q}{C}, \tag{2.1}$$

where  $C$  is the value of the capacitance [28].

In our system, we will start with an equilibrium number  $N_e$  of atoms in either reservoir. We then move a number of atoms  $N$  from one reservoir to the other. This will produce a chemical potential difference  $\Delta\mu$  between the reservoirs. In the limit of this chemical potential difference being linear in this atom number imbalance  $N$ , we can use the constant of proportionality to define our chemical capacitance exactly as in equation 2.1:

$$\Delta\mu = \frac{N}{C_c} \rightarrow C_c = \frac{N}{\Delta\mu}. \quad (2.2)$$

This linear approximation is valid over a large range of number imbalance, as can be seen further down in figure 2.5 where we derive the capacitance of a BEC system with this geometry. Thus to calculate the capacitance of our system, we only need to know the form of the chemical potential as a function of atom number for one of the reservoirs in our trap.

### 2.2.1 Capacitance in a BEC System

The form of the chemical potential in a BEC system will depend heavily on the details of the experiment. If our system is hard walled in two dimensions and harmonic in the third, as we expect for the ideal case in our experiment, the chemical potential of atoms in either reservoir will be proportional to  $N_i^{2/3}$  when calculated using the Thomas-Fermi approximation to the Gross-Pitaevskii equation of the system [29]. Since our system will not be ideal, and the walls will be somewhat soft, we need to make an adjustment to that form. If we go all the way to the limit of totally soft walls, and assume a 3D harmonic potential shape, the chemical potential of

atoms in either reservoir will then be proportional to  $N_i^{2/5}$ . Since we are somewhere between these two limits, we will model our chemical potential as  $\mu_i = \beta N_i^{\gamma_\mu}$ .

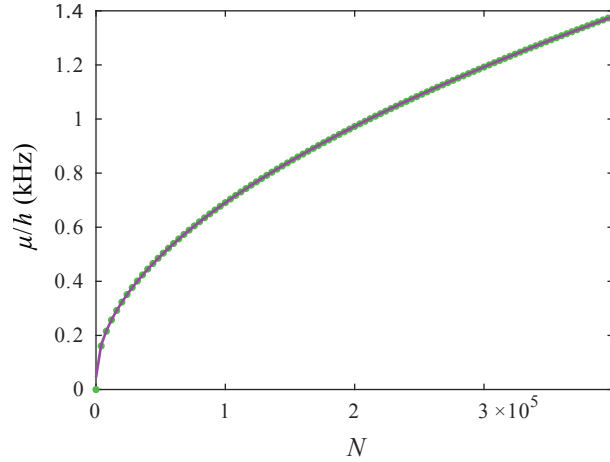


Figure 2.2: A plot of the numerically calculated chemical potential of a BEC in one reservoir of the model potential given in equation 3.1 is plotted as the green dots. A fit of this numerical data to our model form of the chemical potential,  $\mu_i = \beta N_i^{\gamma_\mu}$ , is shown with the red line. For our parameter range,  $\gamma_\mu \approx 0.51$ .

In section 3.1.7.2, we show how we model our reservoir potential. By numerically solving the Gross-Pitaevskii equation with this potential form, we can get a numerical value of chemical potential for any given atom number. In figure 2.2, we fit this numerical calculation to the form discussed here. The chemical potential of atoms in one reservoir is plotted in normalized coordinates in figure 2.3. The chemical potential of both reservoirs as a function of the number balance is plotted in figure 2.4, and their difference in figure 2.5. All three of these plots take a value of  $\gamma_\mu = 0.51$ , which is approximately what we find for our particular system.

We can derive our BEC capacitance by looking at the difference in chemical potential between the two reservoirs for a given atom number imbalance  $N$ . With

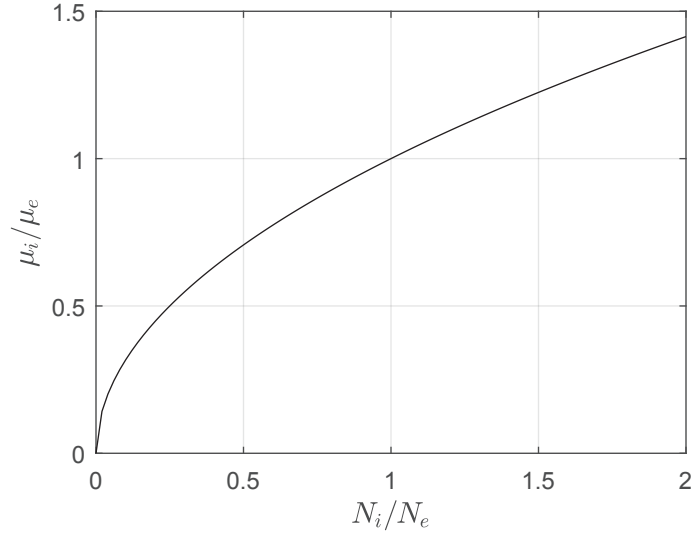


Figure 2.3: The chemical potential of a BEC in one of our reservoirs as a function of atom number in normalized units. The atom number can vary from zero to twice the equilibrium number in the experiment. This example is for a model chemical potential of  $\mu_i = N_i^{0.51}$ .

$N_e + N$  atoms in one reservoir, and  $N_e - N$  atoms in the other reservoir, our chemical potential difference is given by

$$\Delta\mu = \beta ((N_e + N)^{\gamma_\mu} - (N_e - N)^{\gamma_\mu}) \approx (\beta N_e^{\gamma_\mu}) 2\gamma_\mu \frac{N}{N_e} = 2\gamma_\mu \frac{\mu_e - \alpha}{N_e} N, \quad (2.3)$$

an example of which is plotted in figure 2.5. For a value of  $\gamma_\mu = 0.51$ , which is typical for our experiment, this linear approximation represents an error in chemical potential of less than 10% for a number imbalance up to  $|N/N_e| < 0.80$ . Our capacitance is then given by

$$C_{c,BEC} = \frac{N_e}{2\gamma_\mu (\mu_e - \alpha)}. \quad (2.4)$$

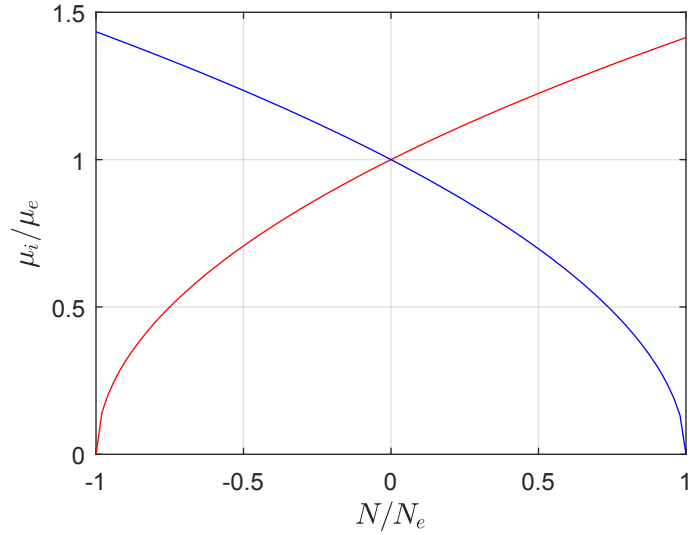


Figure 2.4: The chemical potential of a BEC in both the left (red curve) and right (blue curve) reservoirs in normalized units as a function of the atom number imbalance  $N$ . This example is for a model chemical potential of  $\mu_i = N_i^{0.51}$ .

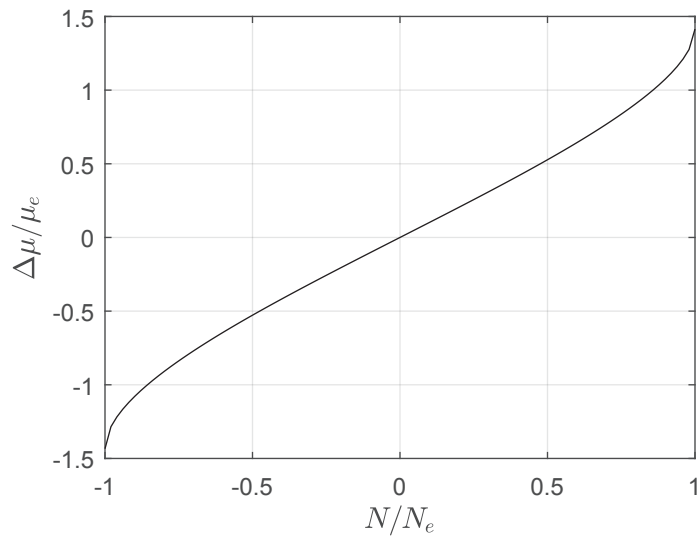


Figure 2.5: The difference in chemical potential between our two reservoirs in normalized units as a function of number imbalance  $N$ . This example is for a model chemical potential of  $\mu_i = N_i^{0.51}$ .

## 2.3 Kinetic Inductance

In an electronic circuit, normal or superconducting, an inductor stores energy. The amount of energy  $E$  stored in the inductor is proportional to the square of the current  $I$  flowing through it:

$$E = \frac{1}{2}I^2L, \quad (2.5)$$

where  $L$  is the inductance of the inductor.

In our system, we have atoms flowing through the channel. Since the atoms are moving, they have a total kinetic energy which we will represent as  $K$ . This energy is equal to the number of atoms in the channel  $N_{ch}$  times the kinetic energy of each atom  $\frac{1}{2}mv^2$ , where  $m$  is the mass of an atom, and  $v$  is the velocity of the atoms. We can rewrite both  $N_{ch}$  and  $v$  in terms of the length of the channel  $l$ , the one dimensional (1D) density of atoms in the channel  $n_{1D}$ , and the current through the channel  $I = \frac{dN}{dt}$ :

$$N_{ch} = ln_{1D}; \quad (2.6)$$

$$v = \frac{I}{n_{1D}}. \quad (2.7)$$

Now, we can write the kinetic energy of the atoms moving in the channel as

$$K = N_{ch}\frac{1}{2}mv^2 = (ln_{1D})\frac{1}{2}m\frac{I^2}{n_{1D}^2} = \frac{1}{2}I^2\left(\frac{ml}{n_{1D}}\right). \quad (2.8)$$

Comparing this to equation 2.5 we can see that the inductance in the channel of our system is given by

$$L_k = \frac{ml}{n_{1D}}. \quad (2.9)$$

This entire argument can also be applied to the kinetic energy of electrons flowing in a wire, and in fact this inductance can be seen in electronic circuits, where it is called the kinetic inductance. Generally it is too small compared to magnetic inductance to be measured, but for some superconducting circuits it is a measurable quantity [30].

## 2.4 Dissipation

In the absence of dissipation, this inductance combined with the capacitance will give rise to LC oscillations with frequency

$$\omega_{LC} = \frac{1}{\sqrt{LC}}, \quad (2.10)$$

exactly as seen in an electronic LC circuit [28]. Due to the constriction of the channel, however, there are potential sources of dissipation that will damp this oscillation.

### 2.4.1 A Superfluid Weak Link

We model the system that we have as the circuit shown in figure 2.6, with our already derived capacitor and inductor in series with some dissipative element. We will model this dissipative element as a resistance-shunted weak link, or Josephson junction. The weak link will set a critical current  $I_c$ , with any additional current flowing through the resistor [31]. This circuit can be described by the following

three differential equations:

$$\frac{dN}{dt} = I, \quad (2.11)$$

$$\hbar \frac{d\gamma}{dt} = \Delta\mu = R [I - I_c f(\gamma)], \quad (2.12)$$

$$L_k \frac{dI}{dt} = - \left[ \frac{N}{C_c} + \Delta\mu \right] = - \left[ \frac{N}{C_c} + R (I - I_c f(\gamma)) \right], \quad (2.13)$$

where  $\hbar$  is the reduced Planck constant,  $\gamma$  is the phase difference between the two reservoirs, and  $I_c f(\gamma)$  is the current-phase relation of the link.

Physically, equation 2.11 defines the current flow between the two reservoirs, and equation 2.13 describes the dynamics caused by the series capacitor and inductor described above. The physical motivation for the form of equation 2.12 comes from two things. The  $I_c f(\gamma)$  term on the right side of the equation is the basic description of superfluid flow, with the phase difference between the reservoirs driving flow. The  $RI$  term on the right side of the equation describes basic dissipation for any flow over the critical current of the system. If the total current is less than the critical current, no dissipation will occur. There will also be a separate resistance parallel to the capacitor due to dissipation in the thermal fraction of atoms. We expect that this is extremely small in our system, however, and it is left out here. A quantitative description of the thermal dissipation below justifies this assumption.

These equations can be numerically integrated to fit the dynamics we will measure in the experiment with three independent parameters,  $\tau = RC$ ,  $\omega^2 = 1/L_k C_c$ , and  $I_c$ . Since we can calculate the capacitance *a priori*, fitting these parameters gives us the experimental values of the three relevant circuit elements,  $R$ ,  $L_k$ , and  $I_c$ . We could similarly use our calculated inductance value as given and experimen-

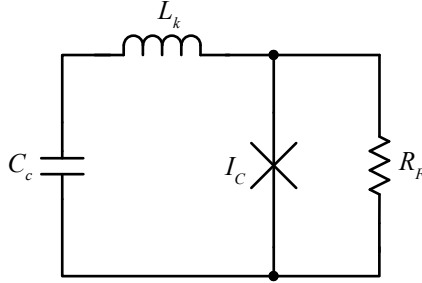


Figure 2.6: A diagram of the the circuit we will use to model our system. It consists of a capacitor that is discharged through an inductor in series with a resistance shunted weak link (Josephson-Junction). We calculate the expected values for these circuit elements and compare to the dynamics that we observe in our BEC trapped in a dumbbell shaped potential.

tally compare our capacitance, however due to the limitations in our knowledge of the exact shape of the potential in the channel there is more uncertainty in the validity of this value.

#### 2.4.2 Superfluid Dissipation - Feynman Resistance

When the superfluid in our system flows above its critical current, we will observe dissipation due to energy from the BEC being coupled into collective excitations. While we cannot create a simple model to describe all of the possible excitations, we can quantify the rate of dissipation due to collective excitations in the form of vortices. The argument that we will follow is that proposed by Richard Feynman [23] when discussing vortices in superfluid helium. This argument considers a geometry as shown in figure 2.7, with a channel of superfluid flowing out into an infinite, uniform reservoir. Since we are ignoring other collective excitations, we

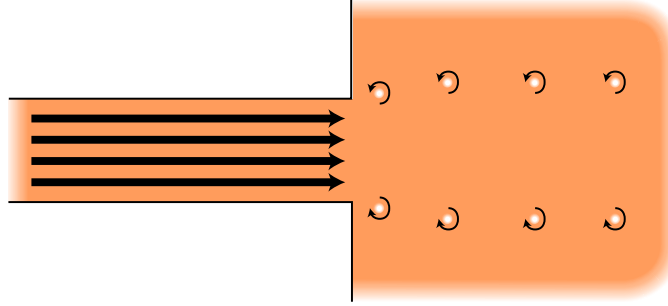


Figure 2.7: A schematic representing the situation described by Feynman [23] in deriving the critical velocity for vortex creation and vortex production rate in a superfluid gas. The system consists of a channel with superfluid flow exiting into an infinite reservoir. Vortices are created at either side of the channel aperture at a calculable rate, allowing us to determine the rate of energy dissipation in the system. Our actual system is an approximation of this, with walls that are not infinitely hard, and reservoir not infinitely large.

expect that any derived resistance (conductance) will be lower (higher) than what will be observed experimentally. Similarly, our derived critical current is expected to be higher than what we should observe.

This model, in addition to estimating the critical velocity for vortex production,

$$v_c = \frac{\hbar}{mw} \ln \left( \frac{w}{\xi} \right), \quad (2.14)$$

calculates the rate of vortex pair production,

$$\gamma_p = \frac{v^2 m}{2\pi\hbar} = \frac{I^2 m}{2\pi\hbar n_{1D}^2}, \quad (2.15)$$

where  $v$  is the flow velocity,  $I$  is the atom number current,  $n_{1D}$  is the 1D density of atoms in the channel,  $w$  is the width of the channel, which is equal to the separation of the created vortices, and  $\xi = \sqrt{\hbar^2/m\mu}$  is the healing length of the superfluid,

with chemical potential  $\mu$ .

For a superfluid with 2D density  $n_{2D}$ , we can also estimate the energy of a pair of vortices separated by a distance  $w$  as

$$E_p = \frac{\pi n_{2D} \hbar^2}{m} \ln \left( \frac{w}{\xi} \right). \quad (2.16)$$

This calculation is for a vortex anti-vortex pair in a homogeneous BEC. To account for our finite geometry, we can use a method of images similar to that used in electromagnetism [26] to numerically calculate the energy of a pair of vortices close to the wall of a circularly contained BEC. This calculation involves introducing image vortices outside of the reservoir such that the velocity field satisfies the boundary condition that it is tangent to the edges of the reservoir. This results in an energy that is greater than that given in equation 2.16 by a factor of  $\kappa \approx 1.7$  for our particular geometry. Since the vortex pairs will be created at either side of the channel, we use the channel width  $w$  as the vortex pair separation in this calculation. It is also possible that vortices will be created at the entrance to the channel, however this is not treated in this analysis. Since we do not see excitation in the initially full reservoir in the experiment, we expect that contributions due to this would be small.

From equations 2.15 and 2.16, the rate of energy dissipation in the system will be

$$P = \kappa \gamma_p E_p = \kappa I^2 \frac{\hbar n_{2D}}{2n_{1D}^2} \ln \left( \frac{w}{\xi} \right). \quad (2.17)$$

The power dissipated by a current through a resistor is given by

$$P = I^2 R_F. \quad (2.18)$$

Comparing equations 2.17 and 2.18, we can now define the Feynman resistance in our system as

$$R_F = \frac{1}{G_F} = \kappa \frac{\hbar n_{2D}}{2n_{1D}^2} \ln \left( \frac{w}{\xi} \right), \quad (2.19)$$

where  $G_F$  is our expected conductance due to this dissipation mechanism. We take the equilibrium value of the chemical potential to determine  $\xi$ . Since we can write  $n_{1D} \approx wn_{2D}$ , our conductance should be approximately proportional to  $n_{1D}$ . This dissipation will only be seen when the current is above the critical current. Below this value, there will be no dissipation. Using equation 2.14 and the density of atoms in the channel  $n_{1D}$ , we can write down this expected critical current

$$I_c = v_c n_{1D} = \frac{\hbar n_{1D}}{mw} \ln \left( \frac{w}{\xi} \right). \quad (2.20)$$

### 2.4.3 Dissipation in a Thermal Gas

In our experiment, we expect that the thermal fraction of atoms will be very low, and any contribution to the dissipation from this thermal fraction will be too small to measure. We can, however, look at a similar system consisting only of an ideal thermal gas. We show that dissipation in this system will be similar to the Sharvin resistance [25] seen in electronics, where a point contact smaller than the mean free path of the electrons restricts current flow. This system can be modeled completely with a classical kinetic theory as follows.

The normalized 2D velocity distribution of the thermal atoms in the system is given, in cylindrical coordinates, by [30]

$$f_{2D}(v, \theta) dv d\theta = \left( \frac{m}{2\pi kT} \right) v e^{-\frac{mv^2}{2kT}} dv d\theta. \quad (2.21)$$

Integrating this times  $n_{2D}wv_x = n_{2D}wv \cos \theta$ , gives us the effusion rate  $F$  at which atoms will leave a reservoir with a hole in the side with width  $w$ ;

$$F = \int_{\pi/2}^{\pi} \int_0^{\infty} n_{2D}w \left( \frac{m}{2\pi kT} \right) v^2 \cos \theta e^{-\frac{mv^2}{2kT}} dv d\theta = \sqrt{\frac{kT}{2\pi m}} n_{2D}w. \quad (2.22)$$

Since atoms will also be entering the first reservoir due to leaving the second reservoir, the total rate of change in atom number in reservoir 1 can then be written as

$$\dot{N}_1(t + \Delta t) = -F_1(t + \Delta t) + F_2(t), \quad (2.23)$$

where the second term on the right hand side of the equation, representing the rate that atoms enter reservoir 1 due to leaving reservoir 2, is evaluated at a time  $\Delta t$  earlier. This delay is due to the finite velocity of the atoms traversing the channel. To calculate this delay time, we need to know the velocity distribution of the atoms within the channel, which will be  $f_{ch}(v, \theta)dv d\theta = v_x f_{2D}(v, \theta)dv d\theta$ , normalized such that

$$\int_{-\pi/2}^{\pi/2} \int_0^{\infty} f_{ch}(v, \theta)dv d\theta = 1. \quad (2.24)$$

Carrying out this normalization gives

$$f_{ch}v, \theta dv d\theta = \frac{1}{\sqrt{2\pi}} \left( \frac{m}{kT} \right)^{3/2} v^2 \cos \theta e^{-\frac{mv^2}{2kT}} dv d\theta. \quad (2.25)$$

The average velocity along the axis of the channel, of atoms in the channel, is thus given by

$$\langle v_x \rangle = \int_{-\pi/2}^{\pi/2} \int_0^{\infty} v \cos \theta f_{ch}(v, \theta)dv d\theta \quad (2.26)$$

$$= \frac{1}{\sqrt{2\pi}} \left( \frac{m}{kT} \right)^{3/2} \int_{-\pi/2}^{\pi/2} \int_0^{\infty} v^3 \cos^2 \theta e^{-\frac{mv^2}{2kT}} dv d\theta \quad (2.27)$$

$$= \sqrt{\frac{\pi kT}{2m}}. \quad (2.28)$$

This gives us the average time for an atom to traverse the channel,

$$\langle \Delta t \rangle = \frac{l}{\langle v_x \rangle} = l \sqrt{\frac{2m}{\pi kT}}, \quad (2.29)$$

where  $l$  is the length of the channel. Equation 2.23 then becomes

$$\dot{N}_1(t + \Delta t) = \frac{w}{A} \sqrt{\frac{kT}{2\pi m}} (-N_1(t + \Delta t) + N_2(t)), \quad (2.30)$$

where  $A$  is the area of either reservoir, taken to be equal for our system. If we expand this linearly around  $t$ , we can again rewrite this as

$$\dot{N}_1(t) + \Delta t \ddot{N}_1(t) = \frac{w}{A} \sqrt{\frac{kT}{2\pi m}} (-N_1(t) - \Delta t \dot{N}_1(t) + N_2(t)). \quad (2.31)$$

Substituting in our definitions,  $N_1 = N_e - N$  and  $N_2 = N_e + N$ , we now have

$$-\dot{N}(t) - \Delta t \ddot{N}(t) = \frac{w}{A} \sqrt{\frac{kT}{2\pi m}} (-N_e + N(t) + \Delta t \dot{N}(t) + N_e + N(t)) \quad (2.32)$$

$$= \frac{w}{A} \sqrt{\frac{kT}{2\pi m}} (2N(t) + \Delta t \dot{N}(t)). \quad (2.33)$$

We can rewrite this as

$$\frac{2kT}{n_e A} N(t) = -\frac{\sqrt{2\pi m kT}}{n_e w} \left(1 + \frac{wl}{\pi A}\right) \dot{N}(t) - \frac{2ml}{n_e w} \ddot{N}(t). \quad (2.34)$$

For our approximations used above to hold, the area of the channel,  $A_{ch} = wl \ll A$ .

We can also calculate the chemical potential of the thermal atoms in either reservoir as [30]

$$\mu = kT \ln \left[ n_{2D} \left( \frac{h^2}{2\pi m kT} \right) \right], \quad (2.35)$$

where  $k$  is Boltzmann's constant,  $h$  Planck's constant,  $T$  the temperature,  $n_{2D}$  the 2D number density and  $m$  the mass of a particle in the gas. The difference in

chemical potential between either reservoir is then given by

$$\Delta\mu = kT \ln \left( \frac{n_{2,2D}}{n_{1,2D}} \right) = kT \left\{ \ln \left[ \left( \frac{N_e}{A} \right) \left( 1 + \frac{N}{N_e} \right) \right] - \ln \left[ \left( \frac{N_e}{A} \right) \left( 1 - \frac{N}{N_e} \right) \right] \right\} \quad (2.36)$$

$$\approx \frac{2kT}{n_{e,2D}A} N. \quad (2.37)$$

This linear approximation is valid for  $N \ll N_e$ . Combining equations (2.1) and (2.37) leads to an expression for our chemical capacitance of the thermal system,

$$C_c = \left( \frac{n_e A}{2kT} \right) = \frac{n_e A}{2\varepsilon_T}, \quad (2.38)$$

where  $\varepsilon_T \equiv kT$  is the thermal energy of the gas.

If we now substitute equation 2.38 into equation 2.34, we can simplify this expression further;

$$\frac{N(t)}{C_c} = -\frac{\sqrt{2\pi mkT}}{n_e w} \dot{N}(t) - \frac{2ml}{n_e w} \ddot{N}(t). \quad (2.39)$$

When we compare this to the Kirchoff equation for a series RLC circuit [28],

$$\frac{Q}{C} = -R\dot{Q} - L\ddot{Q}, \quad (2.40)$$

with resistance and inductance given by

$$R = \frac{2 \langle p_{2D} \rangle}{n_e w} = \frac{2 \langle p_{2D} \rangle}{n_{1D}} \quad \text{and} \quad L_c = \frac{2ml}{n_e w}, \quad (2.41)$$

where

$$\langle p_{2D} \rangle = \int_{-\pi/2}^{\pi/2} \int_0^\infty m v f_{2D}(v, \theta) v dv d\theta = \sqrt{\frac{\pi m k T}{2}} \quad (2.42)$$

is the average magnitude of the 2D momentum of the particles in the system.

As we can see, the inductance derived for the thermal part of the system is almost identical to the form of the kinetic inductance, except for a factor of two. This factor likely comes about for two reasons. First, we are using the average velocity of atoms traveling down the channel as a single value approximating the velocity for all particles. Secondly, we are taking only the first term in the expansion about this time delay in equation 2.31.

For a 2D, electronic system the Sharvin resistance is given by [32]

$$R_S = \frac{\pi}{2} \frac{p_F}{e^2 n w}, \quad (2.43)$$

where  $p_F = \hbar\sqrt{2\pi n_e}$  is the Fermi momentum. Physically, this resistance is due to the ballistic movement of electrons, and the statistical likelihood of them entering a small point contact. This has the same form as our resistance in equation (2.41), differing by a factor of  $e^2$  and a numerical factor because the Sharvin resistance is derived for a 2D, charged,  $T = 0$  Fermi gas, which has a different velocity distribution than our neutral, classical gas.

We verify this functional form in a purely thermal system, and as we will later show for our BEC system, this ballistic resistance in the thermal fraction will not contribute significantly to the overall dissipation that we observe.

## Chapter 3: Apparatus

### 3.1 BEC Apparatus

To experimentally test the model we have formed, we use a BEC of sodium atoms. The BEC is created using standard atomic physics methods, including a Zeeman slower, dark-spot Magneto-Optical Trap (MOT), quadrupole magnetic trap, time-orbiting potential (TOP) trap, optical dipole traps (ODT), and multiple forms of evaporative cooling. A full description of the steps from MOT to BEC are given elsewhere [33]. The basic concepts of these methods are described in appendix A of this thesis, and detailed descriptions can be found in atomic physics textbooks [29, 34]. The portions of the apparatus that are unique to this experiment are described here. Figure 3.1 shows a schematic of the overall vacuum system used to create the BEC, including the important parts that will be discussed below. This system is capable of achieving base pressures of  $\approx 10^{-11}$  Torr, providing trap lifetimes well in excess of the duration of the atom circuit dynamics studied.

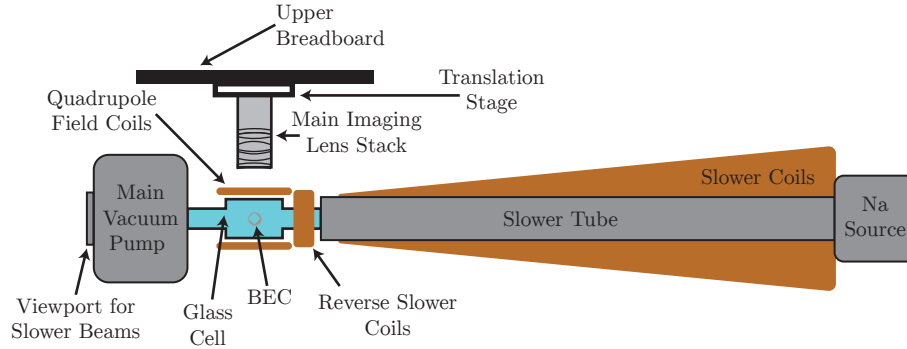


Figure 3.1: Schematic of the vacuum system used to create the sodium BEC. The system consists of a sodium source or oven, a Zeeman slower, the main experimental glass cell, and the main pump, which is a combination ion and titanium sublimation pump. This system achieves base pressures of  $\approx 10^{-11}$  Torr. Also shown are the coils used to create the Zeeman slower and quadrupole magnetic fields, and the main imaging lens stack mounted to the underside of the upper optical breadboard discussed below. It is attached with a 2-axis translation stage to aid in aligning the lens stack properly.

### 3.1.1 Laser System

The main laser system for the sodium BEC apparatus, shown in figures 3.2 and 3.3, is based on a Toptica DL-SHG Pro frequency doubled laser. This laser is capable of producing 2 W of usable light at 589 nm. This laser is locked to the necessary frequency using a saturated absorption (SA) spectroscopy system using a phase-sensitive detection scheme. For this, a small amount of power is taken from the laser output and sent to the SA setup after being frequency modulated at 10 kHz using a double-passed acousto-optic modulator (AOM). The output of this AOM (AOM-1 in figure 3.2) is actively intensity stabilized using a proportional-integral controller with a bandwidth higher than the 10 kHz modulation to avoid unwanted

intensity fluctuations in the SA setup. The signal from the SA setup is then mixed with the reference frequency using a lock-in amplifier. The output of this gives a differential signal, allowing us to use a proportional-integral controller, with output fed back to the laser frequency modulation input, to lock to the known frequency at a peak in the normal SA signal.

The now frequency locked laser output is then split up into three separate beams. The first of these is used to produce the MOT trapping light, with AOM-2 used in a double-pass setup, which is coupled to an optical fiber. When not being used for MOT light, the zero-order of the first pass through this AOM is fed through AOM-3 in a single pass setup, and coupled into another optical fiber to be used as the probe beam for absorption imaging.

The second beam from the laser output is sent through AOM-6 in a single pass to produce light at the frequency necessary for the Zeeman slower, which is coupled into an optical fiber. Part of this frequency shifted beam is also sent through AOM-4, which is a specially made 1.8 GHz Brimrose AOM, to produce light near the repump frequency necessary for our traps. This is sent through AOM-5 to produce the frequency needed for the MOT and imaging repump, with the zero-order output of AOM-5 being coupled into the same fiber as the slower beam, to be used as repump for the slower.

The final beam from the laser output is sent to a wavemeter for rough measurement of the laser wavelength. A schematic of all of the frequency shifts used in the experiment are shown in figure [3.4](#).

In addition to the trapping light, there are also two separate lasers used for

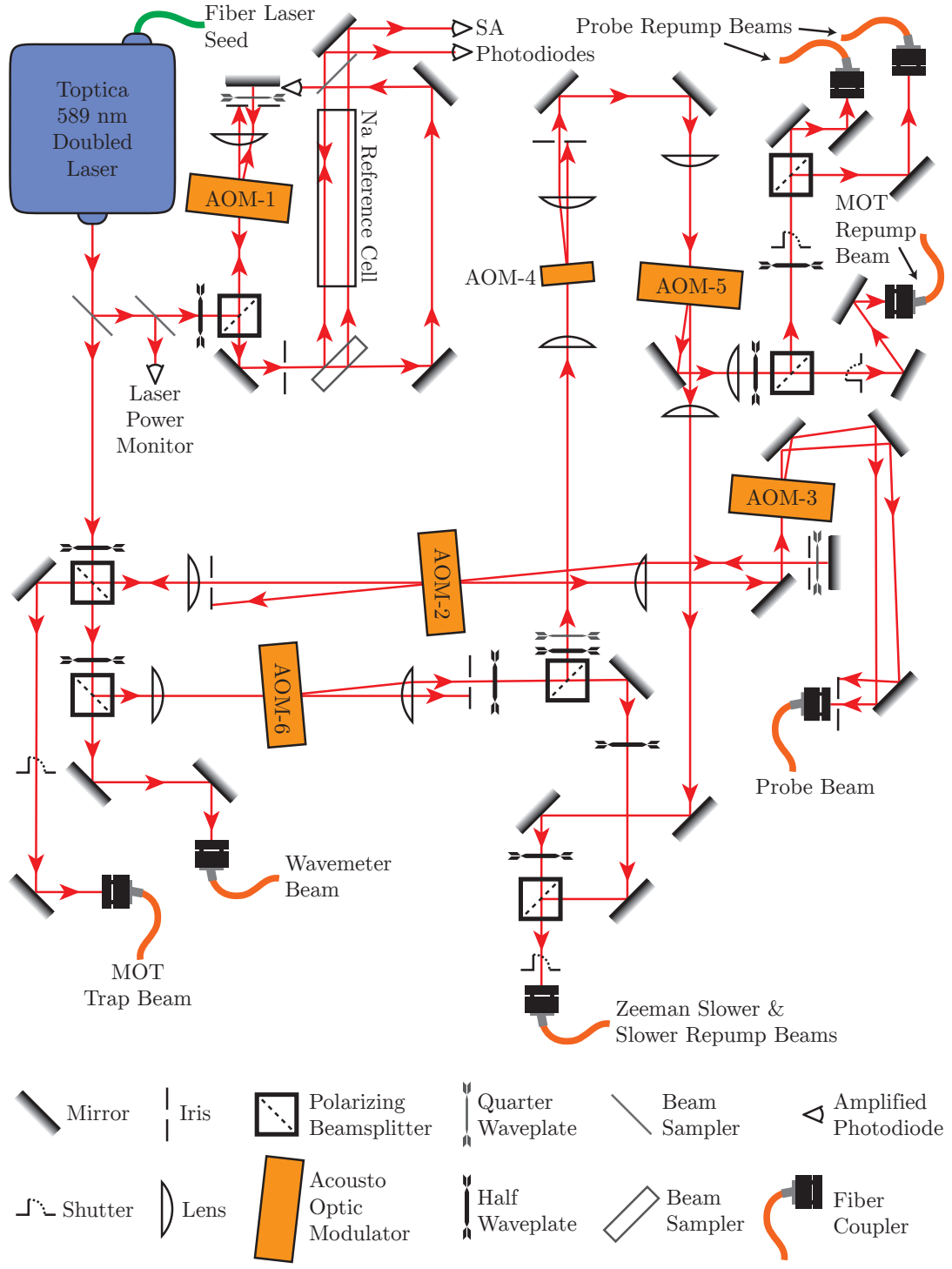


Figure 3.2: Schematic of the setup of the laser used to produce the light for the Zeeman slower, MOT, and imaging for the Na BEC. Various AOMs and shutters allow us to control the frequencies and powers of the various beams with enough precision to carry out the experiment.

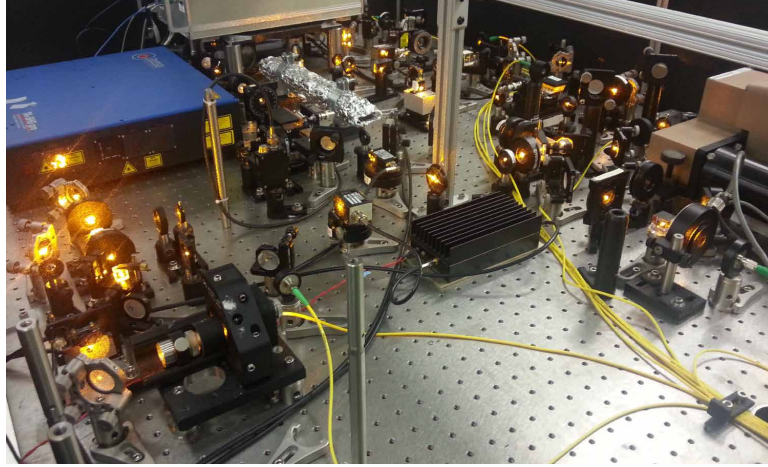


Figure 3.3: Image of the setup of the laser used to produce the light for the Zeeman slower, MOT, and imaging for the Na BEC. Various AOMs and shutters allow us to control the frequencies and powers of the various beams with enough precision to carry out the experiment. A full description of the system is given in the text.

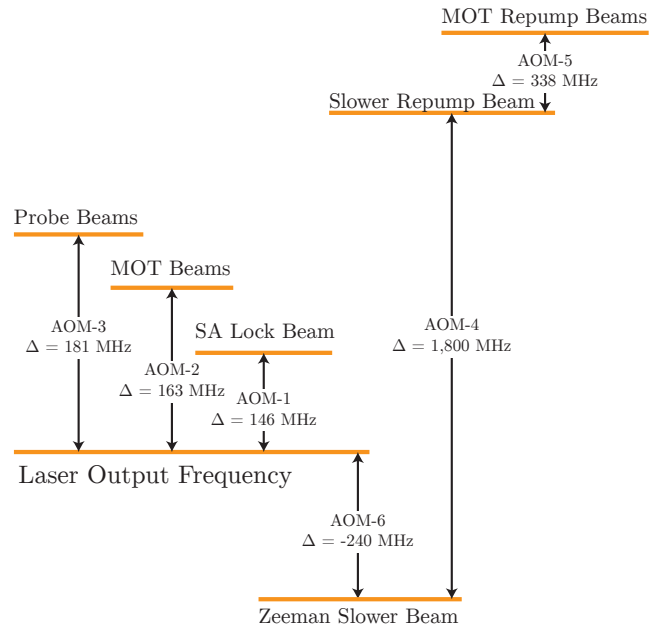


Figure 3.4: Schematic showing the various frequency shifts used to create the necessary beams for the experiment.

the ODTs in the system which are not shown in figure 3.2. The first is a red-detuned, IPG fiber laser (1064 nm) run at approximately 5 W. This is split into two beams, frequency shifted from each other by an amount on the order of 10 MHz to avoid interference where they will eventually cross. These are fiber coupled to the experimental table. The first of these beams is made into a horizontal sheet to vertically confine the atoms. The second is crossed with this sheet to produce the original trap from which the dumbbell potential is loaded. The other ODT laser is a blue detuned (532 nm), Coherent diode pumped solid state laser. About 1 W of the light from this laser is used to create two separate dipole potentials. The first of these creates our dumbbell shaped potential. The other is aimed with a 2D acousto-optic deflector (AOD) to create a barrier over the channel of the dumbbell. All of the ODT beams are actively amplitude locked using feedback from photodiode power monitors as close to the experimental chamber as possible. Shutters are also installed on the laser table side of the fiber to allow complete shutoff of the beams when not in use.

### 3.1.2 Main Experimental Optical Breadboard

Once the atoms are transferred out of the MOT, the majority of the optical access to the atoms is taken through the vertical direction. The exception to this is the horizontal sheet ODT. The mask, AOD, and Laguerre-Gauss (LG) beams are all combined on the breadboard above the cell before being sent down through the main imaging lens stack, which is just above the BEC. The imaging beam also travels along

the same path, counterpropagating with these beams, and is split off on the same upper breadboard before being sent to the imaging camera. Each of these beams has a separate object plane on the upper breadboard which is imaged to the BEC plane. The imaging and LG beamlines are combined on a dichroic plate optic since they are of sufficiently different wavelengths. The two green beams are combined using a polarizing beamsplitter cube. These two sets of beams are combined on a 50/50 beamsplitter cube and sent through the imaging stack, which provides an numerical aperture (NA) of about 0.2. A schematic of the upper breadboard is shown in figure 3.5, and a picture of the actual setup with beamlines and important elements highlighted is shown in figure 3.6.

### 3.1.3 Computer Control

The timing of the sodium BEC apparatus is controlled mainly by a pair of PulseBlaster digital out cards in a master-slave setup. Each card has 24 TTL-level outputs which connect to the various triggers, switches and shutters in the system. Each digital channel is buffered using a HCPL-7720 optocoupler. One of the outputs from the master PulseBlaster is connected to trigger the slave PulseBlaster, and another is connected to trigger the two PCI-6713 analog output cards which control various analog parameters of the system. Due to the long experimental run time ( $\sim 30$  s) and small minimum timestep ( $\sim 100$  ns), directly writing the waveforms for each analog and digital channel is not feasible from a memory limit standpoint. The PulseBlaster, however, avoids the need for this by instead allowing us to write

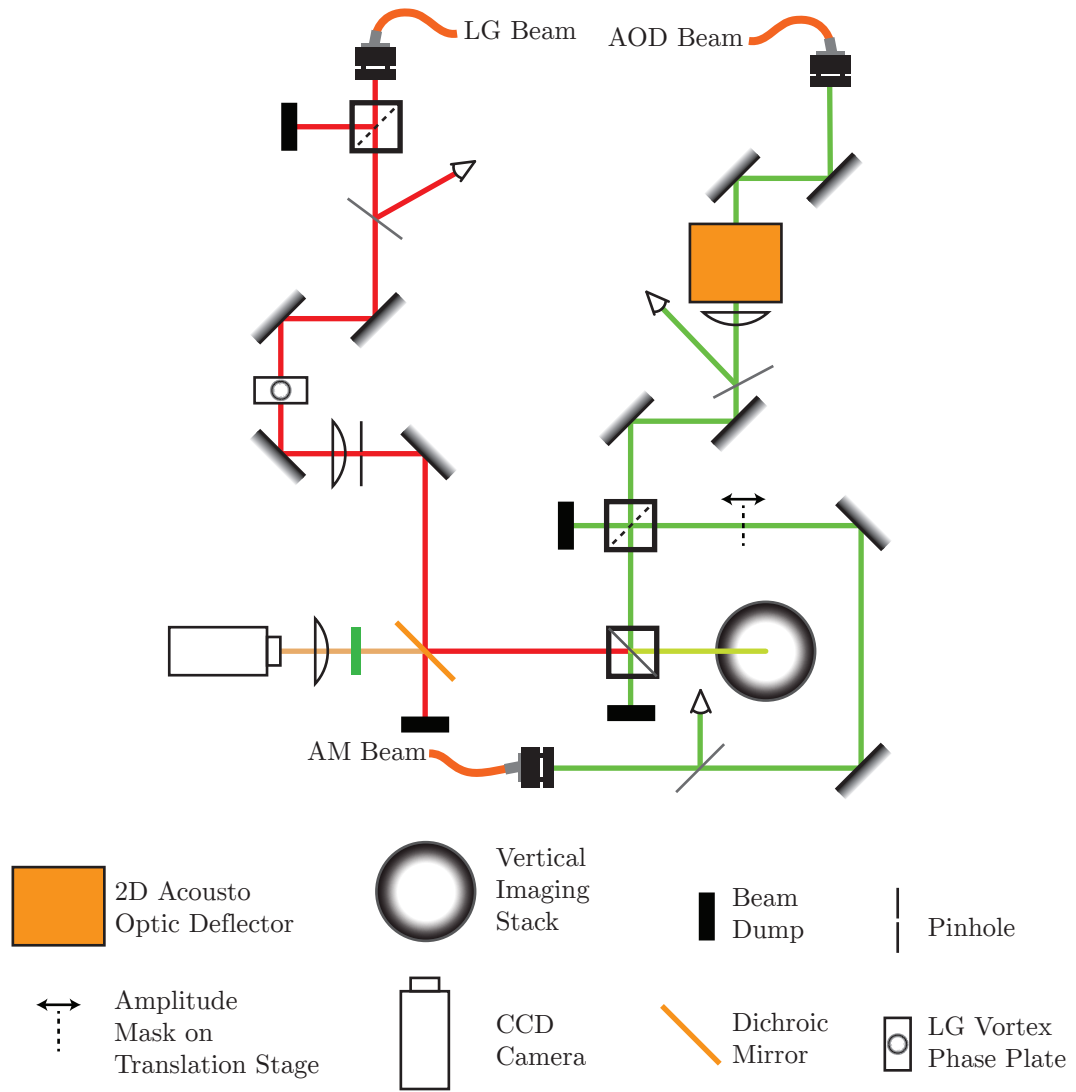


Figure 3.5: Schematic of the optics used to combine the various trapping and imaging beams on the optical breakboard located above the experimental chamber. A full description of the system is given in the text.

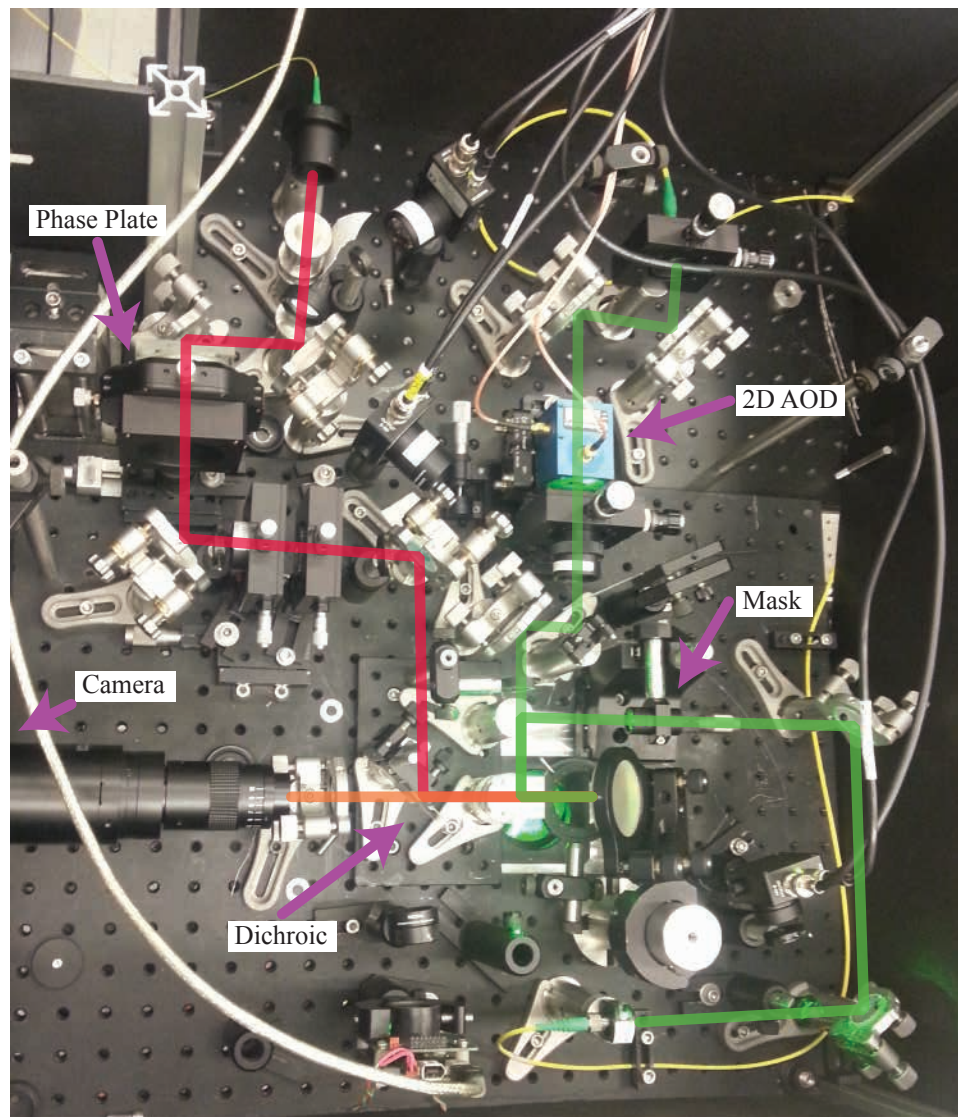


Figure 3.6: Image of the upper optical breadboard of the BEC apparatus with artificial highlighting. The green AOD and mask beams are highlighted in green, the infrared (IR) LG beam is highlighted in red, and the yellow imaging beam is highlighted in orange. The main elements of the setup are also labeled. The main imaging lens stack is below this breadboard, above the BEC chamber.

each step in the sequence as a state with a duration. For the analog cards, rather than running on a continuous clock, an output from the master PulseBlaster is used as the trigger. With this setup, we are able to write the waveform for the analog channels for only the times when they change, rather than for each timestep throughout the experiment. To create the sequences and waveforms for the digital and analog cards, we use a recent version of the SetList LabVIEW program created and maintained at the Joint Quantum Institute at the University of Maryland and the National Institute of Standards and Technology.

### 3.1.4 Imaging

To image the sodium BEC, we used a variation of absorption imaging known as partial-transfer absorption imaging [35] discussed in more detail in appendix A. In this technique, the atoms are imaged using on-resonant absorption imaging. To avoid the saturation of the probe imaging beam that would happen if we imaged all of the atoms, we keep the atoms in the  $F = 1$  dark ground state throughout the experiment, and immediately before imaging, we transfer a known fraction of atoms from to the  $F = 2$  imaging ground state. By adjusting the transferred fraction depending on the parameters of the particular experimental run, we are able to keep the optical density in the measured regions very close to the same value. This allows us to avoid many of the nonlinearities associated with on-resonant imaging due to saturation and bleaching.

### 3.1.5 Cooling Sequence

The full cooling sequence used for the sodium BEC apparatus follows a standard magnetic TOP trap technique, followed by final cooling in a crossed dipole trap, which is our dumbbell potential. Initially, a Zeeman slower is used to load a dark-spot MOT in the ultra-high vacuum (UHV) chamber.

The magnetic quadrupole field of the MOT is then ramped up while the cooling lasers are switched off to load as many as possible of the MOT atoms into a purely magnetic trap. Once in the magnetic trap, RF evaporation is used to cool the atoms close to a point where spin-flip losses at the center of the trap become important. At this point, a rotating bias field is applied with a frequency on a time scale that is fast compared to atomic motion but low compared to splitting of the Zeeman levels of the system, producing what is known as a TOP trap. The level of this bias field is then ramped down, producing a “circle-of-death” evaporation. This is followed by an additional RF evaporation step to condense the atoms into a BEC. The BEC is then transferred to the ODT by ramping the magnetic trap down while the intensity ODT beams is ramped up.

The dipole trap used at this point consists of a horizontal red detuned sheet beam, which is also the final vertical confining potential in the experiment, and a vertical, focused, red detuned LG beam. While this particular experiment does not require that this beam be an LG profile, it existed in the apparatus to be used for other experiments, and did not alter anything for this experiment. A simple Gaussian beam could have been substituted with no effect.

The intensity of the sheet beam is then ramped down as the final evaporation step used to set the final temperature and condensate fraction. This produces a BEC at a temperature of approximately 100 nK. Measurement of the temperature was carried out by imaging the BEC in a direction parallel to the sheet. The optical density in this direction is large enough that the thermal fraction can be observed, and a temperature measurement can thus be made. This is not possible when imaging in the vertical direction due to the significantly lower optical density of the cloud in this direction. The critical temperature for our system is estimated to be approximately 500 nK, and our thermal fraction is thus  $< 5\%$ . The final number of atoms that are used in the experiment is set by adjusting the length of time the atoms are held at this point.

Finally, this BEC is transferred to the dumbbell potential by ramping up the intensity masked ODP and AOD controlled gate across the channel, while ramping down the LG beam with the BEC superimposed over one reservoir. This is then allowed to settle and thermalize for 2 s, and we end up with a final ensemble of atoms in the dumbbell potential with order  $10^5$  atoms at a temperature below 100 nK, with all of the atoms in one reservoir.

### 3.1.6 Imaging

After the dumbbell potential has been loaded with atoms in one reservoir, the gate beam is switched off, allowing the atom to flow in the circuit. To measure the state of the system at a time after release, we image the atoms using a partial transfer

absorption technique, which allows us to image a known fraction of the atoms with on-resonant imaging light. This technique is described in detail in appendix A. In order to reduce the effects of non-linearities that are a part of absorption imaging, we would ideally like to keep the optical density constant in our region of interest. While this is not possible with the entire dumbbell as a region of interest, if we split up the measurement into two parts and look at the reservoirs independently, we are able to come close to this goal. For our experimental measurement of the BEC state at some time after the gate is released, we will take two separate images. For one of these, we choose the imaged fraction of atoms such that the optical density in the initially full reservoir is as close to 1 as possible. For the other, we choose the imaged fraction of atoms such that the optical density in the initially empty reservoir is as close to 1 as possible. We then form a composite image of the BEC at this time by independently scaling these two images of either reservoir, based on the known fractions of atoms imaged, and combining them. For each time measured, we do this three or four times and average the result to get our final 2D density profile as our data point for that time, in order to reduce statistical noise. An example of one such density profile is shown in figure 3.7.

### 3.1.7 Trap Geometry

The description of the trap geometry is not quite as simple as the idealized case of a hard wall in all directions. First of all, the vertical confinement is created using a beam with a Gaussian intensity profile, and will thus create a harmonic

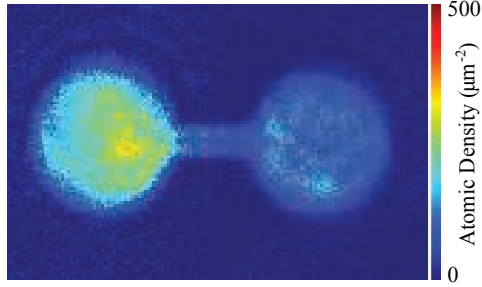


Figure 3.7: A sample plot of the atom density for the BEC trapped in our dumbbell potential. The total atom number in this image is  $495(16) \times 10^3$ .

trap in this direction. This sheet trap also contributes a weak harmonic trapping potential in the plane, on top of the dumbbell potential.

In addition to the sheet confinement, we have the dumbbell itself, which is imaged onto our BEC using an imaging system with a numerical aperture of approximately 0.2. In addition to the inherent limits due to diffraction, this imaging system also contributes to further degradation of the hard wall potential through imaging aberrations. Since all of this cannot be easily modeled analytically, we resort to an observational measurement of the system to determine what our actual potential is.

### 3.1.7.1 The Sheet

The sheet potential is created by focusing a Gaussian beam tightly in one direction. This produces a trap in the center that is tightly confined harmonically in the vertical direction, and loosely harmonically confined in the plane. With proper balancing of the sheet geometry, the confinement in the plane can be made to be

roughly azimuthally symmetric. The vertical trapping frequency will be important for our measurements, and thus needs to be measured. The process for this involved giving the atoms a small momentum kick in the vertical direction with a pulsed magnetic field gradient, allowing the atoms to oscillate in the harmonic trap for a varying amount of time, followed by releasing the trap, a significant time-of-flight (TOF), and imaging of the atoms in the horizontal direction. The vertical position of the cloud after the TOF will depend on the vertical velocity of the cloud when the trap was turned off. Since the atoms are oscillating in the vertical harmonic trap, this velocity will also oscillate at our vertical trapping frequency. Carrying out this measurement shows that the vertical trapping frequency  $\omega_z/2\pi = 529(2)$  Hz.

### 3.1.7.2 The Reservoirs

If we approximate the point spread function of our imaging system to be a Gaussian shape with  $1/e^2$  radius  $w$ , then the potential of a single reservoir in our dumbbell system will be given by

$$V = \frac{1}{2}m\omega_x^2x^2 + \frac{1}{2}m\omega_y^2y^2 + \frac{1}{2}m\omega_z^2z^2 + \frac{U_m}{2} \left[ 1 + \operatorname{erf} \left( \sqrt{2} \frac{r - r_0}{w} \right) \right], \quad (3.1)$$

where  $r = \sqrt{(x - x_c)^2 + (y - y_c)^2}$  is the radial coordinate relative to the center of the reservoir at coordinates  $(x_c, y_c)$ ,  $r_0$  is the radius of the reservoir, erf is the error function, and  $\omega_i$  is the sheet trapping frequency in the  $i$ th direction.

With a known number of atoms and this form of the potential, we can numerically calculate the density distribution that we should observe. By adjusting the parameters  $\omega_x$ ,  $\omega_y$ ,  $r_0$ , and  $w$ , we can find the best fit to what we observe in

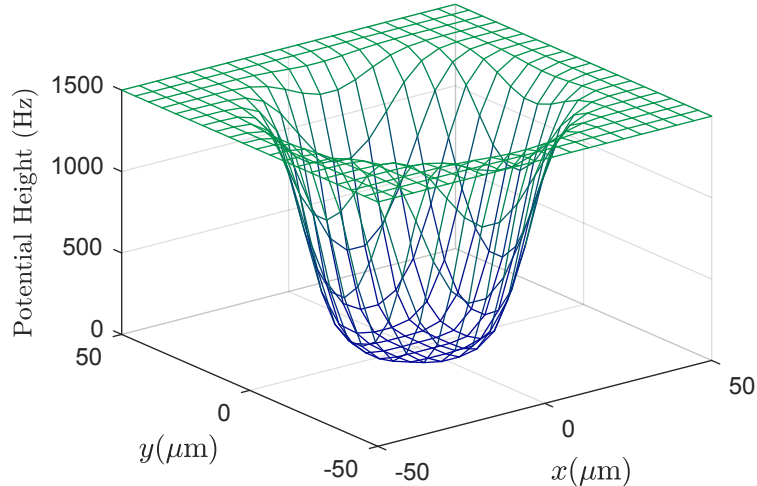


Figure 3.8: A plot of the model we use for the reservoir potential in the plane, given in equation 3.1. The parameters of this model are fit by comparing expected optical densities to what we see in experiment for *in-situ* images of atoms in a reservoir. For this plot,  $U_m = 1500$  Hz.

the experiment. Doing this provides us with the best fit values  $\omega_x/2\pi = 9.1(9)$  Hz,  $\omega_y/2\pi = 9.4(6)$  Hz,  $r_0 = 27(2)$   $\mu\text{m}$ , and  $w = 12(2)$   $\mu\text{m}$ . We did not independently measure the oscillation frequencies in the plant, although these values are all within expectations of our system except for the very large value of  $w$ , which should be closer to 3  $\mu\text{m}$  given the numerical aperture of our imaging system. This large value is likely due to aberrations which we will discuss more in the next section. This model potential form is plotted in figure 3.8 for a sheet depth of  $U_m = 1.5$  kHz.

### 3.1.7.3 The Channel

If our system were only subject to diffraction limits in its imaging, we would expect the potential in the channel region to be fairly close to hard walled, since

the width of the channel is approximately  $14 \mu\text{m}$  and the diffraction limit of our system is about  $3 \mu\text{m}$ . We observe, however, something very different from an empty channel. As can be seen in figure 3.7, there is a depletion of density along a ridge down the center of the channel. This is likely due to both spherical aberration and astigmatism in our imaging system, and this same phenomenon is what causes our surprisingly large value of  $w$  in the previous section. Bench measurements of this imaging system, carried out since this experiment was completed, have verified that such large aberrations are present.

Since we have no good analytical model of what the potential actually is through the channel, we are forced to approximate with a simple model using observed quantities such as the observed Thomas-Fermi width of the channel, the integrated 1D density  $n_{1\text{D}}$  of atoms in the channel, and the cross sectional profile of the channel. The closest description we can find using these parameters is to model our channel potential by  $V \propto y^4$ , with the bottom of the potential having an offset given by  $bU_m + V_0$ , where  $b = 0.15(2)$  and  $V_0/h = 223(30)$  Hz. The  $bU_m$  term is proportional to the dumbbell potential height, and is due to the imaging aberrations causing light to fall in the center of the channel. The  $V_0$  term is an overall offset in the channel, likely due to a local maximum in the sheet potential where the channel is located .

In order for this model to accurately describe our system, we also must take into account the 2D-3D crossover. For  $\mu - V(y = 0) < \hbar\omega_z$ , we use only the ground state of the harmonic oscillator in the  $z$  direction, and for  $\mu - V(y = 0) > \hbar\omega_z$ , we use the full Thomas-Fermi solution in the  $z$  direction. For the example reservoir

potential shown in figure 3.8, the offset at the center of the channel is equal to 450(75) Hz, which is a significant portion of the overall potential height.

## 3.2 Thermal Cold Atom Apparatus

The system used to verify the thermal resistance prediction is a  $^{87}\text{Rb}$  thermal gas trapped in an ODT. This gas is created by loading a MOT from background gas created using SAES rubidium getters, and using a variation of the temporal, dark-spot MOT setup prior to releasing the atoms into one reservoir of the dumbbell potential. This potential is created using a slightly blue detuned laser with the Generalized Phase-Contrast (GPC) setup described below.

### 3.2.1 Vacuum System

The vacuum system for the thermal Rb experiment is centered around a Kimball Physics model MCF600-SphOct-F2C8 spherical octagon chamber. This chamber has concentric, spherical inner and outer surfaces. Either side is cut to have a 6" diameter Multi-CF (ConFlat compatible) flange with a 4.3" diameter bore. In eight equally spaced places around the periphery of the 6" flange, the outer sphere is cut down to produce a 2.75" diameter Multi-CF flange, and bored through to the center with a diameter of 1.5". This platform provides flexibility in design of the system, and good optical access around the entirety of the center of the vacuum. For our experiment, a 40 L / s ion pump (Varian VacIon Plus 40) was attached to one of the small 2.75" flanges to keep the system under  $10^{-8}$  Torr while the experiment

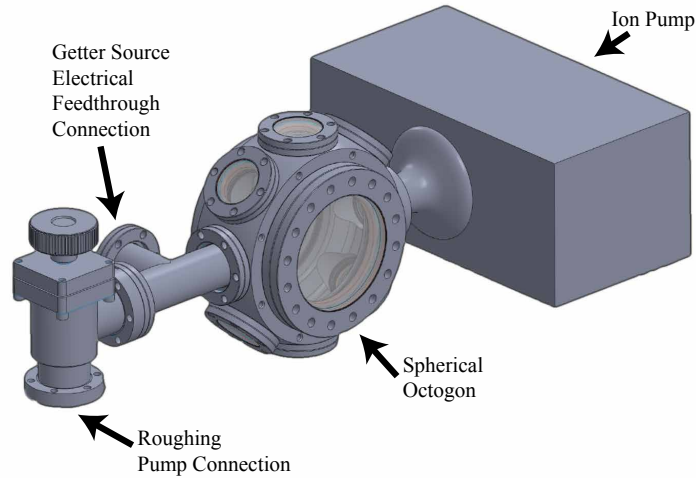


Figure 3.9: Complete vacuum system used for the thermal Rb system without magnetic coils or optical mounting elements. The main chamber is a Kimball Physics spherical octogon with two large, non-AR coated windows mounted on 6" CF Flanges. One of the small ports of the chamber is connected to the ion pump keeping the system under vacuum. Opposite the ion pump is a 2.75" CF mounted tee, connecting the chamber to both the electrical feedthrough to power the rubidium getter source, as well as the valve used to connect to the rough pump system.

is running. This results in a vacuum limited trap lifetime significantly longer than lifetimes we expect to see due to photon scattering. Opposite the pump, a standard 2.75" ConFlat tee is used to provide both a port for initial pump-down, and an electrical feedthrough to power the Rb source. The remaining six 2.75" flanges had optical viewports attached, which were anti-reflective (AR) coated for 532 nm and 780 nm. The two 6" flanges had uncoated optical viewports attached. The chamber was mounted with the 6" flanges in the vertical plane. This whole setup is shown in figure 3.9.

The only hardware inside of the chamber was the SAES Rb Alkali Metal Dispensers (getters). There were three of these sources mounted within the 2.75"

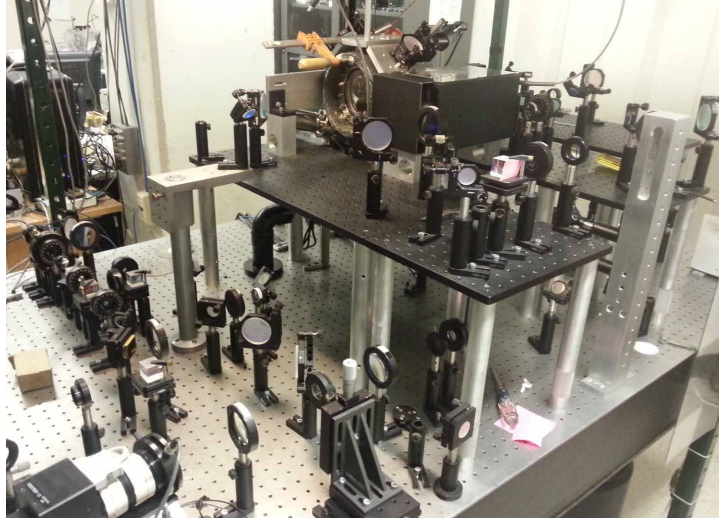


Figure 3.10: The vacuum chamber used in the experiment. Also shown are the various optics used to split up and align the MOT trapping beams. Part of the GPC setup can be seen at the bottom of the image as well.

flange bore opposite the ion pump using the groove-grabber system provided with the Kimball Physics chamber. Magnet wire connected the terminals of the getters to the electrical feedthrough. During normal operation, a current of approximately 3.6 A was run through one of these sources. When heated by this current, the compound within the source emits atomic Rb, increasing the pressure in the chamber to the running value of about  $5 \times 10^{-9}$  Torr.

The initial pump-down of the chamber was carried out with a turbo-molecular pump through a UHV compatible metal valve (MDC P/N: 314002). While rough pumping with the turbo-pump, the chamber was wrapped in heater tape and aluminum foil, and baked to approximately  $150^\circ\text{C}$  for about 1 week. After the temperature was ramped back down to ambient, the valve was closed, and pump turned

off and removed. This produced a base pressure of approximately  $10^{-10}$  Torr.

### 3.2.2 Laser System

The main laser system of the thermal Rb system, shown in figures 3.11 and 3.12, is based around Toptica DL-100 laser operating at 780 nm. A small portion of this master oscillator is sent through a single-passed AOM (all AOMs used in the thermal Rb experiment are IntraAction model 1205C-804B) centered near 80 MHz, into a SA spectroscopy setup used for frequency locking the laser. This provides us our main control over the final frequency used in the experiment. The remaining part of the master oscillator is sent through a double-passed AOM, the frequency of which we can sweep from 55 MHz to 105 MHz. The output of the double-passed AOM is used as the seed for an injection locked diode, providing us with about 100 mW of output light at the desired frequency. The double-passed AOM allows us to tune the final frequency of the system over a range of about 100 MHz. This allows us to easily sweep the frequency for our polarization gradient cooling step discussed later. The frequency of the injection locked laser is monitored using a Fabry-Pérot interferometer. This allows us to ensure that the laser is properly injection locked, as this is very sensitive to both temperature and laser diode current.

We increase our power further with a tapered amplifier, giving us about 500 mW at the same frequency. This amplifier was made from a re-purposed tapered laser (Tiger Littrow Series). This is then sent through another single-passed AOM, being used as a switch before the polarization-maintaining fiber that trans-

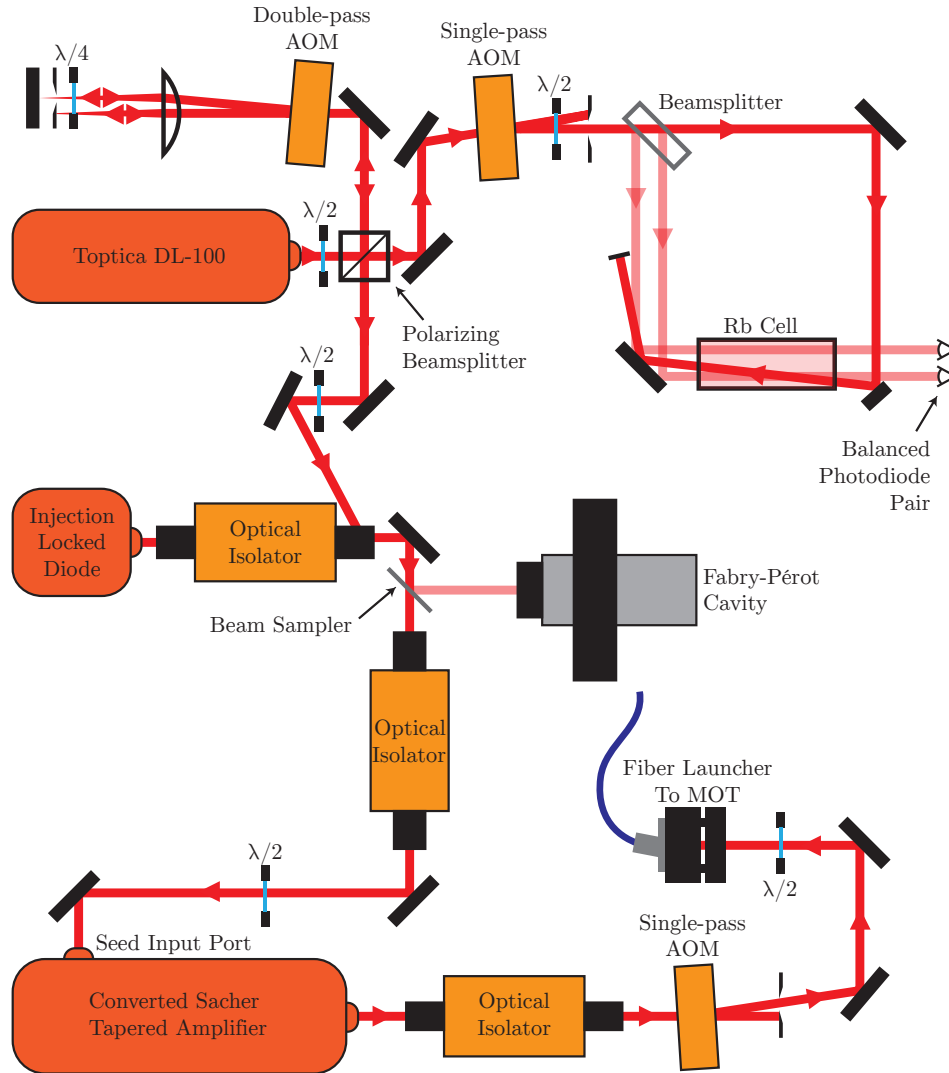


Figure 3.11: The setup of the main laser system for the thermal rubidium experiment. The main oscillator is a Toptica DL-100 diode laser. This is locked to the the necessary frequency using a standard saturated absorption setup with a rubidium reference cell. This beam is passed through a double-pass AOM, set up in a cat's-eye configuration. This allows us to adjust the frequency of the beam with minimal change in optical alignment. To compensate for any optical misalignment that does get into this set up, a second diode laser is injection locked to the frequency of this beam, and is subsequently amplified to necessary power levels with a tapered amplifier, and launched into a single mode, polarization-maintaining optical fiber leading to the experiment table. Frequencies are adjusted with various AOMs throughout the setup, and the injection lock is monitored by a Fabrey-Pérot interferometer.

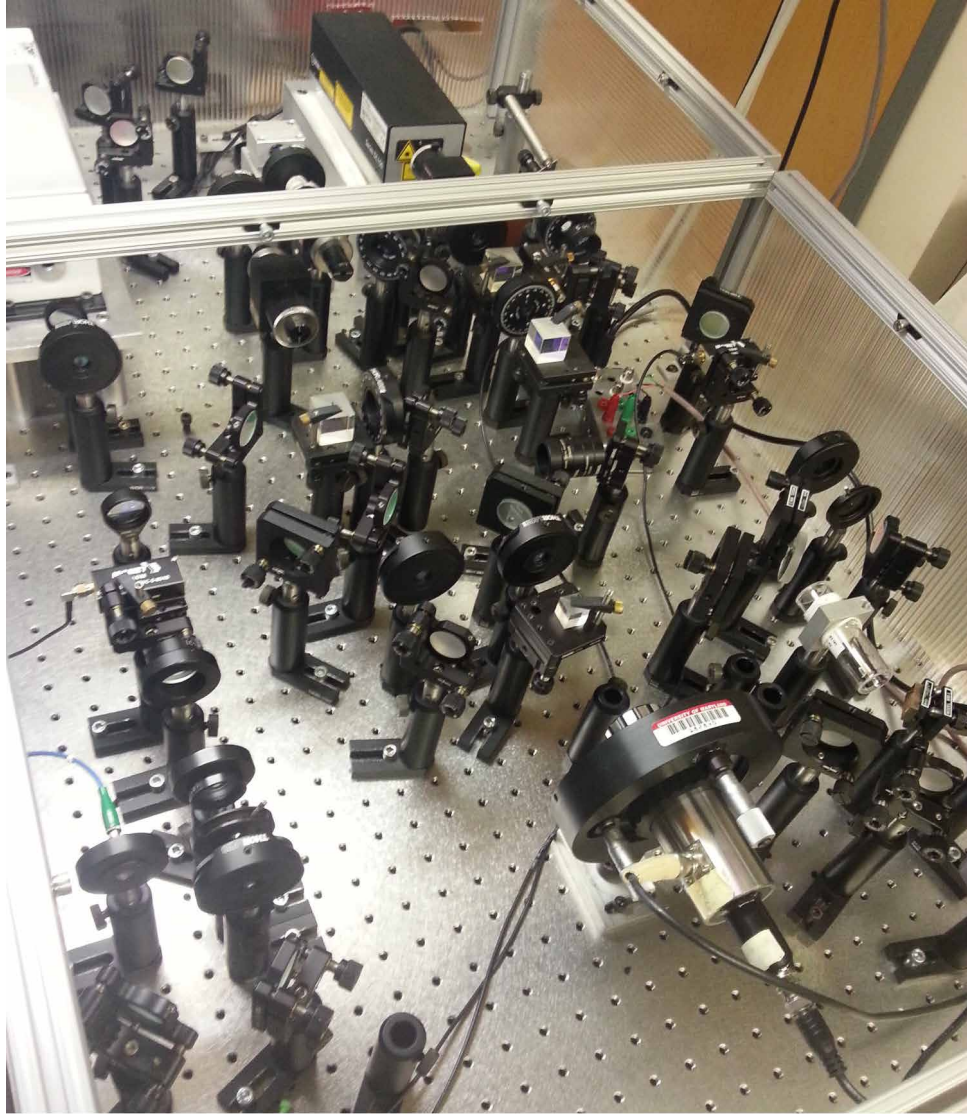


Figure 3.12: The actual laser setup used in the experiment to create the MOT trapping beams.

ports the light to the experiment table. After the AOM and fiber, the output is approximately 180 mW. This light is split into four beams of approximately equal power, which are then increased in diameter to approximately 1". Two of these are passed horizontally, counter-propagating through the large windows of the vacuum chamber to act as the MOT beams along the axis of the anti-Helmholtz coils. The other two beams are each sent up through the smaller viewports at  $45^\circ$  to the vertical, and are then retro-reflected. This produces the other four beams necessary to create the MOT. Each beam is appropriately circularly polarized prior to passing through the chamber using quarter-wave plates.

The repump light necessary for the MOT to function is produced by a second master oscillator (New Focus Vortex Laser), locked to a separate SA setup. This laser is placed on the experiment table, and is free-space coupled into the region of the MOT after passing through a single-passed AOM for switching and frequency control.

Additional light is also needed to create the ODT used in the experiment. This light is created with another Vortex laser, and is locked on the broad Doppler-broadened repump transition by passing a weak probe beam directly through a Rb cell, and observing the broadened absorption signal. The remaining light is then amplified with another injection locked diode, similarly monitored with a Fabry-Pérot interferometer, and fiber coupled into a 1 W New Focus tapered amplifier. This setup is shown in figure 3.13. This light is subsequently switched with a shutter before being used for the ODT. The poor mode quality of the tapered amplifier also requires us to clean up the beam with a pinhole spatial filter.

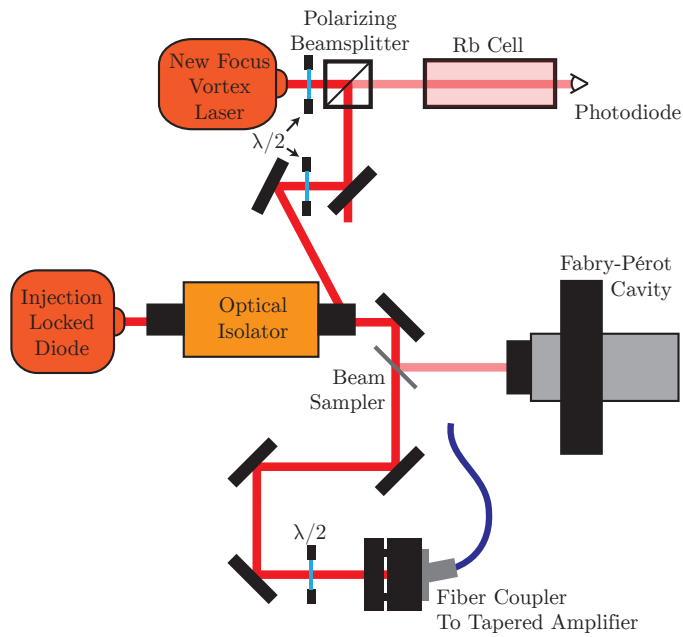


Figure 3.13: The beam used for the ODP in the thermal rubidium experiment is created using a tapered amplifier. The main oscillator for this system is a New Focus Vortex Laser, locked to the side of the Doppler broadened absorption signal of a probe beam passing through a rubidium reference cell. This is then amplified to the minimum requirements of the tapered amplifier using another injection locked setup. This beam is launched into a single mode, polarization-maintaining optical fiber, which connects directly to the amplifier.

### 3.2.3 Computer Control

The timing and data acquisition of the thermal Rb experiment is mainly controlled using a National Instruments model PCI-6713 analog output card. The eight outputs of the card are buffered and passed to control the amplitude and frequency controls on the appropriate AOMs, the IGBT switch on the MOT magnetic field coils, and the camera trigger. The necessary waveform for each channel is calculated based on the experimental run being done, and all of the waveforms are written to the card. The camera is set up to wait for the trigger signal, then upload images to the camera monitor program also running on the control computer. These images are then saved for later analysis. The relatively short run length and long minimum time step requirements of this experiment are such that this direct waveform writing method is more than sufficient in terms of memory limits.

### 3.2.4 Cooling Sequence

The full cooling sequence used in the rubidium MOT setup follows fairly standard procedure for such an experiment. First, the trapping and repump MOT lasers are turned on with the MOT magnetic field also on. We then use a variation of the commonly used polarization gradient cooling technique to further cool the atoms. In this technique, the magnetic field is generally turned off, and the MOT trapping lasers are detuned many linewidths from the trapping transition. This produces a sample of atoms significantly below the Doppler limit. Due to the unbalanced MOT beam powers in our system, a side effect of using retroreflection to save on needed

laser power, we are unable to turn the magnetic field of our MOT off during this step. As a consequence, the polarization gradient cooling will only occur near the zero of magnetic field in the center of the trap, limiting our final temperature to a few times what is possible in a properly balanced setup. With this method, we obtain a sample of atoms at a temperature of  $40 \mu\text{K}$  prior to loading into the dipole trap.

The atoms are loaded into the ODP by simultaneously switching off the MOT cooling lasers and magnetic field while switching on the ODP laser with the atom cloud superimposed over one reservoir of the dumbbell. Since the height of our dipole trap is on the order of the MOT temperature, we lose a significant portion of atoms when we load into the ODP. Since these are the highest energy atoms in the ensemble, this provides an additional level of cooling. As shown below, after loading into the ODP we end up with an ensemble of atoms with an effective temperature of  $25 \mu\text{K}$ .

### 3.2.5 Imaging

To image the thermal rubidium atoms during the experiment, a fluorescence imaging technique is used to capture the spatial distribution of atoms in the trap at various times after releasing the MOT. For this technique, the main MOT trapping light is pulsed on for  $100 \mu\text{s}$ , and a portion of the spontaneously emitted light from the cloud is imaged directly onto a CCD. This imaging is accomplished with a single, 1" diameter, biconvex spherical lens with focal length  $f = 125 \text{ mm}$  placed

250 mm directly above the MOT location. The CCD is placed at the focal plane of this imaging system, 250 mm above the lens. The small numerical aperture of approximately 0.05 suggests that the diffraction limited resolution in our system would be 8  $\mu\text{m}$ , however the system is further limited by spherical aberrations due to the use of the spherical lens for imaging. Observations in the system suggest that our actual optical resolution is on the order of 100  $\mu\text{m}$ . Our pulse length was chosen to keep the thermal movement of our atoms to under this amount during the pulse duration.

### 3.2.6 Thermal System Temperature

Since the atoms in any trap will always have a finite temperature, the velocity distribution of atoms will always have a finite width. Because of this, the atoms will spread out when they are released from the trap. If this spread can be measured, the temperature of the atoms can be calculated. Fortunately, the imaging methods mentioned above can easily accomplish this. If the time between turning off the trap and imaging the atoms is varied, quantitative information about the spread can be gathered. In order to make use of this information, however, we must know how the sample should spread at a given temperature.

For a thermal sample of atoms in a harmonic trapping potential, the spatial distribution of the atoms will have a Gaussian shape [34],

$$N(x, y, z; t = 0) = N_0 e^{-\left(\frac{x^2}{2\sigma_{x0}^2} + \frac{y^2}{2\sigma_{y0}^2} + \frac{z^2}{2\sigma_{z0}^2}\right)}.$$

To determine the density of the sample at a point  $(x', y', z'; t)$  some time later, we

need to integrate over our initial distribution, multiplied by the probability that an atom will have the necessary velocity,  $(v_x, v_y, v_z) = \left(\frac{x'-x}{t}, \frac{y'-y}{t}, \frac{z'-z}{t}\right)$ , to get from the initial point to the final point. The probability of having a velocity  $(v_x, v_y, v_z)$  is obtained from the Maxwell-Boltzmann distribution,

$$f(v_x, v_y, v_z) = Ae^{-\frac{m(v_x^2+v_y^2+v_z^2)}{2kT}}.$$

Thus our final density distribution is described by,

$$\begin{aligned} N(x', y', z'; t) &= \int \left\{ N_0 e^{-\left(\frac{x^2}{2\sigma_{x0}^2} + \frac{y^2}{2\sigma_{y0}^2} + \frac{z^2}{2\sigma_{z0}^2}\right)} Ae^{-\frac{m\left(\left(\frac{x'-x}{t}\right)^2 + \left(\frac{y'-y}{t}\right)^2 + \left(\frac{z'-z}{t}\right)^2\right)}{2kT}} \right\} dx dy dz \\ &= N'_0 e^{-\left(\frac{x^2}{2(\sigma_x(t))^2} + \frac{y^2}{2(\sigma_y(t))^2} + \frac{z^2}{2(\sigma_z(t))^2}\right)}, \end{aligned}$$

where  $(\sigma_i(t))^2 = \sigma_{i0}^2 + \frac{kT}{m}t^2$ . The final distribution is still a Gaussian, but with a variance that increases quadratically in time at a rate that depends on the temperature. Using this information, we can fit our measured distributions to Gaussian functions, and fit the measured variances as a function of time to obtain the temperature of the atoms. An example of this expansion for our MOT system, which produces atoms with a temperature of approximately 40  $\mu\text{K}$ , is shown in figure 3.14.

### 3.2.6.1 Truncated Thermal Distribution

In our experiment, we are loading the atoms from a thermal cloud into a trap of finite height. Because of this, the initial thermal distribution is going to be truncated as shown in figure 3.15. Due to the rough nature of the walls of our trap, and the presence of the channel, we expect that the system will be chaotic enough that there are no closed orbits in the reservoirs allowing trapping of atoms above

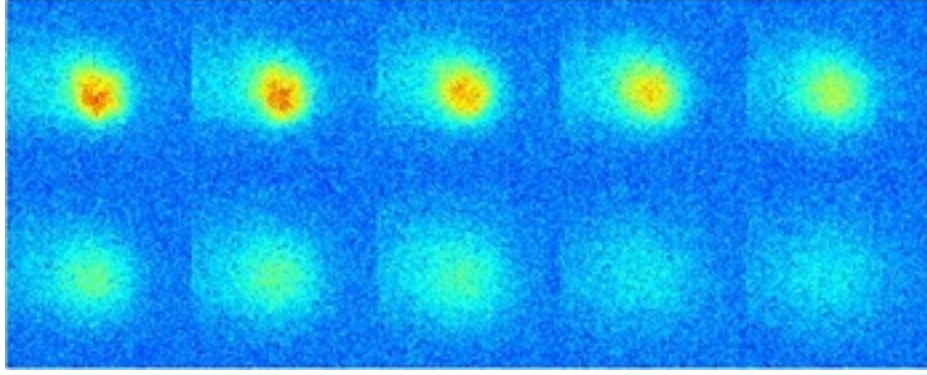


Figure 3.14: False color fluorescence images of the thermal expansion of a sample of cooled Rubidium atoms at  $40 \mu\text{K}$ . The time between frames is 1 ms. By fitting the optical density of the cloud after various TOF, we are able to determine the temperature of the atoms, which affects the rate of expansion of the cloud.

this energy. Additionally, the mean time between collisions in our thermal system is long compared to the lifetime of the trap, so rethermalization will not occur. We thus need some method to approximate our system temperature.

The 2D thermal distribution for our MOT, prior to being loaded into the dumbbell potential, is given by equation 2.21. For our atomic mass ( $m = 87 \text{ amu}$ ), and temperature  $T = 40 \mu\text{K}$ , this gives us

$$f_{2\text{D}}(v) = \frac{m}{kT} v e^{-\frac{mv^2}{2kT}} dv, \quad (3.2)$$

after integrating over the  $\theta$  coordinate. The trapping potential has a height of approximately  $U = k \times 60 \mu\text{K}$ . Any atom with a kinetic energy higher than this will escape the trap. This corresponds to a velocity given by

$$v = \sqrt{\frac{2k(60 \mu\text{K})}{m}} \approx 10.7 \text{ cm/s}. \quad (3.3)$$

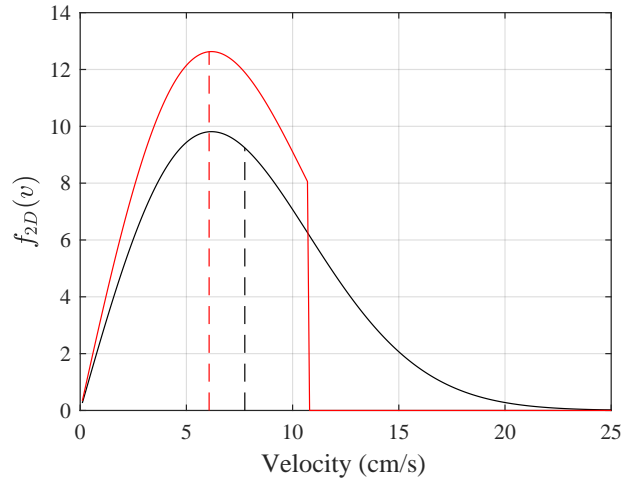


Figure 3.15: The black curve depicts the 2D velocity distribution of our atomic cloud at  $40 \mu\text{K}$ , prior to loading into the ODT. The dotted black line shows the average 2D velocity  $\langle p_{2D} \rangle / m$ . When the atoms are transferred into the ODT, the atoms with a velocity greater than some cutoff ( $1/2mv^2 > U_m$ ) are lost from the trap. After normalizing the velocity distribution, we are left with the red curve, along with its associated average 2D velocity. This velocity corresponds is equal to that of a thermal system with a temperature of  $25 \mu\text{K}$ , which is what we use as our experimental temperature when comparing to theory.

The truncated 2D speed distribution, along with the initial MOT 2D speed distribution, are shown in figure 3.15. The truncated distribution has been normalized, due to the atoms being lost. The dotted lines in the figures show the average 2D speed for the two distributions, which is the quantity from the distribution that matters for our derivation of dissipation for the thermal system. The average 2D speed for the truncated distribution corresponds to the average 2D speed in a Maxwell-Boltzmann distribution with a temperature of  $\approx 25 \mu\text{K}$ . This is the value that we will use when comparing our experimental values to our derived values. We do not compare other quantities, such as the rms speed, since the average speed is what shows up in our equations for dissipation.

### 3.3 Creating a Dumbbell Potential

#### 3.3.1 Generalized Phase-Contrast Imaging

To perform the desired experiments with both the thermal and BEC systems, we need to be able to create dumbbell shaped, 2D ODPs. The method we chose for this in the thermal system was to use an adaptation of the Generalized Phase-Contrast (GPC) setup [36–38]. This system allows us to take an initial phase pattern imprinted on a Gaussian mode beam, and convert it directly into an output intensity pattern. It is an efficient method for spatially shaping the transverse intensity profile of a focused laser beam. The GPC technique redirects most of the beam intensity into the desired potential pattern, making efficient use of available laser power. As a derivative of the Zernike phase imaging [39], it relies on a strate-

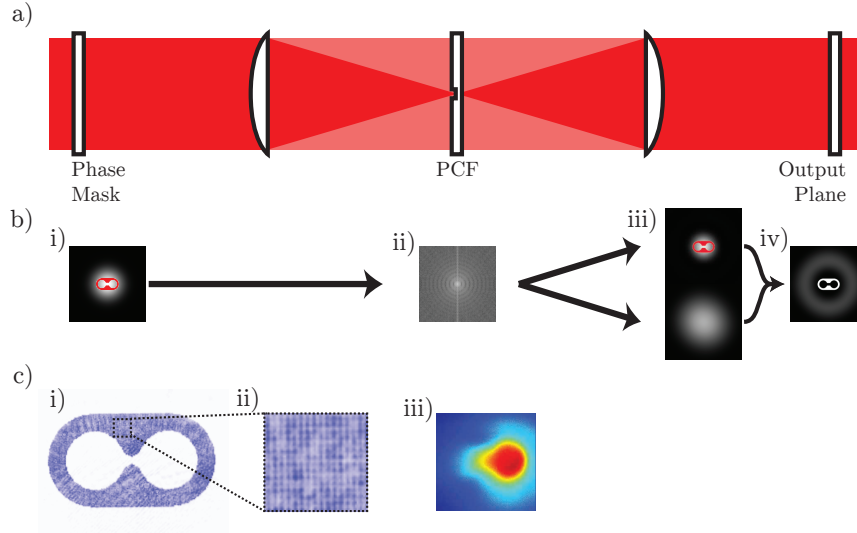


Figure 3.16: a) Schematic of the GPC optical setup, consisting of an input phase mask, two lenses in a 4-f configuration, and a PCF. b) A representation of the dipole trap beam field as it passes through the setup taken from simulations, including i) the input beam with desired phase mask (red area represents the  $\pi$  phase shift imprinted onto the input Gaussian beam), ii) a representation of the intensity in the Fourier plane, iii) the two portions of the beam at the output plane that either did (lower) or did not (upper) pass through the PCF (red area represents the still  $\pi$  phase shifted portion of the beam), and iv) the output intensity pattern resulting from the interference of the portions in iii). c) i) A typical CCD camera image at the output plane of the GPC optical setup for the example pattern from b), ii) a close-up image of this pattern, showing the dead-space artifacts from the SLM, and iii) a fluorescence image of thermal  $^{85}\text{Rb}$  atoms with an effective temperature of  $25 \mu\text{K}$ , taken 2 ms after release from the potential displayed in i). Note, the atoms were released and imaged while initially contained on only one side of the dumbbell shaped potential.

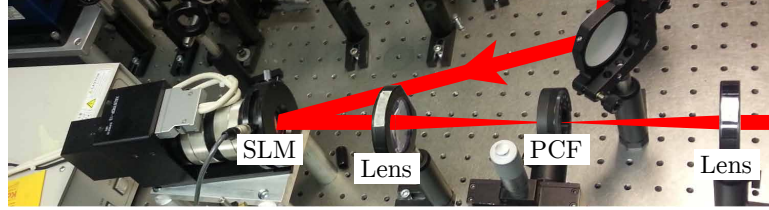


Figure 3.17: The actual GPC setup used in the experiment. The beam path is artificially drawn in for clarity.

gically sized and placed phase-contrast filter (PCF) to enable a one-to-one mapping of a phase embedded across a laser beam to a high-contrast spatial intensity profile. While we only show this for a binary phase pattern, the theory described by Gluckstad et al. [36] extends fully to continuous phase patterns. At the same time, this makes phase-contrast shaping closely related to phase-contrast imaging that has been used to monitor atomic cloud densities in a minimally destructive way [40]. We demonstrate the approach with the setup shown in figure 3.16, which is easily integrated into standard imaging systems used to study cold atoms. While we employed a 4-f arrangement to create the intensity pattern in our use of the technique, other arrangements are also possible. The GPC approach requires the phase mask to be placed in a collimated beam before the first lens and the PCF to be located in the Fourier plane of the first lens. The desired intensity pattern appears in the image plane of the second as shown in Figure 3.16.

In our setup, we use a computer controlled spatial light modulator (SLM) as the phase mask. Etched phase masks could also be used for this purpose. While they will have better resolution, they lack the flexibility that SLMs offer for real time changes to the masks. The PCF is a simple phase mask consisting of a circular

region that shifts the phase of low spatial frequencies by  $\pi$ . The diameter of the circle depends on the input beam size and the details of the phase mask. The initial PCF diameter is chosen to match the focal spot size of the beam in the Fourier plane, with the phase mask removed. Typically the diameter has to be adjusted for maximum contrast as discussed below.

The PCF splits the beam into two parts. One part contains the lowest-order spatial frequencies that have been shifted in phase by  $\pi$ . The profile of this beam will be close to Gaussian because it is nearly devoid of any higher order spatial frequencies. The phase of the other part is unshifted. This portion contains the initial Gaussian envelope, in addition to all of the high spatial frequency components of the associated phase pattern. The two parts will interfere in the image plane to produce the desired intensity profile. The sequence of events is depicted in Figure 3.16. For optimum efficiency and contrast, the intensities of the two parts of the beam should be equal, placing restrictions on the size of the PCF and the particular phase pattern used as mentioned above. Due to mismatch in the sizes of the two parts, there is typically a ring of light surrounding the desired pattern. In our experiments we block this light with an iris. It is useful to simulate desired patterns using numerical approximations prior to setting up the apparatus as well.

In practice, due to having a limited number of PCFs available, and the effort required to change the beam size, we typically fix the PCF and beam sizes, and vary the size of the phase pattern to maximize the contrast in the output plane. For this experiment, the  $1/e^2$  radius of the initial beam was 10 mm, and the focal length of the lenses were 60 mm. The SLM (Hamamatsu PAL-SLM) used to produce the

initial phase pattern was a 768-by-768 array, covering an area of 2.5-by-2.5 mm. The PCF was created in collaboration with the Laboratory for Physical Sciences, and consists of a fused silica window with an array of nine phase spots on a 5 mm grid, varying from 5.5 to 6.5  $\mu\text{m}$ . The phase spots were chemically etched to a depth of  $d = 850$  nm. The difference in index of refraction between the air ( $\approx 1$ ) and fused silica ( $\approx 1.45$ ) produces a phase shift of  $\Delta\phi = 2d(n - 1)\pi/\lambda \approx \pi$  for light with a wavelength of 780 nm.

There are two main advantage of phase shaping over the simple amplitude shaping used for the BEC experiment. First, the theoretical efficiency of the former, defined as the fraction of total input power contained in the desired output pattern, can be larger be more than a factor of 2, depending on the exact pattern used. Experimentally, however, this is not always the case. For this experiment, the phase spot used was extremely small ( $\approx 6 \mu\text{m}$ ), and the spherical lenses used did not allow diffraction limited performance down to this size. Ideally the imaging system should be diffraction limited, with the size of the phase mask larger than the imaging aberrations. More specialized aspherical lenses or complex lens systems could be used in future generations of the setup to make this possible and minimize this source of loss.

The second, and more important, advantage is the flexibility this method provides when combined with an SLM. For this experiment, the SLM was computer controlled, and is interfaced to the computer as an external monitor. With this setup, changing the pattern is just a matter of changing what is on that monitor. While simulations are accurate enough to provide a good starting point for pattern

designs, the pattern on the SLM can be fine tuned to increase efficiency once the optical setup is complete. In addition to fine tuning individual pattern parameters, patterns can be completely changed in a matter of seconds as well, providing quick adjustment to experimental parameters for certain experiments. In addition, it may also be possible to change the phase mask on a time scale commensurate with degenerate gas dynamics.

The main limitation of the GPC technique, when implemented with an SLM, is the cost of SLM. SLMs are also generally designed for limited ranges of wavelengths, limiting the flexibility of the system. In addition, the technical details of how the SLM works, namely the necessary input polarization and the inter-pixel dead-space, can affect the resulting potential that the SLM produces. In order for the SLM to change only the phase of the light incident upon it, the light must be linearly polarized in a particular direction. For reflective SLMs, which are preferable due to reduced dead-space as discussed below, this means that one of two things can be done to separate the input light from the output. Either the light incident on the SLM must be at a slight angle, or a 50/50 beamsplitter can be used if the light must come in normally. The first option can be problematic if the depth of field of the imaging system in the GPC setup is smaller than the longitudinal displacement of the tilted SLM plane. If the second option is used to eliminate this problem, the total power is cut down to 25% of the input. Combined with the relatively low damage threshold for SLMs, this can be a problem for far-detuned traps. A similar photolithographic process as for the amplitude mask (AM) described below could be used to etch a phase mask. While this would negate all of the problems

mentioned above, it would also result in a static mask without the versatility of the SLM created masks.

Before ending this section, we return to the dead-space mentioned above. In any pixelated structure, like an SLM, there will necessarily be some space between pixels that cannot be used. In transmissive SLMs, this space contains the wires that address each pixel, and blocks the light. While reflective SLMs can improve significantly on this, there is still some unusable space between pixels. The reflective SLM used in this experiment has a  $>90\%$  fill factor, so this dead-space is quite small, but is still enough to cause a noticeable effect in the output. In our phase shaping scheme, this shows up as a slight intensity drop in the space between pixels as can be seen in Figure 3.16 (c-ii). Using a blue detuned trap minimizes the problems this can cause, since the atoms are trapped in areas with no light. Additionally, some newer, reflective coated, liquid crystal on silicon (LCoS) SLMs claim to have near 100% fill-factors, however we have not tested these devices to date. Like traditional SLMs, the LCoS SLMs can be used for both phase and amplitude shaping.

### 3.3.2 Direct Intensity Masking

For the BEC experiment, we used a direct intensity masking setup to create the necessary potential. This method is considerably more lossy than the theoretical limit of phase-contrast imaging, as it involves an opaque amplitude mask (AM) to block part of the beam. The setup, however, is simpler than the phase-shaping setup and the total cost is considerably lower. All that is required is an amplitude mask

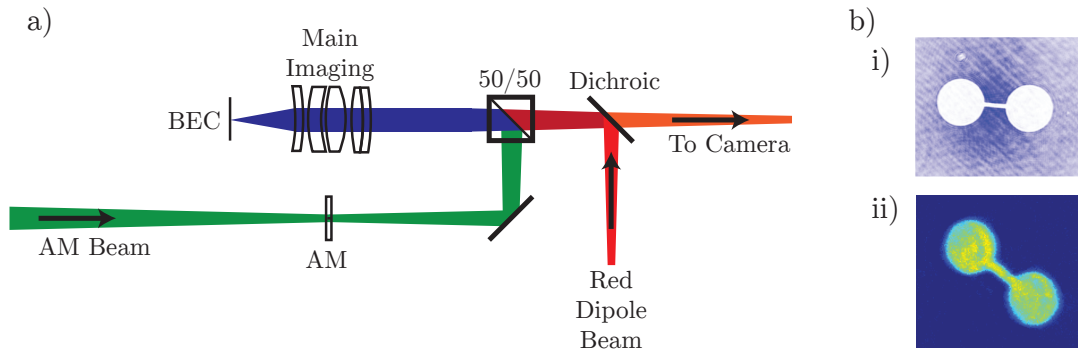


Figure 3.18: a) Schematic of the imaging setup used for the AM system. This setup combines the AM dipole trap beam (green) with a red-detuned (1064 nm) dipole trap beam (red) and counter-propagating imaging beam (589 nm) (orange) using a 50/50 beamsplitter. These two beams are separated using a dichroic plate beamsplitter. All three of these beams are imaged through a main imaging stack suspended on a 2D translation stage above the BEC. The mask is placed on a 3-axis translation stage to allow precise positioning. b) i) A typical CCD camera image of the output plane of a AM optical setup. This example is from a simple, 1:1 system using a single spherical lens. ii) An in situ absorption image of a sodium BEC trapped in this potential.

and a series of lenses to relay the shadow of the mask onto the atoms as sketched in figure 3.18. For the blue-detuned light used in this experiment, the mask blocked light associated with the trapping regions while transmitting the light responsible for the dipole potential. As with phase shaping, amplitude shaping is also easily integrated into commonly used imaging systems for cold atoms. In our experiment, we combined the imaging for the amplitude shaping with that used for absorption imaging diagnostics.

### 3.3.2.1 Construction of Intensity Masks

For our experiments designed to use the AM, 2D potential landscapes had to be created that extended over a length of up to approximately  $150\ \mu\text{m}$ , with minimum structure sizes down to approximately  $10\ \mu\text{m}$ . The imaging system that was used for absorption imaging of the atoms as well as to image the two dipole traps, provided a reduction of 2.9 between the image plane at the atoms and the object plane on the optical table. The dimensions of the necessary masks are thus approximately  $450\ \mu\text{m}$  with features around  $30\ \mu\text{m}$ . While this is incredibly difficult to achieve with ordinary machining techniques, it is well within the realm of possibility of even very basic photolithographic techniques used to fabricate microelectronic circuits. With the wide availability of fabrication labs at many universities, as well as private facilities, the necessary masks can be created quickly with minimal training. Special care needs to be taken, however, beyond standard procedure in these labs, as optical quality is generally not a concern in microelectronic applications.

The process that we use starts with a commercially produced contact mask, which we transfer into a chromium mask on an AR coated optical window. These are cheaply produced from design files sent to a manufacturer. These commercial masks generally come in one of two forms; a glass plate with an opaque chromium mask, or a plastic sheet with an opaque resin mask. Neither of these types of mask is directly usable in our experiment for a few reasons. The mylar masks, in addition to likely melting with high optical intensities, are not completely opaque, and will allow some tapping light to pass, which is undesirable. The glass masks, while being opaque enough for our application, are not AR coated and internal reflections will produce etaloning effects in the output plane at the BEC.

For this experiment, we needed the mask to be on a 1/2" window with a broadband AR coating (350–700 nm). To transfer our commercial masks onto our this window, the we first coated the window on one side with a  $\sim 200$  nm thick layer of chromium using thermal vapor deposition. This thickness which is sufficient to produce an experimentally verifiable optical density greater than 7 for the wavelength of light used (532 nm). The thickness was constantly monitored during deposition with a calibrated quartz oscillator that was also exposed to the chromium. A special rig to hold the windows in the vacuum chamber was necessary to avoid scratching the back side of the window, and standard optical cleaning procedures were carried out before deposition. A layer of gold can also be deposited with the same system, although it will not stick well to the window itself, and a thin layer of chromium is first necessary.

The chromium coated windows were then coated with a layer of photoresist

(Shipley 1813), which is spun on using standard methods for silicon wafers. Again, proper tools must be constructed and used to ensure the back side of the window is not scratched during photoresist spinning, or the subsequent baking to cure the photoresist. Since standard procedures in the lab are designed for thin (0.5 mm) silicon wafers, the baking time was adjusted to accommodate the relatively thick (3 mm) window. For initial tests, the time was approximately doubled to two minutes. The roughness of the edges of the final masks produced was on the scale of 5  $\mu\text{m}$ . It is expected that this is due to improper baking since uneven adhesion of the photoresist layer can cause these effects. Given the image magnification and diffraction limit of the experimental setup used, however, this was more than sufficient for our purposes. It is expected that further fine-tuning of the baking time, which would improve photoresist adhesion, would result in smoother masks if necessary for future experiments.

Once the photoresist is exposed to ultraviolet (UV) light, the polymer breaks down, and can be removed by a weak developer solution that leaves unexposed photoresist intact. In order to carry this process out selectively, and create our desired pattern, a commercially produced mask is used with the same dimensions as our final product. These can come in many forms, but those used in this experiment are created on a Mylar film with an opaque resin. These are easily produced from source files in a standard Gerber format. This mask is sufficient for exposing the photoresist, but lacks the AR coating desired, and optical density necessary for the experimental intensity mask.

This commercial mask is placed over the chromium and photoresist coated

window in an apparatus known as a mask aligner. This machine combines a vacuum system to hold the window and mask in place, a precision translation and rotation stage to align the two, a microscope to inspect alignment, and a timed UV exposure system. Again, another custom holder needs to be made to hold the window without scratching the back side, and to hold the window lower than the typically thinner silicon wafers used. Once exposed, the mask is removed and the window is again baked, with adjusted baking time, to finish curing the photoresist. It is then rinsed in the developer solution for approximately 40 seconds to remove the exposed photoresist. The result can then be examined under a microscope to verify that the desired pattern has been transferred properly. If not, the remaining photoresist can be stripped with acetone, and the photoresist, exposure, developing procedure can be attempted again. In our initial runs of this process, we had success rates of about one in every three tries. Once the proper transfer has been verified, the window is rinsed in a chromium etchant solution for approximately 2 minutes, or until the chromium in the exposed regions has been completely etched off of the window. The chromium etchant used in this experiment had no noticeable effect on the AR coating of the window. Any remaining photoresist can then be removed, and the finished chromium intensity mask is left on the optical window, and can be placed in the experimental setup at the object plane of the imaging system.

## Chapter 4: Experimental Details and Results

### 4.1 Thermal System

In order to test our theoretical treatment of the purely thermal system, we carried out an experiment using the thermal rubidium MOT system. For this experiment, a MOT was created directly over one reservoir of the dumbbell potential. A blue detuned, sheet ODP confined the atoms from below, with gravity providing confinement from above. The potential height of this sheet was approximately  $k_B(500 \mu\text{K})$ , well above the temperature of the MOT. The MOT was then suddenly switched off, and fluorescent images were taken after varying times of discharge. As described in section 3.2.6.1, due to the finite height of the dumbbell potential the fastest atoms escape the trap, leaving a reduced number of atoms with a reduced, effective temperature to interact with the potential. For the trap used in this experiment, with a potential height of approximately  $60 \mu\text{K}$ , and atoms at an initial temperature of  $40 \mu\text{K}$  after the sub-Doppler cooling step, this leaves a population of atoms with an effective temperature of  $25 \mu\text{K}$ . Due to scattering of light from the relatively near resonance trapping beam used to create the dumbbell potential, the resulting trap has a lifetime of  $\tau \approx 75 \text{ ms}$ . This scattering will also increase the temperature of the atom cloud, although this is not taken into account for this

analysis.

#### 4.1.1 Details of Parameters varied in Experiment

The dumbbell potential used has reservoirs with a diameter of  $600 \mu\text{m}$ , and a channel with a length of  $150 \mu\text{m}$ . The width of the channel was set to a different value for each experimental run, varying from  $48 \mu\text{m}$  to  $580 \mu\text{m}$  in 8 steps. The first image after the MOT release was taken at 5 ms, with subsequent images being taken at 10 ms intervals after that, to a maximum time of 75 ms. After this point, the atoms number is so low due to light scattering losses, that useful information is no longer able to be obtained. For each time step, 8 separate runs were done, and the resulting atom numbers averaged together to reduce random noise in the signal.

#### 4.1.2 Data

An example of the images obtained for one run of the experiment are shown in figure 4.1. The atom density is shown in false color, with each frame normalized separately. The dynamics appear qualitatively to match what one would expect, and what our description above predicts; the atoms start mostly localized to one reservoir, then as time evolves, they come closer to being evenly distributed between the two reservoirs. To get a quantitative measure of the dynamics in the system, we want to measure the normalized number difference between the reservoirs,  $\frac{N_2 - N_1}{N_2 + N_1}$ . We get the number of atoms in either reservoir,  $N_i$ , by counting the photons captured in an image for the pixels over only that reservoir. The normalized number difference

is plotted as a function of time in figures 4.2 and 4.3 for the channel widths used in the experiment. Each of these plots includes a fit to an exponential decay in red, which we would expect for an overdamped oscillator. The blue lines in these figures show the lower and upper bound of the standard errors in the fitted time constants. Again we see that it qualitatively follows what we expect, with the addition of an oscillation that might be explained by the inductance that we have derived causing the system to be underdamped. These oscillations are only significant for very wide channels.

For these plots, it should be noted that the first two to three data points are not expected to fit our description of the capacitor dynamics. At the times the images for these data points are taken, there are a significant number of high energy atoms still in the frame that are not bound in the potential. These are the atoms above the cutoff in the velocity distribution that we have assumed are gone. Until these atoms are actually gone from the trap, we do not expect the system to act as we have described. For this reason, the first three data points are not taken into account in the fits.

### 4.1.3 Comparison to Expected Values

Plugging values for our system into equations 2.41 and 2.38, we obtain values for our atom circuit elements;

$$C_c = \frac{n_e A}{2kT} = \frac{n_e A}{2 \left(1.38 \times 10^{-23} \frac{\text{J}}{\text{K}}\right) (25 \times 10^{-6} \text{ K})} = n_e A (1.45 \times 10^{27} \text{ J}^{-1}), \quad (4.1)$$

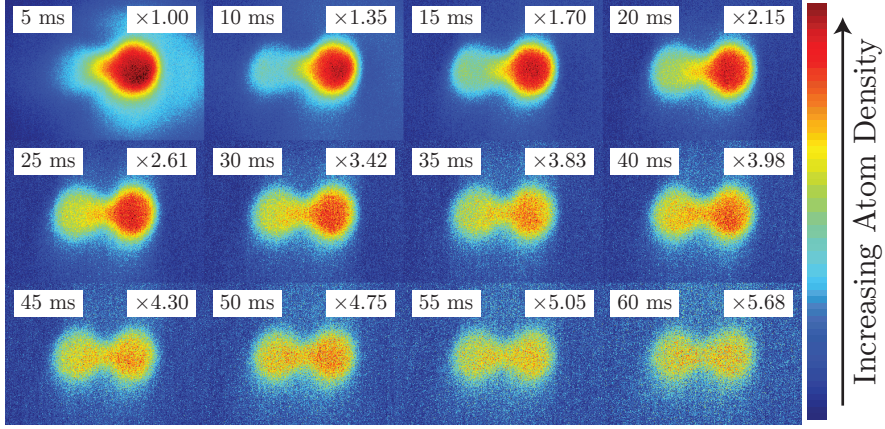


Figure 4.1: After the MOT is released over one reservoir of our dumbbell potential, fluorescence images are taken after various TOF. Here we show a composite of these images for a channel width of  $288 \mu\text{m}$ . The time after release of the MOT is shown on each frame, and varies from 5 ms to 60 ms. Since atom losses are significant over these time scales, one scaling cannot be used for the entire image and each frame is individually scaled. The scale factor for each frame is also shown.

$$R_c = \frac{\sqrt{2\pi mkT}}{n_e w} = \frac{\sqrt{2\pi (1.44 \times 10^{-25} \text{ kg}) (1.38 \times 10^{-23} \frac{\text{J}}{\text{K}}) (25 \times 10^{-6} \text{ K})}}{n_e w} = \frac{1}{n_e w} \left( 1.77 \times 10^{-26} \text{ kg} \frac{\text{m}}{\text{s}} \right), \quad (4.2)$$

and

$$L_c = \frac{2ml}{n_e w} = \frac{l}{n_e w} (2.89 \times 10^{-25} \text{ kg}). \quad (4.3)$$

Since our system is as damped, harmonic oscillator, one of the first parameters that we should look at is the damping constant, or damping ratio

$$\zeta = \frac{R_c}{2} \sqrt{\frac{C_c}{L_c}} = \frac{1}{n_e w} \left( 8.85 \times 10^{-27} \text{ kg} \frac{\text{m}}{\text{s}} \right) \sqrt{n_e^2 A \frac{w}{l} (5.02 \times 10^{51} \text{ J}^{-1} \text{ kg}^{-1})} = 0.627 \sqrt{\frac{A}{wl}}. \quad (4.4)$$

This unitless parameter tells us how damped the system is. For  $\zeta < 1$ , the system will be underdamped, and can be described by an oscillation with exponentially

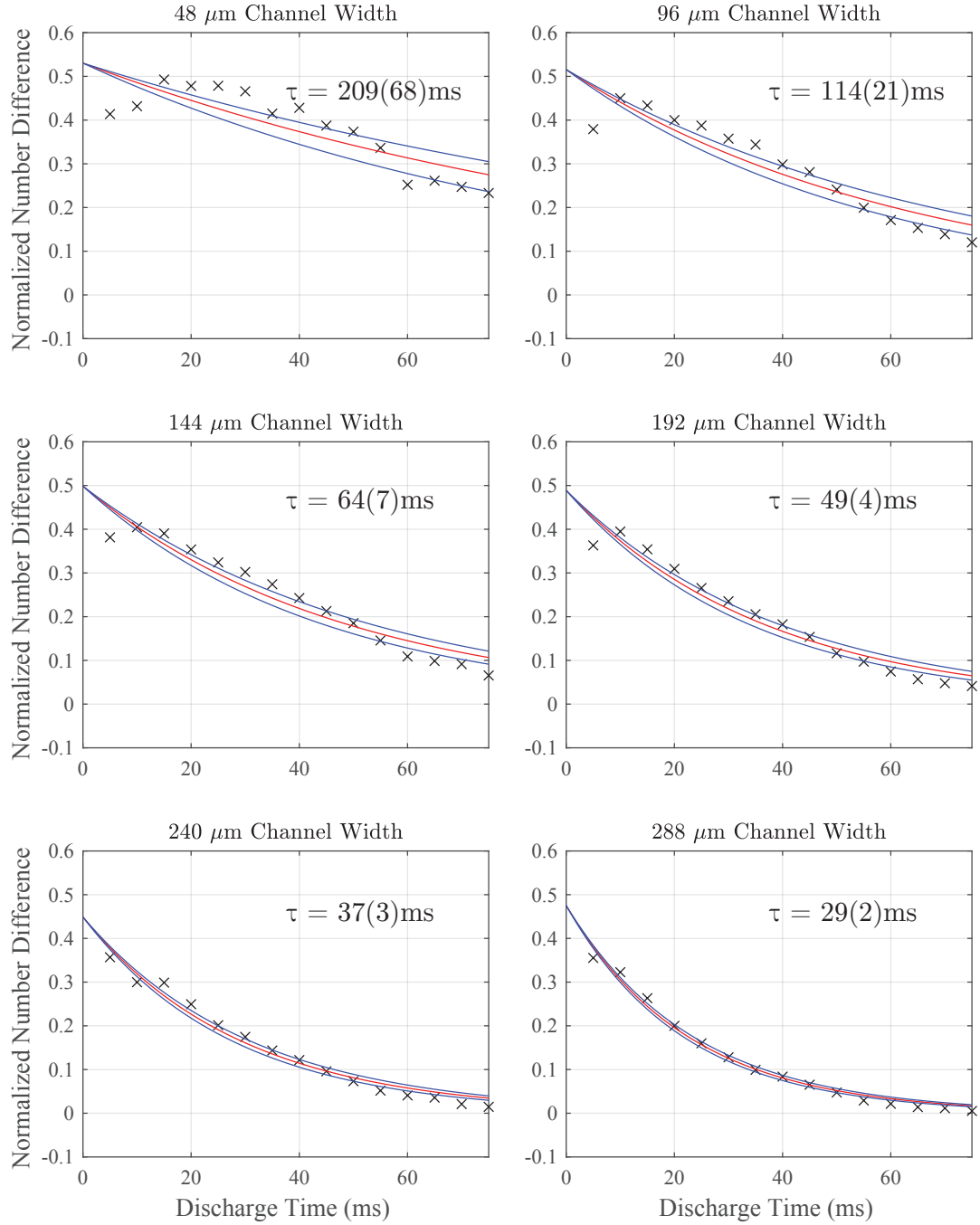


Figure 4.2: In each of these plots, the experimentally measured normalized number difference between the two reservoirs  $\frac{N_2 - N_1}{N_2 + N_1}$  of the thermal dumbbell system is plotted as a function of time after release from the MOT (black  $\times$ s). A fit of this data to an exponential decay is also shown (red line) with decay time constant  $\tau$ . Also shown are plots for decay with  $\tau_{er} = \tau \pm \sigma_\tau$ , where  $\sigma_\tau$  is the standard error in the fitting parameter for the fit (blue lines). Each plot is labeled with the channel width for that experimental run. This is the only variable adjusted in this experiment.

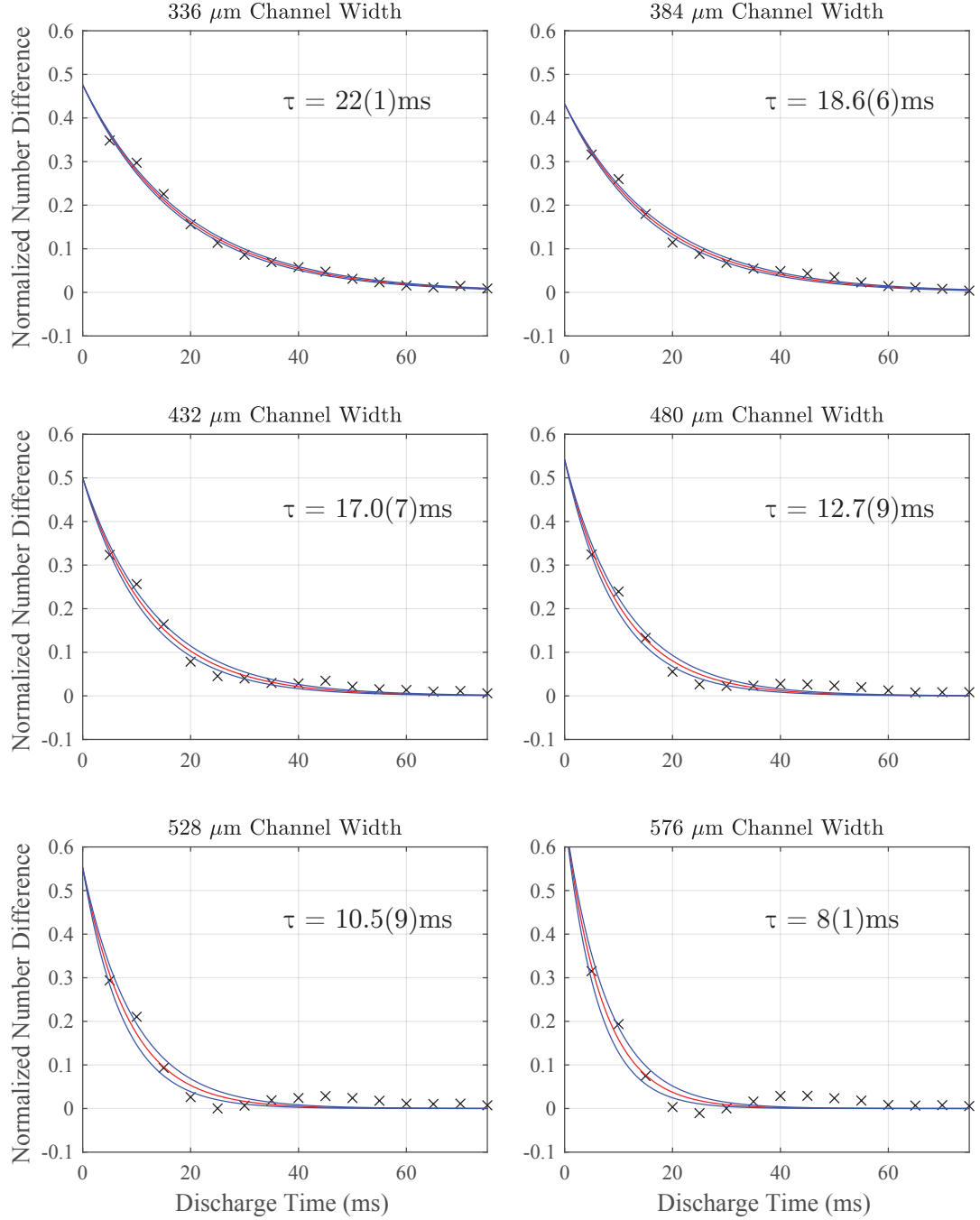


Figure 4.3: In each of these plots, the experimentally measured normalized number difference between the two reservoirs  $\frac{N_2 - N_1}{N_2 + N_1}$  of the thermal dumbbell system is plotted as a function of time after release from the MOT (black  $\times$ s). A fit of this data to an exponential decay is also shown (red line) with decay time constant  $\tau$ . Also shown are plots for decay with  $\tau_{er} = \tau \pm \sigma_\tau$ , where  $\sigma_\tau$  is the standard error in the fitting parameter for the fit (blue lines). Each plot is labeled with the channel width for that experimental run. This is the only variable adjusted in this experiment.

decaying amplitude. For  $\zeta = 1$ , the system is critically damped, and will follow an exponential decay. For  $\zeta > 1$ , the system is overdamped and again will follow an exponential decay, with the inductance value not significantly altering the dynamics. Note that for our system, this parameter does not depend on the number of atoms in the system, and as long as the area of either of the reservoirs is greater than about 2.5 times the area of the channel, we are in the overdamped regime. This means that the inductance in our system does not significantly influence the dynamics except possible for the widest channels, since our channel is short compared to the size of the reservoirs. For these wide channels, however, many of our assumptions going into this analysis break down and this is no longer a valid description. Specifically, we have assumed that either reservoir is in equilibrium, with the effusion into and out of it acting as a perturbation. This is obviously not true for these large channel widths, where we are basically seeing a simple expansion of an atomic cloud into a larger area. Therefore, for the experimental runs that we expect to be well described by this model, we are in the overdamped regime.

In this regime, we can describe our dynamics by a simple exponential decay, with a decay time

$$\tau = RC = \frac{A}{w} \left( 25.6 \frac{\text{s}}{\text{m}} \right). \quad (4.5)$$

Figure 4.4 shows the expected values for this decay time compared to fits to the data taken from the experiment. The error bars are the standard error in the fitted decay times, and the two blue lines indicate the margin of error in our expected value of the time constant for a  $5 \mu\text{K}$  error in the measured temperature. Given

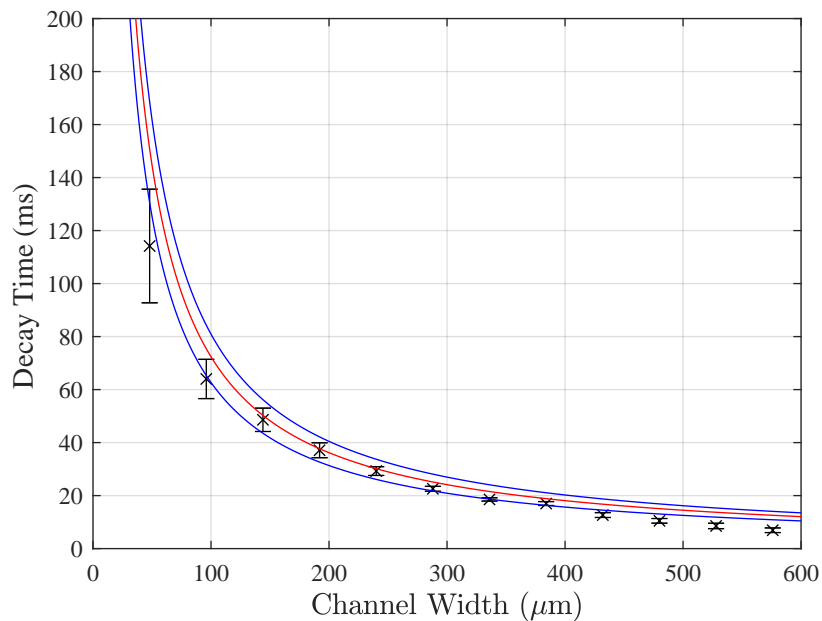


Figure 4.4: The experimentally measured decay time  $\tau$  is plotted (black  $\times$ s) as a function of channel width. The decay times are from the fits in figures 4.2 and 4.3, with error bars given by the standard error in the fit (depicted as the blue lines in figures 4.2 and 4.3). Also plotted is our expected decay times that we calculate in chapter 2 with no fitting parameters (red line), as well as the expected values if for a temperatures  $5 \mu\text{K}$  above and below our assumed temperature of the system (blue lines). The higher (lower) temperature corresponds to the lower (upper) blue line. The value of  $5 \mu\text{K}$  is chosen as a rough guess to our certainty in our effective temperature.

the assumptions going into the effective temperature used for the theoretical values because of the truncated velocity distribution, we expect a possible error of this order. This is by far the largest contribution to error in this system.

With the exception of the extremely large channel widths, where we expect to see departures from theory due to breaking of assumptions in the theory, it is clear that our theoretical description is consistent with what we observe in experiment. Both the functional form of the dissipative dependence on channel width and the overall scaling factor are quite close to what we expect. It is important to note here that there are no fitting parameters in this plot. This is not a fit, but rather a calculation based only on the geometry and temperature of our system.

## 4.2 BEC System

For the superfluid experiment, a sample of atoms was confined vertically by the red detuned sheet ODP. This sheet has a vertical trapping frequency of  $\omega_z/2\pi \approx 529(2)$  Hz. The sheet also confines the atoms in the horizontal plane with a trapping frequency of  $\approx 9$  Hz. The number of atoms can be varied from  $10^5$  to  $5 \times 10^5$  atoms, corresponding to equilibrium chemical potentials of  $\mu_e/\hbar \approx 2\pi \times (500 \text{ Hz})$  to  $\mu_e/\hbar \approx 2\pi \times (1000 \text{ Hz})$ . This roughly square root scaling of chemical potential comes from our derivation and measurement shown in section [2.2.1](#)

The dumbbell potential, created using the direct intensity masking procedure described above, consists of reservoirs with a diameter  $D = 40(3) \mu\text{m}$ , and a channel length of  $l = 22(1) \mu\text{m}$ . The Thomas-Fermi width of the atoms in the channel is

measured to be  $d = 6.4(2) \mu\text{m}$ , and is independent of both the total atom number and the intensity of the beam used to create the dumbbell potential. The 1-D density of the atoms in the channel does however vary with these parameters.

#### 4.2.1 Details of Parameters varied in Experiment

The two parameters that were varied for the experiment are the total atom number  $N$ , and the potential height of the dumbbell trap  $U_m$ . The different atom numbers were measured to be nominally  $125(6) \times 10^3$ ,  $229(9) \times 10^3$ ,  $331(11) \times 10^3$ , and  $472(22) \times 10^3$  atoms.  $U_m/h$  was varied from approximately 2.25 kHz down to the lowest possible value before atoms start leaking out of the trap, which is limited by the chemical potential, and thus atom number. Four evenly spaced points were taken over this range, with the exception of the lowest atom number, which only has three data points due to this limitation in lowest possible value.

#### 4.2.2 Data

A sequence of images taken for an atom number of  $495(16) \times 10^3$  is shown in figure 4.5. The normalized number difference between the two reservoirs is plotted for all data runs in figures 4.6, 4.7, 4.8, and 4.9.

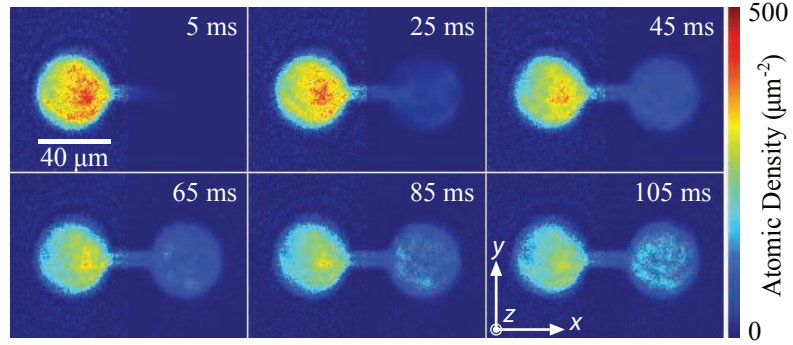


Figure 4.5: After the gate beam over the channel is released, the BEC is allowed to evolve for a variable amount of time after which we measure the optical density. The full method for this takes approximately 8 individual experimental runs, and is described in detail in the text. Here we plot a composite of these optical densities for a few of the evolution times for a group of  $495(16) \times 10^3$  atoms.

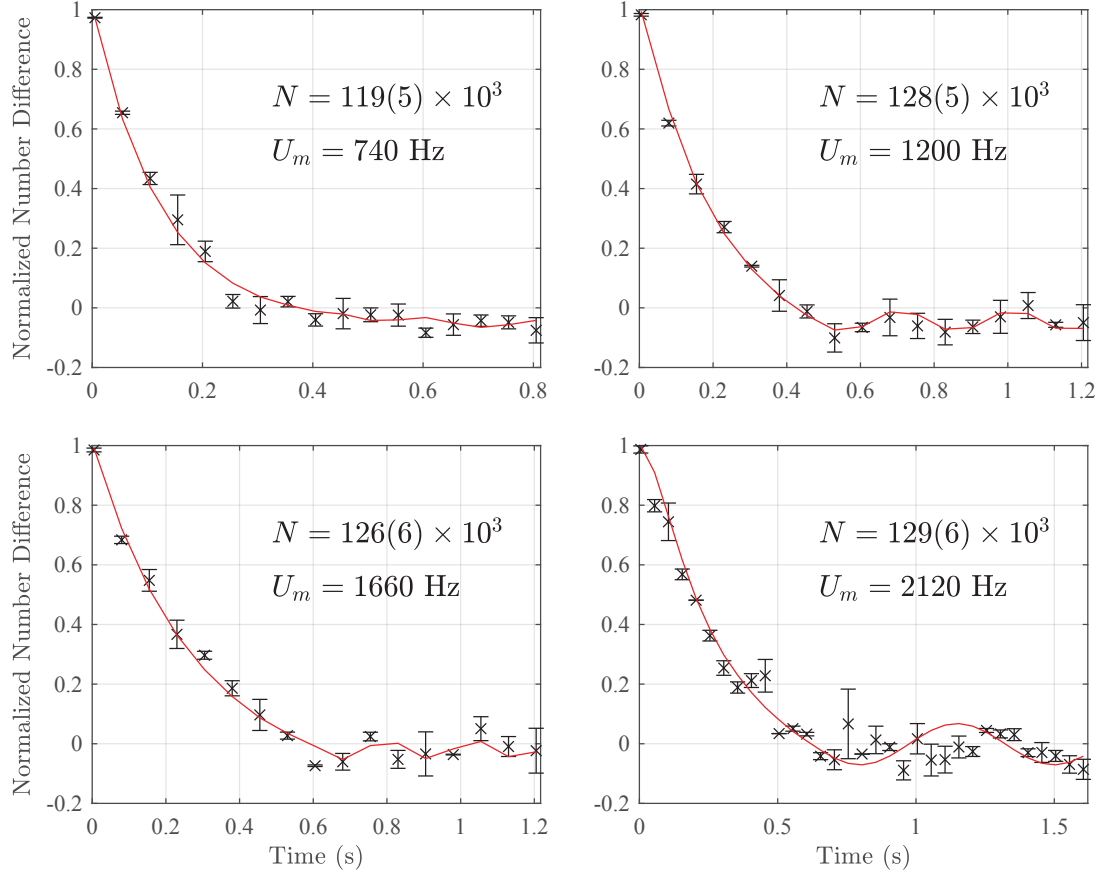


Figure 4.6: The measured normalized number difference between the two reservoirs is plotted (black  $\times$ s) as a function of time after gate release for the system with nominally  $125 \times 10^3$  atoms. Each plot is for a different value of dumbbell potential height  $U_m$ , which is shown on each plot along with the atom number for that run, which varied slightly around the nominal value. The red curve shows a fit to our circuit model given in equations 2.11, 2.12, and 2.13.

### 4.2.3 Component Values

The fits in these plots of our data are numerically calculated best fits to the coupled set of differential equations that describe our system (equations 2.11, 2.12, and 2.13). This model contain three independant fitting parameters,  $\tau = RC$ ,  $\omega^2 = 1/LC$ , and  $I_c$ . Although the functional form of the current-phase relation for

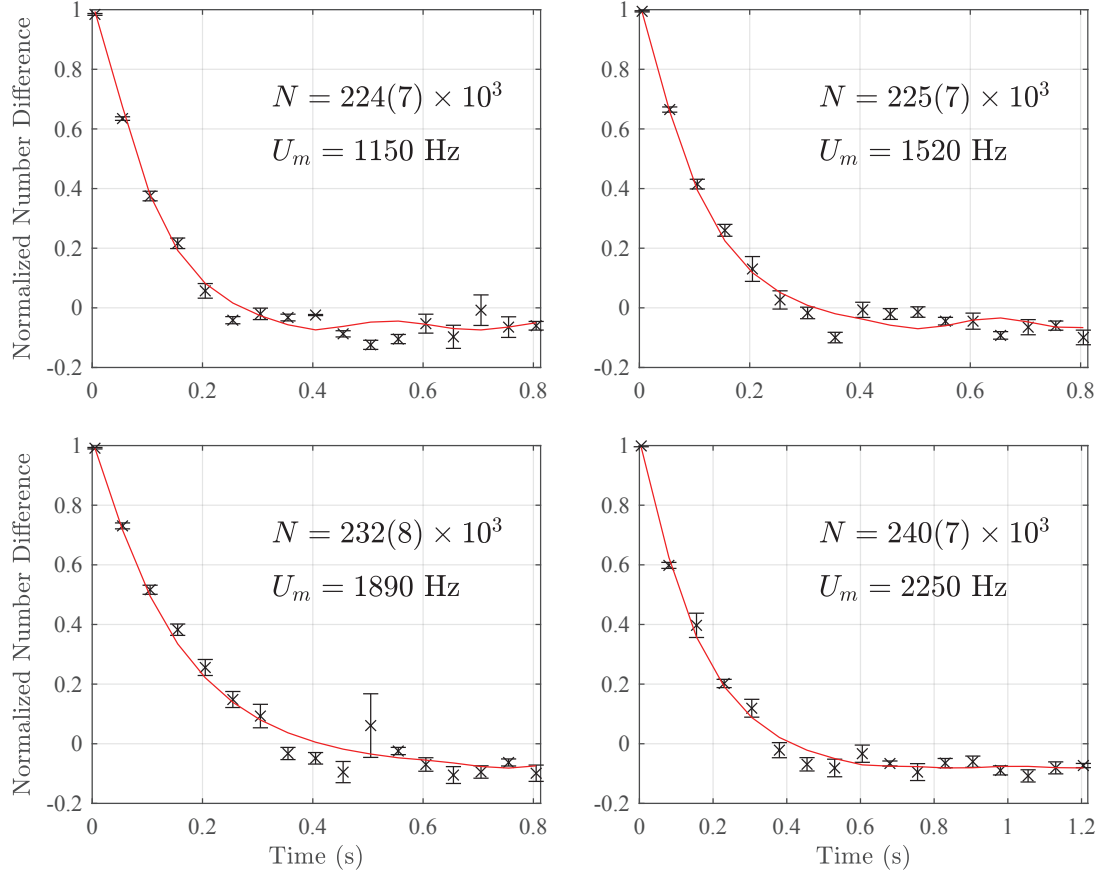


Figure 4.7: The measured normalized number difference between the two reservoirs is plotted (black  $\times$ s) as a function of time after gate release for the system with nominally  $230 \times 10^3$  atoms. Each plot is for a different value of dumbbell potential height  $U_m$ , which is shown on each plot along with the atom number for that run, which varied slightly around the nominal value. The red curve shows a fit to our circuit model given in equations 2.11, 2.12, and 2.13.

our weak link is not known, we take to be  $f(\gamma) = \sin\gamma$  for mathematical simplicity.

Changing the form, however, does not significantly alter the fits as long as  $f(\gamma)$  is  $2\pi$ -periodic, which will always be the case.

Since we have three fitting parameters in our model, and we are attempting to compare to four calculated values ( $C$ ,  $R$ ,  $L$ , and  $I_c$ ), we must take one of these

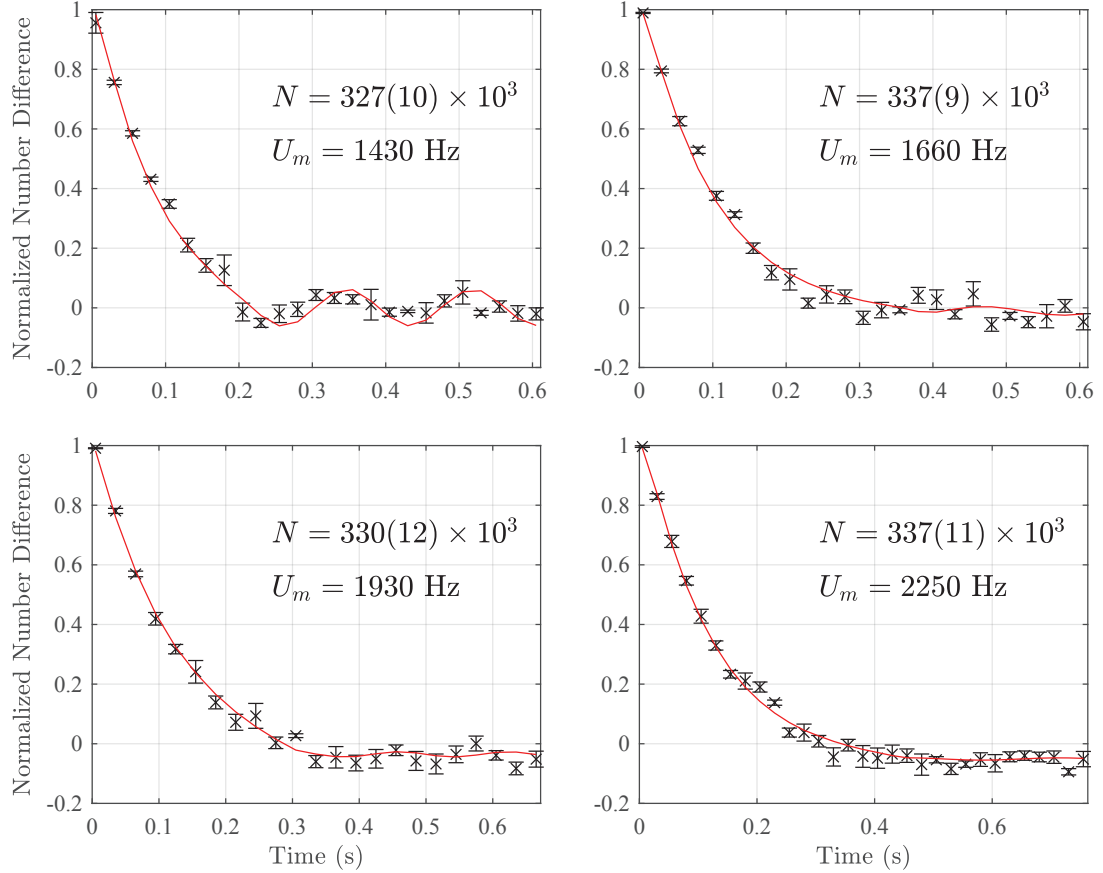


Figure 4.8: The measured normalized number difference between the two reservoirs is plotted (black  $\times$ s) as a function of time after gate release for the system with nominally  $333 \times 10^3$  atoms. Each plot is for a different value of dumbbell potential height  $U_m$ , which is shown on each plot along with the atom number for that run, which varied slightly around the nominal value. The red curve shows a fit to our circuit model given in equations 2.11, 2.12, and 2.13.

to be known *a priori*. Since we understand the chemical potential and capacitance with the least uncertainty, we take  $C$  to be known and we pull values for  $R$ ,  $L$ , and  $I_c$  out of our fits to compare to theory. Figure 4.10 shows a comparison of our calculated and measured conductance, giving us a comparison of  $R$ . Figure 4.11 shows a comparison of our calculated and measured inductance. Figure 4.12 shows

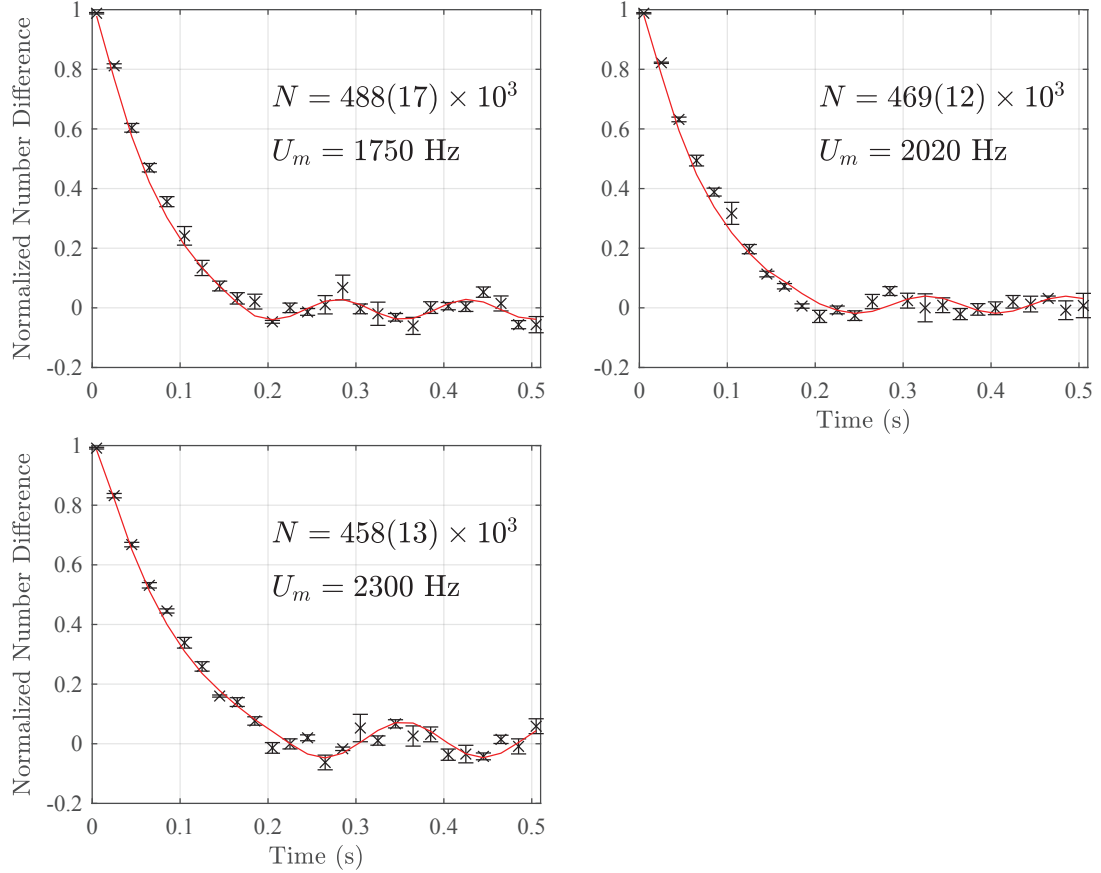


Figure 4.9: The measured normalized number difference between the two reservoirs is plotted (black  $\times$ s) as a function of time after gate release for the system with nominally  $470 \times 10^3$  atoms. Each plot is for a different value of dumbbell potential height  $U_m$ , which is shown on each plot along with the atom number for that run, which varied slightly around the nominal value. The red curve shows a fit to our circuit model given in equations 2.11, 2.12, and 2.13. Because the chemical potential of this sample of atoms is significantly higher than the other values tested, we were unable to lower the dumbbell potential height below the lowest value used here due to loss of atoms from the trap. This is why there are only three potential heights used for this atom number.

a comparison of our calculated and measured  $I_c$ .

As described previously, the conductance should be linear in  $n_{1D}$ , and this is found to be true, with a linear fit to the data shown in the plot. The dependence

of  $G$  on the dumbbell potential height and atom number is a bit more complex, and is what we use to quantitatively compare the results to our derived Feynman conductance. This data is also plotted in figure 4.10, with the atom number groups distinguished by color, with a fit to our expected form of the resistance shown with the solid lines. The only parameter in this fit is an overall scaling factor  $\alpha_F$ , such that our measured  $G = \alpha_F G_F$ , where  $G_F$  is our derived conductance. The model reasonably captures the trend, and the best fit parameter  $\alpha_F = 0.47(10)$ . The value of  $\alpha_F$  being less than unity implies that there is higher dissipation than what we have accounted for in our theory. Since we have not taken into account any collective excitations other than vortices, this is reasonable.

Figures 4.11 and 4.12 plot the ratio of the experimental to theoretical values of  $L$  and  $I_c$  respectively. The mean and standard deviation of the ratios are shown by the highlighted region in the plots as well. The value that we find for the inductance is consistent with unity, showing agreement between the experiment and theory. On the other hand, the value obtained for the critical current is significantly smaller than unity. As with the fitting factor found for the dissipation in the system, the direction of this discrepancy tells us that there are excitations we are not taking into account, and we are experiencing a higher dissipation than we are accounting for in the theory.

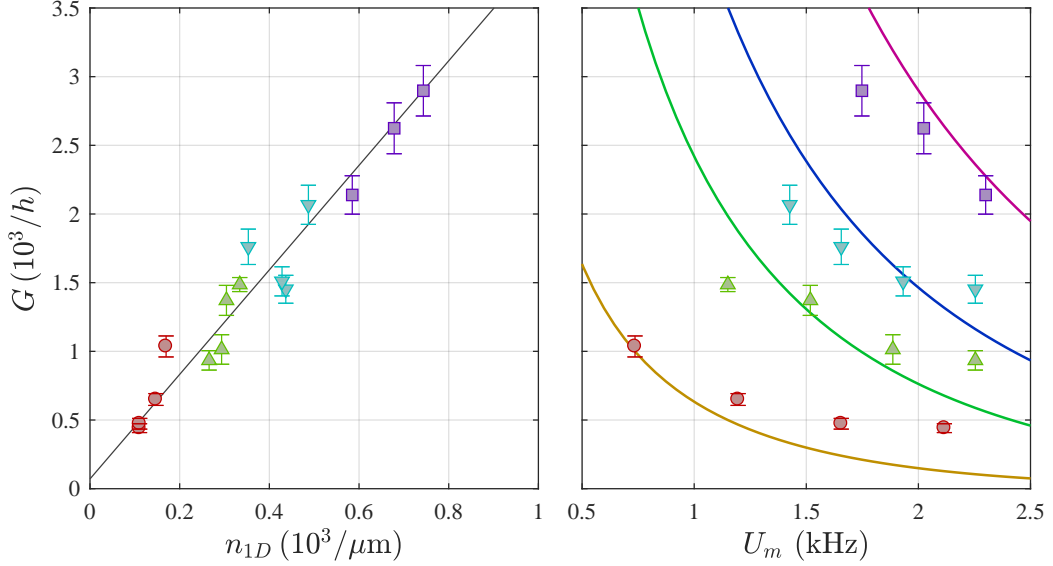


Figure 4.10: From the fits in figures 4.6, 4.7, 4.8, and 4.9, and from our calculated capacitance value, we are able to determine the conductance of the channel in our dumbbell for each experimental run performed. The plot on the left shows this conductance as a function of the 1D atom density in the channel ( $n_{1D}$ ). According to our theory, this plot should show a linear relationship that intercepts the origin. The black line is a fit to this model. The points are grouped in color by atom number. The red, green, blue, and purple points correspond to total atom numbers of nominally  $125(3) \times 10^3$ ,  $230(4) \times 10^3$ ,  $333(5) \times 10^3$ , and  $450(8) \times 10^3$  atoms. The plot on the right shows the conductance as a function of dumbbell potential height  $U_m$ , again with the same atom number grouping. The colored lines correspond to a fit of our Feynman resistance model to our data for all combined runs. The individual curves are this fit plotted at for the average atom number of each grouping, with colors matching the experimental data groups.

#### 4.2.4 Observation of Vortices

Since our model of dissipation in our system involves the creation of vortices in the superfluid, we have another avenue by which to assess the model. While our imaging resolution is not adequate to directly observe vortices *in-situ* in our

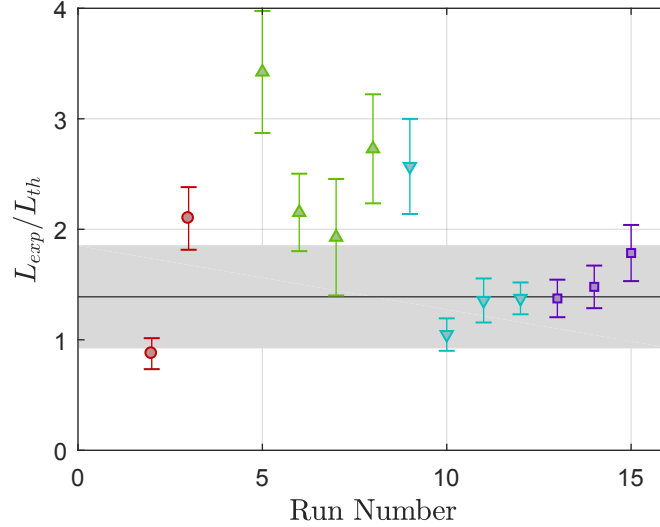


Figure 4.11: From the fits in figures 4.7, 4.8, and 4.9, and from our calculated capacitance value, we are able to determine the inductance of the channel. Here we plot the ratio of experimental to theoretical inductance for each experimental run. The atoms are grouped by color similar to figure 4.10. The black line represents the weighted mean of the values, and the shaded area shows the weighted standard deviation of the values.

superfluid, which have core sizes on the order of  $1 \mu\text{m}$ , we can image them in time-of-flight images, as the core size increases significantly when the cloud expands. To investigate this, we allow an initially imbalanced dumbbell system to come to equilibrium, discharging for a time on the order of half a second. This is long enough for the system to have damped out any difference and any oscillations. After this, we turn off all traps completely. After a 10 ms TOF, we image the atoms. A sample of these TOF images is shown in figure 4.13 for a system that was given 612 ms to discharge, and excitations can very clearly be seen in the initially empty reservoir.

The excitations qualitatively resemble the structure of vortices after expansion, although determining this without doubt is not possible without some sort

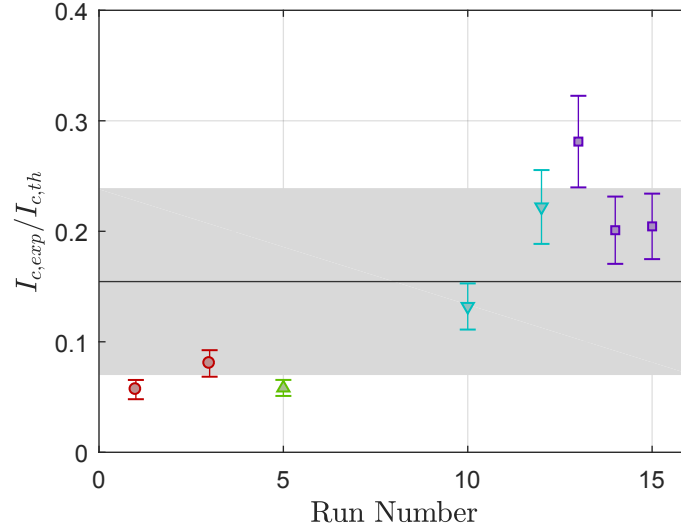


Figure 4.12: From the fits in figures 4.7, 4.8, and 4.9, and from our calculated capacitance value, we are able to determine the critical current for vortex formation at the exit of the channel. Here we plot the ratio of experimental to theoretical critical current for each experimental run. The atoms are grouped by color similar to figure 4.10. The black line represents the weighted mean of the values, and the shaded area shows the weighted standard deviation of the values.

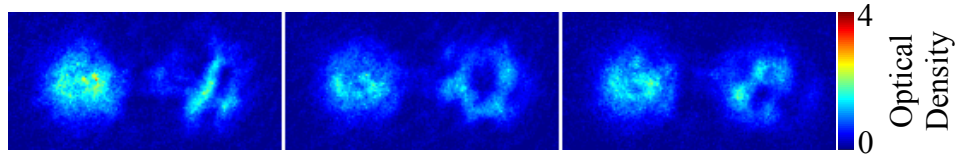


Figure 4.13: Images taken after a discharged dumbbell potential is released completely from the trap and allowed to expand in TOF for 10 ms. The system was allowed to discharge for 612 ms prior to release, which is well past the amount of time necessary to come to equilibrium. Excitations can clearly be seen in the initially empty reservoir which is what we expect based on our model.

of velocity measurement (interferometric measurement, Raman spectroscopy, etc.).

These excitations can be seen in nearly all TOF images after atoms have at least

partially populated both reservoirs. The fact that they nearly all exist in the initially empty reservoir is strong evidence in favor of our description of excitation formation, namely that it occurs on the exit of flow from the channel.

### 4.3 Conclusions

Through the course of this experiment, we have developed two new techniques for creating arbitrary, 2D, optical dipole potentials for use in ultracold neutral atom research. Both of these techniques are borrowed from other fields; the GPC technique comes from microscopy and the fabrication process used to make the amplitude masks for the direct intensity masking technique is borrowed from the manufacture of microelectronics. Both of these techniques heavily adapt many aspects of their predecessors in order to make them applicable to our system. Each provides its own advantages and disadvantages, and depending on the atomic system being studied, optical access to the cold sample, the available light sources for dipole traps, the necessary intensities for the dipole traps, available fabrication facilities, and many other factors, one can choose whichever method is best suited.

Using these newly adapted techniques, we have studied dissipation in the flow of a superfluid between two reservoirs connected by a narrow channel. The model that we use to describe this system is analogous to a superconducting circuit. The motivation behind drawing this parallel is similar to that for other systems. Many physical systems are described by similar differential equations. Some dynamics are already well understood in certain systems, and if we can show that other systems

are fundamentally similar we already have a framework for analyzing them. An example of this is the use of conductance and circuit models to analyze vacuum system design. Even our thermal system is different than this particular example though, as collisions with the walls of our potential are very different in nature to collisions with a physical vacuum chamber wall.

These parallels also provide us with insight into what might be possible with our system. Many complex electronic circuits already exist, and if we can determine a method to mathematically switch between the systems, we can see what devices we might be able to create with a cold atom circuit. An example of this is the existence of superconducting SQUID circuits. These devices make use of circuits with a ring geometry and Josephson junctions to create an extremely sensitive magnetometer. Drawing our parallels to the cold atom superfluid, we can conceivably create a rotation sensor using the same principles.

Our dumbbell geometry creates an atom circuit that is analogous to a superconducting circuit consisting of a capacitor, an inductor, a resistor and a Josephson Junction. A surprisingly large number of components for such a simple system. The dissipation in the system is described by a model of vortex-like collective excitations being produced at either side of the channel when the superfluid flows into a reservoir above some critical current. This description of vortex production has existed for decades, but this is to our knowledge the first direct experimental investigation of its applicability to a real system. We show that the dissipation we see in our system is consistent with this description, except for an overall scaling factor. We also directly observe vortices in the reservoirs after dissipation has occurred. The

fact that we observe a dissipation that is greater than what would be expected for vortices alone, and that we observe a lower than expected critical current, both indicate that there are likely other excitations causing dissipation in our system in addition to vortex production.

### 4.3.1 Future Directions

The flexibility of the experimental techniques that we have developed allow for many future experiments following up on this work, in addition to being applicable to many completely different systems. One possibility is to take more careful measurements with smaller atom imbalances, where the current stays below the critical current, to study the persistent oscillation in the  $LC$  system. This oscillation can also be driven with the addition of a variable strength potential over one of the reservoirs (such as an additional ODP). With this driving potential, careful study of the crossover to the dissipative regime can be carried out.

The geometry of the system could also be altered to look more directly the Feynman mechanism of vortex production. In our system, the reservoirs are far from infinite, and the current is not constant. If a geometry with larger reservoirs were created, one could imagine a system in which one of the reservoirs is “squeezed” by an additional ODP to create a constant current. With high enough imaging resolution, individual vortices may even be directly observable, and countable, *in-situ*.

Our techniques can also be taken further with the use of new devices like 2D

micro-mirror arrays. These can be used to create a sort of combination of our two techniques, allowing computer control of a direct intensity mask. The speed of these devices could even allow real-time manipulation of the potential, even to the point where rapid switching may some day be able to be used to create time averaged potentials that are individually, continuously adjustable and addressable at each pixel. With such a system, not only could we further research the physics that we have investigated here, but conceivably any 2D, time dependant potential system can be created, allowing study of limitless other problems.

## Appendix A: Details of Cooling Methods

### A.1 Cooling and Trapping Methods

#### A.1.1 Electronic Structure of the Alkali Atoms

The initial cooling stages for both the sodium and rubidium apparatus rely on the absorption of momentum from photons to slow the atoms down. Because the momentum of a photon ( $p = h/\lambda \approx h/600 \text{ nm} \sim 10^{-27} \text{ kg m/s}$ ) is several orders of magnitude less than the momentum of an atom at room temperature ( $p = mv \approx \sqrt{mk_B T} \sim 10^{-23} \text{ kg m/s}$ ) which we are trying to slow down, we need the atom to be able to continually absorb and emit photons without moving into an internal electronic state that can no longer support this absorption. The alkali atoms provide a convenient method of insuring this due to their relatively simple electronic structures. The structure of the D<sub>2</sub> spectroscopic lines for rubidium and sodium are shown in figures [A.2 \[41\]](#) and [A.1 \[42\]](#) respectively. Due to selection rules for a single photon, dipole transition, the total angular momentum  $F$  must change by 0 or  $\pm 1$  when a transition from the  $S_{1/2}$  ground state to the  $P_{3/2}$  excited state. Because of this, if we tune our cooling light to use the transition from the ground state  $F = 2$  to the excited state  $F' = 3$  angular momentum state, the only

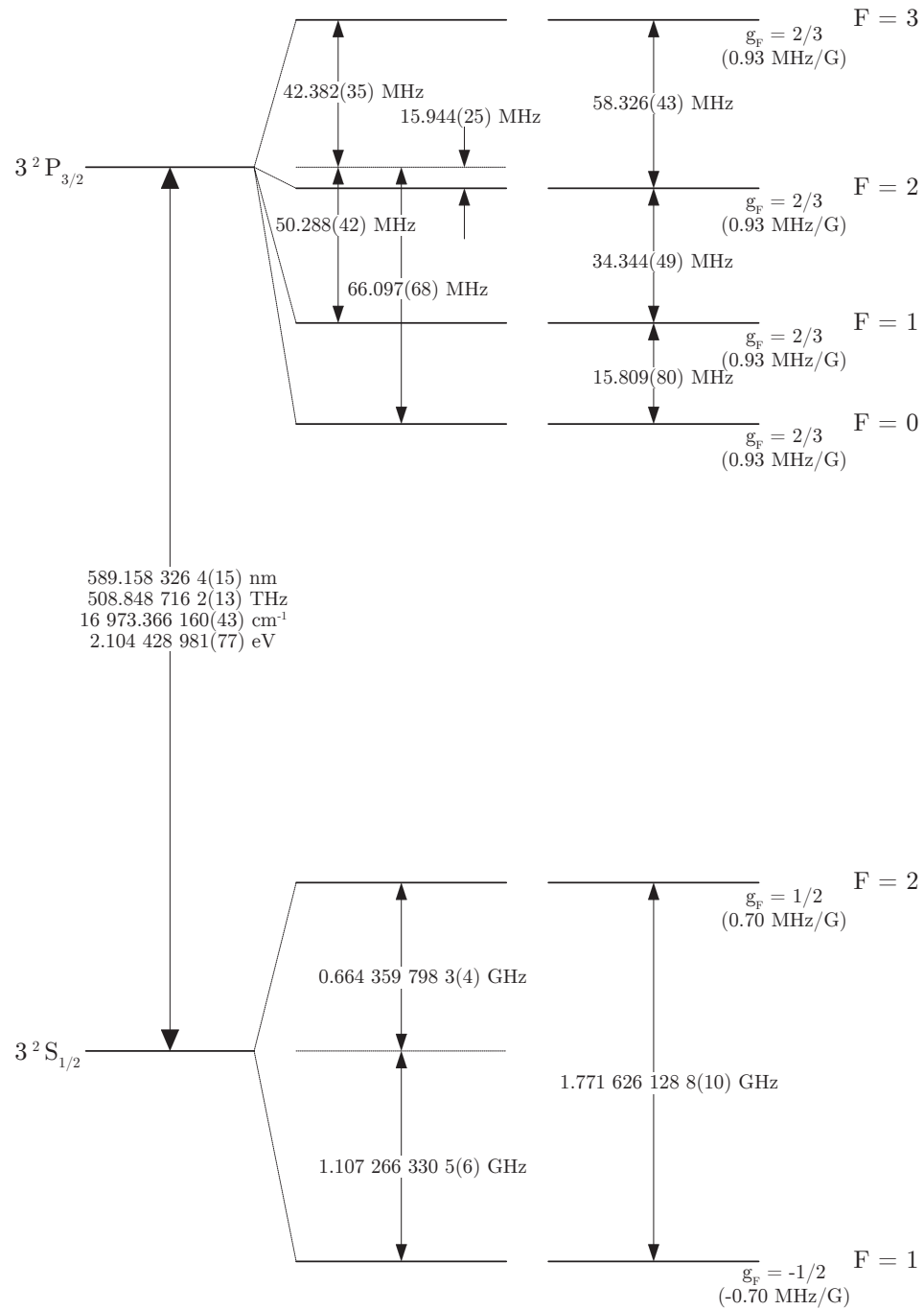


Figure A.1: The electronic structure of the Na D<sub>2</sub> spectroscopic line [42].

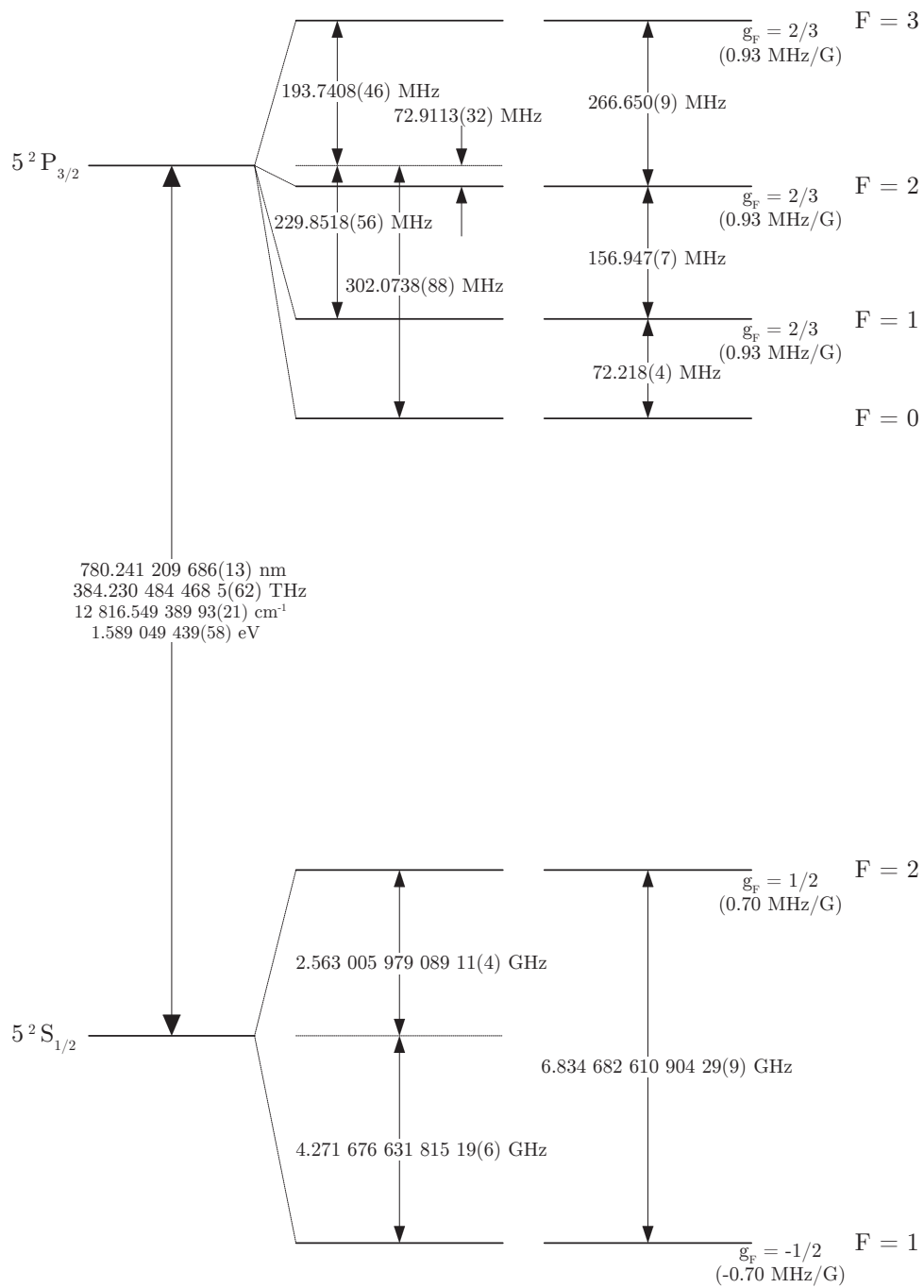


Figure A.2: The electronic structure of the  $^{87}\text{Rb}$   $D_2$  spectroscopic line [41].

available state for the atom to decay back down to is the  $F = 2$  state. This gives us our closed cycling transition to use for cooling.

In reality, the atoms will occasionally absorb an off-resonant photon, and get excited to the  $F' = 2$  state, in which case it can decay down to the  $F = 1$  ground state. If this happens, the atoms will be transparent to our cooling light, and will no longer be cooled. In order to compensate for this effect, we also use a second source of light in our cooling apparatus, called a repump beam, which is tuned to resonance on the  $F = 1$  to  $F' = 2$  transition. This light optically pumps any atoms that fall into the  $F = 1$  ground state into the  $F = 2$  ground state.

### A.1.2 Zeeman Slowing

For the BEC apparatus, the source of atoms is a sodium oven. The nozzle of the oven is kept at  $320^\circ\text{C}$ , and produces a beam of atoms at roughly that temperature that is directed toward the experimental chamber. At this temperature, the root-mean-squared (RMS) velocity of the atoms in the beam is  $v_{rms} = \sqrt{\frac{3kT}{m}} = 802 \text{ m/s}$ . In order to slow these atoms down to the capture velocity of a standard sodium MOT, which is approximately  $100 \text{ m/s}$ , we use what is known as a Zeeman-slower. The idea of the slower is to direct a beam of light counterpropagating with the atomic beam that is in resonance with the cycling transition. The atoms will absorb photons from the beam, along with their momentum, which slows the atoms down. Once in the excited state, the atoms will decay back down to the ground state, emitting a photon. This photon will also give a momentum kick to the atom,

however since this spontaneous emission is in a random direction each time, these momentum kicks will average to zero.

The situation is somewhat complicated due to the Doppler shifted frequency of light that the atoms actually see. In the frame of reference of the atoms exiting the oven, the light in the slowing beam will be shifted by  $\Delta f = \frac{\Delta v}{c} f_0 = \frac{802}{3 \times 10^8} \times 510 \text{ THz} = 1.4 \text{ GHz}$  relative to the lab frame. Since this is well over the linewidth of the transition,  $\Gamma = 2\pi \times 9.8 \text{ MHz}$ , some mechanism is needed to keep the light in resonance with the transition throughout the slowing process. In the aptly named Zeeman-slower, this mechanism is the linear Zeeman shift. A tapered solenoid is wound around the tube through which the atoms are directed. The current flowing through this coil produces a magnetic field that varies along the axis of propagation in such a way that the atoms are always in resonance with the light as they are slowed. Rather than having the magnetic field taper from some maximum, down to zero, we choose it such that it contains a zero along the slower beam. This is done for two reasons. First, it allows for the use of lower overall magnetic fields and currents. Secondly, it means that the atoms exiting the slower are out of resonance with the beam which is still passing over them. The velocity of the slowed atoms is  $< 10 \text{ m/s}$  [33]; well within the capture range of the MOT.

### A.1.3 Magneto-Optical Trapping

The first stage of cooling in the thermal rubidium system, and the second stage of cooling in the sodium BEC apparatus, is a magneto-optical trap (MOT).

The MOT uses two counterpropagating laser beams along each axis of a coordinate system centered at the trapping region. These beams are tuned approximately 2 natural linewidths below resonance of the cycling transition. In this setup, any atom that is moving will be moving toward the source of light in one of the beams. The light in this beam will be slightly closer to resonance than the light coming from the opposite direction due to the Doppler shift. Light will thus be preferentially absorbed from the beam opposing the motion of the atom, and the atom will be slowed when it absorbs the momentum from the photons in this beam. As with the Zeeman-slower, the momentum kicks from the randomly emitted photons will average to zero. The result is that any atom with motion in any direction will be slowed in that direction, giving a nearly linear damping to any motion of the atoms. While the atoms will not be trapped by this so-called optical molasses, they will be cooled to sub-milliKelvin temperatures.

In order to trap the atoms once they have been cooled by the optical molasses, we add a quadrupole magnetic field, produced with an anti-Helmholtz coil. This setup consists of two coils of wire in parallel planes, equally spaced from the center of the optical molasses beams. The current in the two coils flows in opposite directions, producing a zero-field at the center, with increasing field away from it. This produces a Zeeman shift in the cycling transition of the atom away from the center of the trap. If the correct circular polarization of light is chosen for each beam, this field puts any atom away from the center into resonance with the beam toward which it has moved, causing the atom to get a momentum kick back toward the center. The result of this is a position dependant restoring force which, along with the damping

of the optical molasses, gives us our MOT, closely resembling a damped harmonic oscillator.

The standard MOT discussed here has two main limitations when it comes to creating a BEC. First, with each photon that is absorbed to slow or trap an atom, another photon must be emitted. This photon gives a momentum kick to the atom. While this effect will average out over the many photons that are absorbed, it does impose a limit on the minimum temperature achievable through the mechanism described. For Na and  $^{87}\text{Rb}$ , these limits are  $235\ \mu\text{K}$  and  $146\ \mu\text{K}$  respectively. Secondly, if the density gets too high, the emitted photons from atoms in the center of the trap will exert a radiation pressure on the rest of the atomic cloud. This will limit the maximum density of the MOT, and if the end goal is a BEC where both low temperatures and high densities are required, it would be advantageous to overcome this limit. Fortunately, both of these limitations can be reduced with the techniques described below.

#### A.1.4 Dark-Spot MOT

To overcome the density limitation of the sodium MOT, we employ what is known as a dark-spot MOT. In this setup, our repump beam is split into two separate beams that intersect at the center of the MOT. Each of these beams has a dark mask blocking the center of the beam on the optical table. This mask is then imaged onto the plane of the MOT, producing a roughly spherical region centered at the MOT where there is no repump light. The result of this is that the atoms will be optically

pumped out of the cycling transition ground state, and will become dark to the trapping light soon after entering this central region. Once the atoms fall back out of the central region, they will be optically pumped back into the cycling transition ground state, and will again be trapped. Because the atoms are dark to the cooling light while in the center, they will not be absorbing, and more importantly emitting, photons at the same rate as without the dark-spot setup.

## A.1.5 Evaporative Cooling and Conservative Traps

### A.1.5.1 Evaporative Cooling

Evaporative cooling in a dilute atomic gas is very similar to the cooling of a cup of hot liquid left open to room temperature air. The hottest particles in the liquid are above the threshold for evaporation, and leave the cup. These particles have more than the average energy per particle, so the average energy of the particles in the remaining liquid, and hence the temperature of the liquid, goes down. The remaining particles rethermalize, and the process repeats. In our system, a sample of atoms is held in a trap with a potential depth large enough that essentially none of the atoms can escape. The depth is then lowered to a point where a small portion of the atoms are moving fast enough to leave the trap. This lowers the average energy of the sample, which then rethermalizes, and the process repeats. At some point, the temperature will eventually drop to a point where there are very few atoms escaping. The potential depth is then lowered again. This continues until the sample condenses.

At this point another advantage of the conservative traps is evident. In the MOT, the atoms in the sample are continually absorbing and emitting photons. Because of this, even if we were somehow able to obtain a pure quantum state, it would not last since the spontaneous emission would destroy any coherence. In the conservative traps used for evaporative cooling this is not the case, and the quantum states are free to exist and be studied.

### A.1.5.2 Magnetic Trapping

In order to cool below the recoil limit, we need a different kind of trap. One trap which allows such cooling is a magnetic trap. We have already seen that energy levels in an atom shift in the presence of a magnetic field. This can also be used to create a trap. If we have a sample of atoms in one of its ground states, the energy of those atoms will depend on the magnetic field that they are in. For an atom in the  $|F, m_F = +F\rangle$  state, its energy will increase with increasing magnetic field, thus it can be trapped in the minimum of a magnetic field. For an atom in the  $|F, -F\rangle$  state, its energy will increase with decreasing magnetic field, and it could be trapped in the maximum of a magnetic field. Unfortunately it is impossible to create a magnetic field with a local maximum in free space, so we are restricted to trapping atoms in the  $|F, +F\rangle$  state. In this state, the energy of the atom can be expressed as

$$E(B) = g_F m_F \mu_B B. \tag{A.1}$$

This energy does not depend on the direction of the field, since as long as an atom moves adiabatically through the field, it will stay aligned with it.

Now the problem is to create a magnetic field with a local minimum. Fortunately, we already have a setup to do this. We can use the same coils that we used to create the MOT. The anti-Helmholtz coils create a field that increases approximately linearly in any direction away from the center

$$\vec{B} = (B'x, B'y, -2B'z). \quad (\text{A.2})$$

There is a problem with this setup though. If an atom goes directly through the center, it is going through a point of zero magnetic field. At this point, the two spin states are degenerate, and the atom can spontaneously flip from the  $|F, +F\rangle$  to  $|F, -F\rangle$  state, and it will be lost from the trap. While this is not a significant loss mechanism for large, warm samples, when the temperature is decreased, and density increased, it becomes a serious problem.

A couple of solutions to this problem have been created. Some involve creating more complex fields that have a minimum without having a zero. The method we use is called a TOP trap [29, 34]. In this method, the anti-Helmholtz field is supplemented by an orbiting field that rotates with a period that is short compared to the relevant timescales of the problem. This field can be written as

$$\vec{B} = (B_0 \cos \omega t, B_0 \sin \omega t, 0), \quad (\text{A.3})$$

giving a total field of

$$\vec{B} = (B'x + B_0 \cos \omega t, B'y + B_0 \sin \omega t, -2B'z), \quad (\text{A.4})$$

the magnitude of which is

$$B(t) = \sqrt{(B'x + B_0 \cos \omega t)^2 + (B'y + B_0 \sin \omega t)^2 + (2B'z)^2} \quad (\text{A.5})$$

$$\approx B_0 + B' (x \cos \omega t + y \sin \omega t) + \frac{B'^2}{2B_0} [x^2 + y^2 + 4z^2 - (x \cos \omega t + y \sin \omega t)^2]. \quad (\text{A.6})$$

The time average of this gives us our effective field, which is

$$\langle B \rangle_t = B_0 + \frac{B'^2}{4B_0} (x^2 + y^2 + 8z^2). \quad (\text{A.7})$$

Now we effectively have a local minimum that is non-zero. We have also changed our trap into a harmonic trap that is more easily analyzed than the previous absolute value type trap. Another advantage of this trapping setup is that we can use the MOT to load the TOP trap since both traps are located at the zero of the anti-Helmholtz coils. The MOT can cool the atoms either from a slowed beam or directly from background gasses, and then the atoms can be transferred to the TOP trap for experiments.

### A.1.5.3 Evaporative Cooling in a Magnetic Trap

There are two main mechanisms for evaporatively cooling the atoms once they are in the magnetic trap. The first method used is called RF evaporation. When the atoms are in the magnetic trap, they experience a Zeeman shift of the energy levels within the atoms. In particular, for the alkali atoms, the difference in energies between the trapped and anti-trapped ground states will be separated by  $\Delta E = 2g_F m_F \mu_B B(\vec{r})$ . By directing RF radiation at the trap, we can couple atoms from the trapped to the anti-trapped state when the frequency used is equal to the

energy level splitting. Since the magnetic field is dependant on the distance from the center of the trap, we can tune this frequency to only out-couple atoms from the trap that are a specific distance from the center. The aim of evaporative cooling is to get rid of the highest energy atoms, leaving the remaining lower energy atoms to thermalize. Since only the high energy atoms will make it up the potential hill to arrive near the edge of the cloud, if we tune our RF frequency such that atoms only at the edge of the cloud get out-coupled, we are able to do just this. By ramping this frequency down gradually as the atoms thermalize, and the trap shrinks, we can significantly cool the atoms.

The other mechanism for cooling in a magnetic trap is called “circle-of-death” evaporation, and which only applies to the TOP trap [29,34]. In the TOP trap, The actual zero field point is circulating around the center of the trap at the TOP trap frequency. If an atom goes through this point, it will flip spin to the anti-trapped state, and be expelled from the trap. By adjusting the magnitude of the circulating magnetic field, the radius of this zero-field point can be controlled. As with the RF evaporation, if we adjust this radius to be just at the edge of the cloud of atoms and gradually lower it as the atoms cool, we can get rid of the high energy atoms, and effectively cool the sample.

#### A.1.5.4 Dipole Trapping

Another type of trap that allows sub-recoil cooling is an optical dipole trap. When an atom is exposed to light, the electric field of that light will induce an

oscillating dipole in the atom. If the light is below the resonant frequency of the atom, the dipole will be in phase with the electric field, and the energy of dipole in the electric field will be greater for greater electric field. If the light is above resonance, the dipole will be  $180^\circ$  out of phase with the electric field, and the energy of the dipole will be smaller for greater electric field. The result of this is that when an atom is exposed to light, if that light is blue detuned (above resonance) the atoms will have a higher potential energy in higher intensity regions, and will essentially be repelled by the light. For red detuned (below resonance) light, the opposite is true, and the atoms will be attracted to higher intensity regions. If a full quantum description is followed, it can be shown that the potential energy of the atoms as a function of intensity will be

$$U(I) = \frac{3\pi c^2 \Gamma}{2\omega_0^3 \Delta} I, \quad (\text{A.8})$$

where  $\omega_0$  is the resonant angular frequency and  $\Delta$  is the angular frequency detuning.

Both blue and red detuned traps have their advantages and disadvantages. For blue detuned traps, the atoms can be trapped in regions of zero intensity. This means that unwanted scattering of trapping light will be minimized. The down side is that it can be quite difficult to create light intensity fields with local minima in the shapes one might desire. Some such traps have been created using lasers with Bessel and Laguerre-Gaussian spatial modes. Also, there needs to be some additional trapping in the direction of propagation, since the zero persists along this direction.

Red detuned traps can be easier to create since a simple focused Gaussian

beams can be used to provide trapping in all three dimensions. Unfortunately, with red detuned traps the atoms are confined to the highest intensity part of the beam, where the scattering is the highest. The vast majority of dipole trap experiments have used red detuned traps however, as there is a relatively simple solution to this scattering problem.

The scattering rate of an atom exposed to light of intensity  $I$  is given by

$$\Gamma_{sc} = \frac{3\pi c^2}{2\hbar\omega_0^3} \left(\frac{\Gamma}{\Delta}\right)^2 I. \quad (\text{A.9})$$

Since the scattering rate falls off as  $1/\Delta^2$  and the potential only falls off as  $1/\Delta$ , the scattering rate will decrease for constant potential if the light is detuned farther from resonance. Commonly used sources are in the near IR part of the spectrum (1-2  $\mu m$ ) for atoms with resonances around 500-800  $nm$ . This does come at the cost of having to use quite high power beams, but modern fiber lasers are usually more than sufficient, commonly producing 10's of Watts at these wavelengths.

Even greater detunings have also been used, with sources near 10  $\mu m$ . In this case a lot of power is necessary ( $\sim 100W$ ), but CO<sub>2</sub> lasers at this wavelength easily surpass this. One advantage of these long wavelength, high power traps is that they can be quite large. This eliminates one of the major disadvantages of many other dipole traps, which is that they are generally much smaller than most MOTs, making it hard to efficiently load atoms from the MOT into the dipole trap.

### A.1.5.5 Evaporatively Cooling in a Dipole Trap

For a dipole trap, the mechanism used for evaporative cooling is quite simple; the intensity of the trapping light is gradually reduced. Since the maximum potential depth of the trap is proportional to the intensity of the light, and any atoms with higher energy than this potential height will escape, by gradually reducing the intensity of the trapping light as the sample loses the higher energy atoms, we can again effectively evaporatively cool the atoms. There is a big disadvantage to this method though. As the trapping light intensity is dropped, the trapping frequencies are also reduced. This means that the trap becomes bigger. This partially, but not completely, offsets the increase in phase-space density that we are attempting to achieve with the goal of producing a BEC. For this reason, in our experiments, we generally choose to perform the majority of cooling in the magnetic trap, and transfer to the dipole trap just prior to condensation.

## A.2 Imaging

### A.2.1 Fluorescence Imaging

Now that we have ultracold samples of atoms, we need to develop a method to measure their properties. For the thermal rubidium experiment, the method used is called fluorescence imaging. When the atoms are exposed to resonant light, they will absorb photons from it. After a short time ( $\sim 25$  ns for *Rb*), each atom will emit a photon in a random direction. If the incident light is well above the saturation

intensity, each atom will almost immediately absorb another photon, and the process repeats. If a portion of the emitted light is collected and imaged onto a CCD, the density of the atomic sample can be directly measured. When this imaging method is used in experiments, a short pulse of resonant light is directed at the atoms while the camera is exposing a frame. In order for this to be effective, the pulse must be short enough so that the atoms do not move appreciable during the pulse. For rubidium atoms at  $20 \mu K$ , this gives us a pulse length of about  $100 \mu s$  if we want an imaging resolution of  $10 \mu m$ . Since this limits the number of photons emitted, the solid angle of photon collection and quantum efficiency of the CCD must be high enough, and sources of noise low enough, to give the desired signal to noise ratio. One advantage of this type of imaging is that all of the sources of noise are random, allowing us to average them out over multiple images.

### A.2.2 Absorption Imaging

Another method, which we use to observe the sodium BEC atoms, is absorption imaging. We take a collimated probe beam that is tuned to the cycling transition of our atoms, and shine it over our atomic sample. The atoms absorb some of the light, and the intensity of the light as a function of position immediately after the atoms is given by

$$I(x, y) = I_0(x, y)e^{-n(x, y)\sigma}, \quad (\text{A.10})$$

where  $I_0(x, y)$  is the original intensity profile,  $n(x, y)$  is the integrated column density, and  $\sigma$  is the absorption cross section. We then image this intensity profile onto

a CCD. We can then calculate the integrated column density as

$$n(x, y) = \ln \left( \frac{I_0(x, y)}{I(x, y)} \right) \frac{1}{\sigma}. \quad (\text{A.11})$$

In practice, for each calculation, three images are taken. One image has no sample and no probe beam ( $I_{dark}$ ). One image has no sample but does have the probe beam ( $I_0$ ). The final image has the sample and probe ( $I$ ). We subtract the dark image from the other two to eliminate effects of room light or stray trap light getting into the camera. The equation used here assumes that  $I_0$  is below the saturation intensity, and that the optical density is less than about one.

### A.2.2.1 Partial Transfer Absorption Imaging

Getting an accurate measure of atom density over a large range of optical densities is not trivial. Not only are we limited by the signal to noise ratio of our optical system, there are a few non-linear effects that make it difficult to compensate for this. In order to get as accurate a count of atom number in the reservoirs of our system, we use a technique that is called partial transfer absorption imaging. This method uses on resonant absorption imaging, but lowers the observed optical density of the atomic cloud by transferring only a certain amount of atoms into the ground electronic state that is used for imaging. The rest of the atoms are very far out of resonance with the probe beam, and do not effect the measurement. We transfer the atoms between the ground electronic states using a microwave pulse to create Rabi flopping between the two ground states. By adjusting the microwave frequency and pulse duration, we can accurately determine the fraction of atoms that

we transfer. This gives us the flexibility to transfer a different fraction of atoms into the probing state, which lets us keep the observed optical density relatively constant for whichever reservoir we are imaging in our experiment. We are thus able to keep our measurements in an area of maximal signal to noise, and avoid non-linear effects in the imaging.

## Bibliography

- [1] H. K. Onnes. On the sudden rate at which the resistance of mercury disappears. *Akad. van Wetenschappen*, 14:818, 1911.
- [2] D. J. Quinn III and W. B. Ittner III. Resistance in a superconductor. *Journal of Applied Physics*, 33(2):748–749, 1962.
- [3] C. Zhuang, C. Gu, D. X. Chen, and Z. Han. Persistent current of bi2223/ag closed coil in 77 k. *Applied Superconductivity, IEEE Transactions on*, 17:3125–3128, 2007.
- [4] P. Kapitza. Viscosity of liquid helium below the  $\lambda$ -point. *Nature*, 141:74, 1938.
- [5] J. F. Allen and A. D. Misener. Flow of liquid helium ii. *Nature*, 141:75, 1938.
- [6] B.V. Rollin and F. Simon. On the “film” phenomenon of liquid helium II. *Physica*, 6(2):219–230, feb 1939.
- [7] Henry A. Fairbank and C. T. Lane. Rollin film rates in liquid helium. *Physical Review*, 76(8):1209–1211, oct 1949.
- [8] M. R. Matthews, B. P. Anderson, P. C. Haljan, D. S. Hall, C. E. Wieman, and E. A. Cornell. Vortices in a bose-einstein condensate. *Physical Review Letters*, 83(13):2498–2501, sep 1999.
- [9] K. W. Madison, F. Chevy, W. Wohlleben, and J. Dalibard. Vortex formation in a stirred bose-einstein condensate. *Physical Review Letters*, 84(5):806–809, jan 2000.
- [10] K. W. Madison, F. Chevy, W. Wohlleben, and J. Dalibard. Vortices in a stirred bose-einstein condensate. *Journal of Modern Optics*, 47(14-15):2715–2723, nov 2000.
- [11] J. R. Abo-Shaeer, C. Raman, J. M. Vogels, and W. Ketterle. Observation of vortex lattices in bose-einstein condensates. *Science*, 292(5516):476–479, apr 2001.

- [12] C. Raman, M. Köhl, R. Onofrio, D. S. Durfee, C. E. Kuklewicz, Z. Hadzibabic, and W. Ketterle. Evidence for a critical velocity in a bose-einstein condensed gas. *Physical Review Letters*, 83(13):2502–2505, sep 1999.
- [13] R. Onofrio, C. Raman, J. M. Vogels, J. R. Abo-Shaeer, A. P. Chikkatur, and W. Ketterle. Observation of superfluid flow in a bose-einstein condensed gas. *Physical Review Letters*, 85(11):2228–2231, sep 2000.
- [14] P. Engels and C. Atherton. Stationary and nonstationary fluid flow of a bose-einstein condensate through a penetrable barrier. *Physical Review Letters*, 99(16), oct 2007.
- [15] C. Ryu, M. Andersen, P. Cladé, Vasant Natarajan, K. Helmerson, and W. Phillips. Observation of persistent flow of a bose-einstein condensate in a toroidal trap. *Physical Review Letters*, 99(26), dec 2007.
- [16] A. Ramanathan, K. C. Wright, S. R. Muniz, M. Zelan, W. T. Hill, C. J. Lobb, K. Helmerson, W. D. Phillips, and G. K. Campbell. Superflow in a toroidal bose-einstein condensate: An atom circuit with a tunable weak link. *Physical Review Letters*, 106(13), mar 2011.
- [17] F. London. The  $\lambda$ -phenomenon of liquid helium and the bose-einstein degeneracy. *Nature*, 141:643–644, 1938.
- [18] L. Tisza. Transport phenomena in helium ii. *Nature*, 441:913, 1938.
- [19] L. Landau. Theory of the superfluidity of helium ii. *Physical Review*, 60:356–358, 1941.
- [20] V. Peshkov. Second sound in helium ii. *J. Physics USSR*, 8:381, 1944.
- [21] N. N. Bogoliubov. On the theory of superfluidity. *J. Physics(USSR)*, 11(1):23–32.
- [22] L. Onsager. Statistical hydrodynamics. *Il Nuovo Cimento (1943-1954)*, 6(2):279–287, Mar 1949.
- [23] R.P. Feynman. Chapter II application of quantum mechanics to liquid helium. In *Progress in Low Temperature Physics*, pages 17–53. Elsevier, 1955.
- [24] J. Clarke and A. I. Braginski. *The SQUID Handbook: Fundamentals and Technology of SQUIDs and SQUID Systems*. Wiley-VCH, 2004.
- [25] YU. V. Sharvin. On the possible method for studying fermi surfaces. *Zh. Eksp. Teor. Fiz.*, 48:984, 1965. [*Sov. Phys. JETP* **21**, 655 (1965)].
- [26] J. D. Jackson and Ronald F. Fox. Classical electrodynamics, 3rd ed. *American Journal of Physics*, 67(9):841–842, sep 1999.
- [27] C. Kittel and H. Kroemer. *Thermal Physics*. W. H. Freeman, New York, 1980.

- [28] P. Horowitz. *The Art of Electronics*. HARVARD UNIVERSITY PRESS, 2015.
- [29] C. J. Pethick and H. Smith. *BoseEinstein Condensation in Dilute Gases*. Cambridge University Press, 2008.
- [30] A. M. Kadin. *Introduction to Superconducting Circuits*. John Wiley and Sons, New York, 1999.
- [31] M. Tinkham. *Introduction to Superconductivity*. Dover Pubs, 2004.
- [32] B. J. van Wees, H. van Houten, C. W. J. Beenakker, J. G. Williamson, L. P. Kouwenhoven, D. van der Marel, and C. T. Foxon. Quantized conductance of point contacts in a two-dimensional electron gas. *Phys. Rev. Lett.*, 60:848–850, 1988.
- [33] A. Ramanathan. *A Ring with a Spin : Superfluidity in a toroidal Bose-Einstein condensate*. PhD thesis, University of Maryland, 2011.
- [34] C. J. Foot. *Atomic Physics (Oxford Master Series in Physics)*. Oxford University Press, 2005.
- [35] Anand Ramanathan, Sérgio R. Muniz, Kevin C. Wright, Russell P. Anderson, William D. Phillips, Kristian Helmerson, and Gretchen K. Campbell. Partial-transfer absorption imaging: A versatile technique for optimal imaging of ultracold gases. *Review of Scientific Instruments*, 83(8):083119, aug 2012.
- [36] Jesper Glckstad. Phase contrast image synthesis. *Optics Communications*, 130(4):225 – 230, 1996.
- [37] Darwin Palima, Carlo Amadeo Alonzo, Peter John Rodrigo, and Jesper Glückstad. Generalized phase contrast matched to gaussian illumination. *Opt. Express*, 15(19):11971–11977, Sep 2007.
- [38] Carlo Amadeo Alonzo, Peter John Rodrigo, and Jesper Glckstad. Photon-efficient grey-level image projection by the generalized phase contrast method. *New Journal of Physics*, 9(5):132, 2007.
- [39] F. Zernike. How i discovered phase contrast. *Science*, 121(3141):345–349, 1955.
- [40] M. R. Andrews, D. M. Kurn, H.-J. Miesner, D. S. Durfee, C. G. Townsend, S. Inouye, and W. Ketterle. Propagation of sound in a bose-einstein condensate. *Phys. Rev. Lett.*, 79:553–556, Jul 1997.
- [41] D. A. Steck. Rubidium 87 d line data. *available online at <http://steck.us/alkalidata>*.
- [42] D. A. Steck. Sodium d line data. *available online at <http://steck.us/alkalidata>*.